

# Magnetic Interfaces at the Nanoscale: From Fundamentals to Technological Applications

Guest Editors: M. Angelakeris, O. Crisan, and C. Martinez-Boubeta





---

# **Magnetic Interfaces at the Nanoscale: From Fundamentals to Technological Applications**

Journal of Nanomaterials

---

# **Magnetic Interfaces at the Nanoscale: From Fundamentals to Technological Applications**

Guest Editors: M. Angelakeris, O. Crisan,  
and C. Martinez-Boubeta



---

Copyright © 2012 Hindawi Publishing Corporation. All rights reserved.

This is a special issue published in “Journal of Nanomaterials.” All articles are open access articles distributed under the Creative Commons Attribution License, which permits unrestricted use, distribution, and reproduction in any medium, provided the original work is properly cited.

## Editorial Board

- Katerina Aifantis, Greece  
Nageh K. Allam, USA  
Margarida Amaral, Portugal  
Xuedong Bai, China  
L. Balan, France  
Enrico Bergamaschi, Italy  
Theodorian Borca-Tasciuc, USA  
C. Jeffrey Brinker, USA  
Christian Brosseau, France  
Xuebo Cao, China  
Shafiul Chowdhury, USA  
Kwang-Leong Choy, UK  
Cui ChunXiang, China  
Miguel A. Correa-Duarte, Spain  
Shadi A. Dayeh, USA  
Claude Estournes, France  
Alan Fuchs, USA  
Lian Gao, China  
Russell E. Gorga, USA  
Hongchen Chen Gu, China  
Mustafa O. Guler, Turkey  
John Zhanhu Guo, USA  
Smrati Gupta, Germany  
Michael Harris, USA  
Zhongkui Hong, USA  
Michael Z. Hu, USA  
David Hui, USA  
Y.-K. Jeong, Republic of Korea  
Sheng-Rui Jian, Taiwan  
Wanqin Jin, China  
Rakesh K. Joshi, India  
Zhenhui Kang, China  
Fathallah Karimzadeh, Iran  
Alireza Khataee, Iran
- Do Kyung Kim, Korea  
Kin Tak Lau, Australia  
Burtrand Lee, USA  
Benxia Li, China  
Jun Li, Singapore  
Shijun Liao, China  
Gong Ru Lin, Taiwan  
J.-Y. Liu, USA  
Jun Liu, USA  
Tianxi Liu, China  
Songwei Lu, USA  
Daniel Lu, China  
Jue Lu, USA  
Ed Ma, USA  
Gaurav Mago, USA  
Santanu K. Maiti, Israel  
Sanjay R. Mathur, Germany  
A. McCormick, USA  
Vikas Mittal, UAE  
Weihai Ni, Germany  
Sherine Obare, USA  
Abdelwahab Omri, Canada  
Edward Andrew Payzant, USA  
Kui-Qing Peng, China  
Anukorn Phuruangrat, Thailand  
Ugur Serincan, Turkey  
Huaiyu Shao, Japan  
Donglu Shi, USA  
Suprakas Sinha Ray, South Africa  
Vladimir Sivakov, Germany  
Marinella Striccoli, Italy  
Bohua Sun, South Africa  
Saikat Talapatra, USA  
Nairong Tao, China
- Titipun Thongtem, Thailand  
Somchai Thongtem, Thailand  
Alexander Tolmachev, Ukraine  
Valeri P. Tolstoy, Russia  
Tsung-Yen Tsai, Taiwan  
Takuya Tsuzuki, Australia  
Raquel Verdejo, Spain  
Mat U. Wahit, Malaysia  
Shiren Wang, USA  
Yong Wang, USA  
Ruibing Wang, Canada  
Cheng Wang, China  
Zhenbo Wang, China  
Jinquan Wei, China  
Ching Ping Wong, USA  
Xingcai Wu, China  
Guodong Xia, Hong Kong  
Zhi Li Xiao, USA  
Ping Xiao, UK  
Shuangxi Xing, China  
Yangchuan Xing, USA  
N. Xu, China  
Doron Yadlovker, Israel  
Ying-Kui Yang, China  
Khaled Youssef, USA  
William W. Yu, USA  
Kui Yu, Canada  
Haibo Zeng, China  
Tianyou Zhai, Japan  
Renyun Zhang, Sweden  
Yanbao Zhao, China  
Lianxi Zheng, Singapore  
Chunyi Zhi, Japan

## Contents

**Magnetic Interfaces at the Nanoscale: From Fundamentals to Technological Applications**, M. Angelakeris, O. Crisan, and C. Martinez-Boubeta  
Volume 2012, Article ID 619485, 1 page

**FMR Study of the Porous Silicate Glasses with Fe<sub>3</sub>O<sub>4</sub> Magnetic Nanoparticles Fillers**, B. Zapotoczny, M. R. Dudek, N. Guskos, J. J. Koziół, B. V. Padlyak, M. Kośmider, and E. Rysiakiewicz-Pasek  
Volume 2012, Article ID 341073, 7 pages

**Electronic and Magnetic Properties of the Interface LaAlO<sub>3</sub>/TiO<sub>2</sub> Anatase from Density Functional Theory**, Mariana Weissmann and V. Ferrari  
Volume 2012, Article ID 757493, 5 pages

**Effect of Titanium Substitution on Magnetic Properties and Microstructure of Nanocrystalline Monophase Nd-Fe-B Magnets**, Wang Cong, Guo ZhiMeng, Sui YanLi, Bao XiaoQian, and Chen ZhiAn  
Volume 2012, Article ID 425028, 5 pages

**Interlayer Thickness Effects on Magnetic Properties of X/FePtAg (X = FePt/Fe and Fe/FePt) Trilayers**, Jai-Lin Tsai, Jian-Chiang Huang, and Hsueh-Wei Tai  
Volume 2012, Article ID 129097, 7 pages

**Positive Contrast Imaging of SPIO Nanoparticles**, Chenghong Lin, Shuhui Cai, and Jianghua Feng  
Volume 2012, Article ID 734842, 9 pages

**Simulation of Magnetophoretic Separation Processes in Dispersions of Superparamagnetic Nanoparticles in the Noncooperative Regime**, Jordi S. Andreu, Pablo Barbero, Juan Camacho, and Jordi Farauo  
Volume 2012, Article ID 678581, 10 pages

**Angular Response of Magnetostrictive Thin Films**, Jianjun Li  
Volume 2012, Article ID 940272, 7 pages

**Fabrication and Characterization of Composite Containing HCl-Doped Polyaniline and Fe Nanoparticles**, Rongcheng Liu, Hong Qiu, Hua Zong, and Chunying Fang  
Volume 2012, Article ID 674104, 7 pages

## Editorial

# Magnetic Interfaces at the Nanoscale: From Fundamentals to Technological Applications

**M. Angelakeris,<sup>1</sup> O. Crisan,<sup>2</sup> and C. Martinez-Boubeta<sup>3</sup>**

<sup>1</sup>Department of Physics, Aristotle University of Thessaloniki, Thessaloniki, Greece

<sup>2</sup>National Institute for Materials Physics, Bucharest, Romania

<sup>3</sup>Department of Electronics, University of Barcelona, Barcelona, Spain

Correspondence should be addressed to M. Angelakeris, [angelaker@auth.gr](mailto:angelaker@auth.gr)

Received 12 July 2012; Accepted 12 July 2012

Copyright © 2012 M. Angelakeris et al. This is an open access article distributed under the Creative Commons Attribution License, which permits unrestricted use, distribution, and reproduction in any medium, provided the original work is properly cited.

One of the most widely researched topics over the last decades has been magnetic nanoscale systems, but recent breakthroughs in high-resolution imaging techniques in modern computing and electronics towards continuously smaller devices have nourished a booming in the quest for new materials and their novel applications. It is unambiguous that the interest for tailor-made and properly functionalized particles is very wide and expected results will be of enormous benefit for the global economy. Still, researchers should improve the manufacture of nanomaterials on a larger scale at a lower cost. In nanotechnology, methods to produce some desired structure must satisfy certain conditions, such as *speed*, *performance*, and *precision*. Although computer modelling may provide a hint in finding a structure that minimizes the internal energy, control of nanoscale phenomena in real time remains a puzzle in most cases. In this regard, even if certain prerequisites should be fulfilled for specific applications, magnetic nanoscale systems exploitation lays in the control of their interface properties.

Nanomagnets may enter in the production of almost every product we use, as standard magnets do. Among them, magnetic nanoparticles deserve special attention because of their extended applicability not only for data storage and nanoscale spintronics applications but also for healthcare. Medical researchers are actively seeking to develop improved tools for diagnosis (gene sequencing, high contrast agents for imaging) and new therapies such as hyperthermia where functionalized magnetic nanoparticles may target only the tumors without harming the healthy tissues or could be used in synergy with chemotherapeutic drug delivery.

This special issue provides a carefully selected compilation of original research papers as well as review articles

in understanding and insight of magnetic properties at nanoscale interfaces. Our scientific goal was to collect articles focusing on chemical and magnetic interfaces of nanostructured materials, in determining their influences on intrinsic magnetic properties, and to trace the role of these issues in the macroscopic behavior of nanostructures.

We did our best to conduct review and editing processes according to international standards, and we believe this special issue addresses a novel emerging technology, namely the control, functionalization, and analysis of nanometer-sized magnetic materials. Eventually, it turned out that about 50% of submitted papers have been finally accepted for publication. Finally, we would like to thank all the reviewers for their prompt and substantial involvement and all the authors for the interesting and fruitful results presented in this issue and we hope that especially young scientists will benefit from this multidisciplinary special issue, which is relevant to various up-to-date and future nanotechnologies.

M. Angelakeris  
O. Crisan  
C. Martinez-Boubeta

## Research Article

# FMR Study of the Porous Silicate Glasses with $\text{Fe}_3\text{O}_4$ Magnetic Nanoparticles Fillers

**B. Zapotoczny,<sup>1</sup> M. R. Dudek,<sup>1</sup> N. Guskos,<sup>2,3</sup> J. J. Koziół,<sup>4</sup>  
B. V. Padlyak,<sup>1,5</sup> M. Kośmider,<sup>1</sup> and E. Rysiakiewicz-Pasek<sup>6</sup>**

<sup>1</sup>*Institute of Physics, University of Zielona Góra, ul. Szafrana 4a, 65-069 Zielona Góra, Poland*

<sup>2</sup>*Department of Solid State Physics, University of Athens, Panepistimiopolis, 15 784 Athens, Greece*

<sup>3</sup>*Institute of Physics, West Pomeranian University of Technology, Al. Piastow 17, 70-310 Szczecin, Poland*

<sup>4</sup>*Faculty of Biological Sciences, University of Zielona Góra, ul. Szafrana 1, 65-516 Zielona Góra, Poland*

<sup>5</sup>*Sector of Spectroscopy, Institute of Physical Optics, Dragomanov Street 23, 79-005 Lviv, Ukraine*

<sup>6</sup>*Institute of Physics, Wrocław University of Technology, Wyb. Wyspiańskiego 27, 50-370 Wrocław, Poland*

Correspondence should be addressed to M. R. Dudek, m.dudek@if.uz.zgora.pl

Received 16 March 2012; Revised 7 June 2012; Accepted 26 June 2012

Academic Editor: Makis Angelakeris

Copyright © 2012 B. Zapotoczny et al. This is an open access article distributed under the Creative Commons Attribution License, which permits unrestricted use, distribution, and reproduction in any medium, provided the original work is properly cited.

The results of research on new magnetic materials for biomedical applications are discussed. These materials are porous silicate glasses with magnetic fillers. To ensure the smallest number of components for subsequent removal from the body, the magnetic fillers are bare magnetite nanoparticles ( $\text{Fe}_3\text{O}_4$ ). The magnetic properties of these materials have been investigated using the ferromagnetic resonance method (FMR). The FMR analysis has been complemented by scanning electron microscope (SEM) measurements. In order to examine the effect of time degradation on filling the porous glass with bare magnetite nanoparticles the FMR measurement was repeated five months later. For the samples with high degree of pore filling, in contrast to the samples with low degree of pore filling, the FMR signal was still strong. The influence of different pH values of magnetite nanoparticles aqueous suspension on the degree of filling the pores of glasses is also discussed. The experimental results are supported by computer simulations of FMR experiment for a cluster of  $N$  magnetic nanoparticles locked in a porous medium based on a stochastic version of the Landau-Lifshitz equation for nanoparticle magnetization.

## 1. Introduction

The ferrimagnetic magnetite ( $\text{Fe}_3\text{O}_4$ ) nanoparticles are considered among the promising materials for biotechnological and medical applications because of their biocompatibility and low toxicity [1, 2]. An obstacle in the direct use of bare magnetite nanoparticles is their tendency to degrade their magnetic properties with time when exposed to atmospheric air. Therefore, it is necessary to cover the magnetic nanoparticle's surface with a nonmagnetic protective layer. On the other hand, in some medical applications such as magnetic nanocapsules for drug delivery, it is more desirable to use materials with the smallest number of components for subsequent removal from the body. Taking this into account, the study of magnetic properties of bare magnetic nanoparticles for different nonmagnetic matrices is an important goal of research.

In the following, we show that bare magnetite nanoparticles can be fillers of a porous silicate glass without the need for additional protective layer of nanoparticles. In this case, the nonmagnetic porous surrounding of the magnetic nanoparticles acts as a protective layer and magnetic properties of such materials may remain unchanged for a long time. In order to determine the magnetic properties of the samples under consideration we use the method of ferromagnetic resonance (FMR) [3]. It is known that FMR spectroscopy is a very efficient tool to study the magnetic properties of magnetic agglomerates in nonmagnetic matrices [4, 5]. Recently, magnetic nanopowders placed in various nonmagnetic polymer matrices have been proposed as the new types of smart materials which combine mechanical properties of polymer matrix and magnetic response of nanoparticles, for example, in hyperthermia treatment, in magnetic nanocapsules for drug targeting or intracellular manipulation, and so

TABLE 1: Parameters of the porous glass texture.

Parameter	Glass B	Glass D
Specific area, m <sup>2</sup> /g	28.9	5.9
Pore volume, cm <sup>3</sup> /g	0.44	0.47
Average diameter, nm	45	320
Porosity, %	50	48

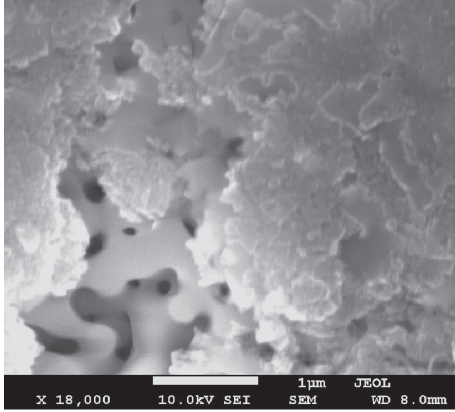


FIGURE 1: SEM visualisation of the porous silicate glass surface area (sample D).

forth (e.g., [6, 7]). The silica-based materials are currently implemented in medical and biotechnological applications such as bone-repairing devices and drug delivery systems [8, 9].

## 2. Experimental

Two types of porous silica glass samples (B and D) were studied and they were obtained as a leaching product from one sodium-borosilicate glass with a chemical composition as follows: 90–91% SiO<sub>2</sub>, 8.3–8.7% B<sub>2</sub>O<sub>3</sub>, 0.3–0.6% Na<sub>2</sub>O (%mol). For phase separation glass B was heated at 490°C for 165 hours and glass D was heated at 650°C for 100 hours. All the samples were etched in hydrochloric acid and rinsed in deionized water. Then both types of glasses were immersed in KOH [10]. The texture of obtained porous glasses was essentially different (Table 1). In Figure 1 the example of a pore structure in the case of sample D is shown.

In the experimental stage, which refers to filling the pores of porous glass by magnetic nanoparticles, glass samples (with dimensions 10 × 10 × 0.5 mm<sup>3</sup>) were immersed in an aqueous suspension of magnetite nanoparticles (Fe<sub>3</sub>O<sub>4</sub>) for about 48 hours. The experiment was repeated for different values of pH of the aqueous solution. The glass samples were filled with magnetite nanoparticles as a result of a diffusion process from the magnetic suspension. The initial pH value of the water solution with the nanoparticles was adjusted by adding an appropriate amount of the hydrochloric acid or sodium hydroxide. In this work, five samples of porous glass filled with magnetic nanoparticles at different pH values were selected for investigation. They were denoted as sample 1, sample 2, sample 3 (glass type B, pH values 7.92, 8.78, 9.04,

resp.), and samples 4 and 5 (glass type D, pH values 7.90 and 7.94, resp.). Samples 4 and 5 were filled with magnetic nanoparticles at approximately the same pH value but sample 5 was subjected to an external constant magnetic field from a permanent magnet ( $B_{\text{sat}} \sim 0.5$  T) during the filling process.

The nanoparticles were synthesized according to the Massart's method [11]. Their diameter was smaller than 20 nm. The size of the magnetic nanoparticles has been measured by using semicontact Ntegra Aura system (Scanning Probe Microscope) with a 100 × 100 × 10 μm closed-loop sample scanner. In Figure 2, two images on the sample of Fe<sub>3</sub>O<sub>4</sub> nanoparticles, which has been presented on the fresh mica surface by using drop-coating method after being dispersed into ethanol solvent, are shown. In (a), a small 2.0 × 2.0 μm area has been shown with many tiny magnetic nanoparticles and two of them have been chosen for a detailed investigation in (b). A Si cantilever was used in these measurements with a force constant of  $\sim 2.0$  N/m and a resonance of  $\sim 120$  kHz. The curvature of the Si tip is 10 nm. Two representative magnetic nanoparticles have dimensions of 14.94 nm and 12.82 nm.

For measurements of FMR spectra of the samples of porous glass filled with magnetic nanoparticles the glass plates were broken into pieces with average dimensions 2 × 2 × 0.5 mm<sup>3</sup>. Next, these pieces were subjected to FMR measurements. The FMR spectra were recorded using X-band ( $f \sim 9.4$  GHz) EPR spectrometer of the SE/X-2013 type (RADIOPAN, Poznań, Poland), operating in high-frequency (100 kHz) modulation mode of magnetic field at room temperature. In addition to FMR measurements the morphology of the porous glass samples has been investigated using the scanning electron microscope (SEM) JEOL 7600F with the energy-dispersive X-ray spectroscopy (EDS) system integrated into it to examine both sample's surface and interior. The latter was the cross-section of the samples after they have been broken in smaller pieces.

## 3. Discussion of Results

Our method of filling the porous glass is a direct immersion of the samples of porous glasses in an aqueous suspension of magnetic nanoparticles. The filling takes place at a given pH value of the water solution and pH value is one of the most important parameters for controlling the process of diffusion of magnetic nanoparticles from the solution to the pores of glasses and their adsorption into them. It is known that both magnetite nanoparticles and porous glass samples possess a pH-dependent surface charge after contacting aqueous solution. The charge is positive for pH < PZC, where PZC represents the point of zero charge and the charge is negative otherwise. The values of PZC for the silicate glass samples (PZC<sub>g</sub>) and magnetite nanoparticles (PZC<sub>m</sub>) are substantially different, PZC<sub>m</sub>  $\sim 7.9$  (in the literature PZC<sub>m</sub> ranges from 6.3 to 7.9 [12–15]) whereas PZC<sub>g</sub>  $\sim 1.8$  for the silicate glasses [16, 17]. In our case, the process of filling the pores by magnetic nanoparticles was carried out for pH > PZC<sub>g</sub> for both pH < PZC<sub>m</sub> and pH > PZC<sub>m</sub>. This means that

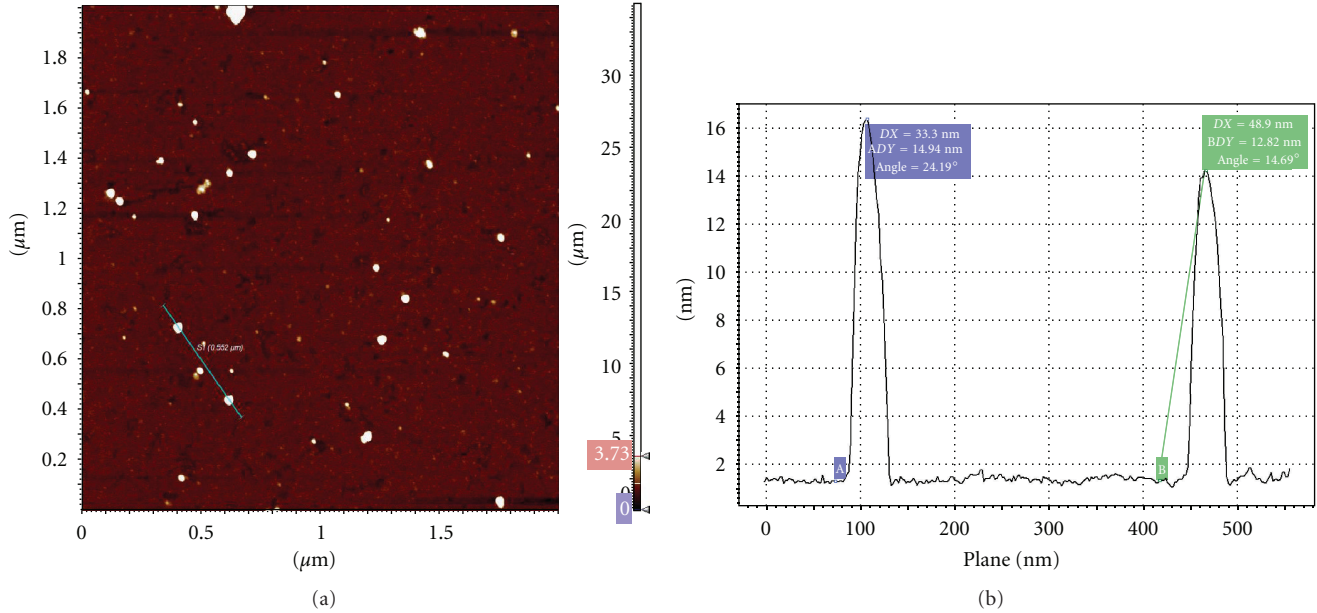


FIGURE 2: Investigation of  $\text{Fe}_3\text{O}_4$  nanoparticle by Ntegra Aura system (Scanning Probe Microscope): (a) sample of  $\text{Fe}_3\text{O}_4$  nanoparticles in  $2.0 \times 2.0 \mu\text{m}$  scanning area, (b) two nanoparticles have been measured and the dimensions are 14.94 nm and 12.82 nm.

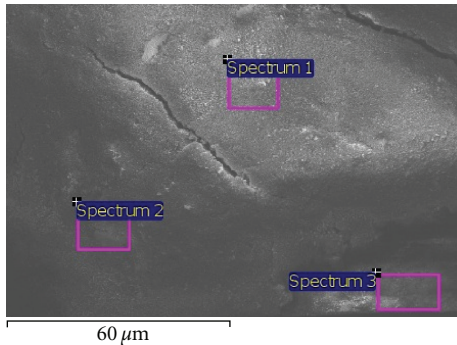


FIGURE 3: SEM visualisation of a large surface fragment of the sample 2 (glass of type B), where three rectangular areas were selected for whom EDS analysis was carried out (Table 2).

porous glass surface was always negatively charged whereas the surface charges of magnetic nanoparticles were positive or negative unless  $\text{pH} = \text{PZC}_m$ . We have observed that the best filling of glasses of type B takes place when  $\text{pH} \gtrsim \text{PZC}_m$ , that is, when the surface charge of magnetic nanoparticle is positive. Close to  $\text{pH} \sim \text{PZC}_m$  the electrostatic repulsion between the magnetic nanoparticles weakens and magnetic dipolar forces causes them to aggregate. The filling process appeared to be inefficient for glasses of type D at  $\text{pH} \sim \text{PZC}_m$ . It is interesting that in the latter case we have observed the improving of the degree of pore filling after the magnetic nanoparticles were exposed to a weak external magnetic field, which introduces an additional aggregation of magnetic nanoparticles. Note that the average pore diameter for samples D is several times larger than the average diameter of the synthesized magnetite nanoparticles opposed to type B

TABLE 2: Elements identified by SEM on the surface of sample 1 in three regions denoted as Spectrum 1, Spectrum 2, Spectrum 3 in Figure 3.

	Element	Weight%	Atomic%
Spectrum 1	O K	25.48	54.41
	Fe K	74.52	45.59
Spectrum 2	O K	28.20	56.27
	Si K	4.73	5.38
Spectrum 3	Fe K	67.07	38.35
	O K	55.08	68.28
	Si K	44.92	31.72

samples. In the case of type B samples the external magnetic field prevented insertion of nanoparticles inside the pores of the glass because the size of the magnetic aggregations that have been created exceeded the pore diameter.

We examined the surface of five samples of silica glass with magnetic fillers, samples 1–5 which have been defined in Section 2, using SEM (scanning electron microscope). We have observed that large areas of the surface of the porous glass samples with linear dimensions of micrometers have been coated with a homogeneous layer of magnetic nanoparticles. In Figure 3, it has been shown the surface of sample 2, where three rectangular areas were selected for whom EDS analysis was carried out (Table 2). It is evident from the SEM data in Table 2 that there are large surface areas occupied by magnetic nanoparticles, like the one in a window called Spectrum 1.

Using the SEM/EDS visualisation we obtained also information concerning the filling of pores of porous glass in the range of a few micrometers below the surface layer of glass.

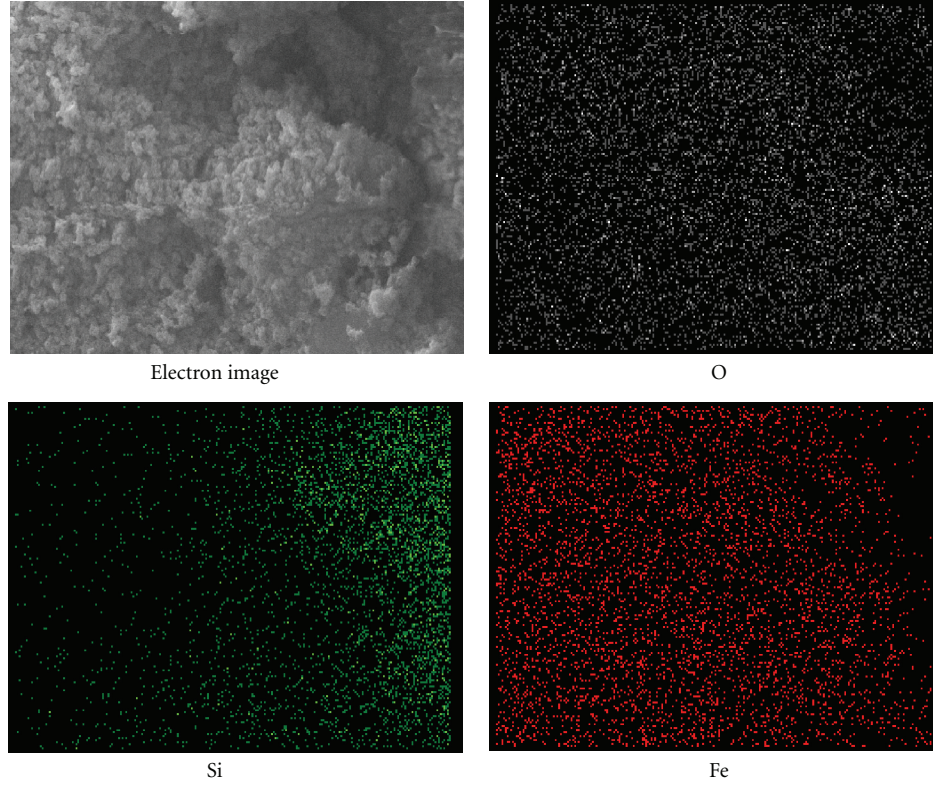


FIGURE 4: SEM/EDS images of the surface of the cross-section ( $4.5 \times 6.0 \mu\text{m}$ ) of porous silicate glass sample which was obtained after breaking the sample. The first photo shows an SEM visualization of the cross-section surface. The remaining three photos represent space distribution of different elements, Si, O, Fe, identified in this cross-section with the respective color saturation corresponding to the actual density of the identified elements.

This has been done by breaking the glass sample and observing the distribution of elements in the resulting cross-sections. The results of this analysis have been shown in Figure 4 and it is evident that the inner layers of the porous glass are very homogeneously filled with the magnetite nanoparticles.

Some information on the magnetic properties of the silica glass filled with nanoparticles can be obtained from the analysis of the absorption lines in FMR experiment. They represent the imaginary part  $\chi''$  of the complex ac magnetic susceptibility

$$\chi = \chi' - i\chi'' \quad (1)$$

In the FMR experiments, the absorption lines derivatives,  $d\chi''/dH_{\text{dc}}$ , with respect to the external dc magnetic field are measured instead of direct measuring of  $\chi''$ . It is always the case that  $H_{\text{dc}}$  is transverse to an external ac magnetic field  $H_{\text{ac}}$  which is rotating with a frequency  $f$ . The ferromagnetic resonance condition takes place when

$$f = \frac{\gamma}{2\pi} H_{\text{eff}}, \quad (2)$$

where  $\gamma = 2.21 \times 10^5 \text{ s}^{-1} (\text{A/m})^{-1}$  denotes the gyromagnetic ratio and  $H_{\text{eff}}$  represents the net magnetic field experienced by a magnetic moment of magnetic nanoparticle.

The FMR experiment technique [3] is one of the basic methods for determining the magnetic properties of magnetic agglomerates dispersed in nonmagnetic matrices. Usually, the main peak corresponding to the uniform resonance mode in the FMR spectra is accompanied by a series of other peaks which originate both from a spin-wave exchange model [18, 19] and dipolar interparticle interactions and they can as well be coupled with the magnetoelastic phenomena. The latter case has been discussed in [20] in the case of the  $\gamma\text{-Fe}_2\text{O}_3$  ferrimagnetic nanoparticles embedded in a multiblock poly(ether-ester) copolymer nonmagnetic matrix. The results suggested that some additional peaks in low temperatures originate from the orientational anisotropy of frozen polymer blocks. The same interpretation of the presence of additional peaks in the case of materials with random agglomerates of magnetic nanoparticles can be found in theoretical papers, for example, [5, 21], where the stochastic version of the Landau-Lifshitz equation [22, 23] has been used to model the ferromagnetic resonance. In the papers, there is a discussion on the shape of the ferromagnetic resonance spectra for the ensemble of the randomly distributed magnetic anisotropy axes and their dependence on temperature. In particular, it is observed the multimodal FMR signal and its broadening for the randomly distributed magnetic anisotropy axes as compared to the magnetic nanoparticles which all have the same orientation of the

magnetic anisotropy. These theoretical models adequately can explain the asymmetric and multimodal FMR spectral line shape which we have received for the agglomerates of magnetite nanoparticles in porous glasses in the case of Figures 5 and 6. Note that qualitatively the same topology of the FMR signal, as in Figures 5 and 6, has been shown in Figure 7, which is a result of the computer simulation of the random clusters consisting of  $N = 80$  and  $N = 200$  magnetic nanoparticles, respectively. In the same figure, there have been also plotted the spectral lines of the single chains consisting of  $N = 40$  magnetic nanoparticles. The single chains were oriented in the direction of the field  $H_{dc}$  (dot-dashed line in the figure) and transversely to it (dashed line in the figure), respectively. The simulation results suggest that in the case of the silica glass filled with magnetic nanoparticles (Figures 5 and 6) there are large magnetic agglomerates inside them which have the orientation of anisotropy axis aligned with the direction of the field  $H_{dc}$  and there are also large clusters where the orientation is set transversely to the direction of the  $H_{dc}$ . In the computer simulations, the dc magnetic field has been chosen into  $z$ -direction ( $H_z = H_{dc}$ ) and the ac magnetic field into  $x$ -direction ( $H_x = H_{ac} = H_{ac}^0 \cos(2\pi f t)$ ). In this case, the components of the complex ac susceptibility (1) have been calculated by performing the Fourier transform on the time averaged  $x$ -component of the magnetization, that is,

$$\chi = \frac{1}{\tau H_{ac}^0} \int_0^\tau dt M_x(t) e^{-i2\pi f t}, \quad (3)$$

where  $\tau = 1/f$ . The values  $M_x(t)$  are calculated with the help of the Landau-Lifshitz equation ([5, Equation (12)]) describing the magnetic nanoparticle magnetization dynamics in the case of the frozen orientation of its magnetic anisotropy axis.

The experimental results in Figures 5 and 6 concern the newly synthesized porous glass and magnetic nanoparticles. In view of the potential applications of such material to the magnetic nanocapsules important is the question of the degradation of the magnetic material in these nanocapsules since magnetite nanoparticles degrade with time if they are exposed to atmospheric air. We have measured the FMR signal from the selected samples of porous glass with magnetic fillers after the expiry of five months. In general, we observed that in the cases where the magnetite nanoparticles are mainly deposited on the surface of porous glass (samples of type D) the FMR signal decreased. The signal from the magnetic nanoparticles inside the glass remained just as strong as five months earlier. These trends are evident in Figures 8 and 9 for samples 1 and 5, respectively. The main resonance amplitudes of the ageing samples decrease and they are shifted towards higher values of the magnetic field  $H_{dc}$  as compared with the newly synthesized samples. The ageing of the samples introduces additional averaging of the FMR signal possibly due to the reorientation of magnetic anisotropy axes as it is suggested by computer simulations (Figure 7). This signal averaging effect is greater for sample 5 (Figure 9) with pores of large diameter than for sample 1 (Figure 8)

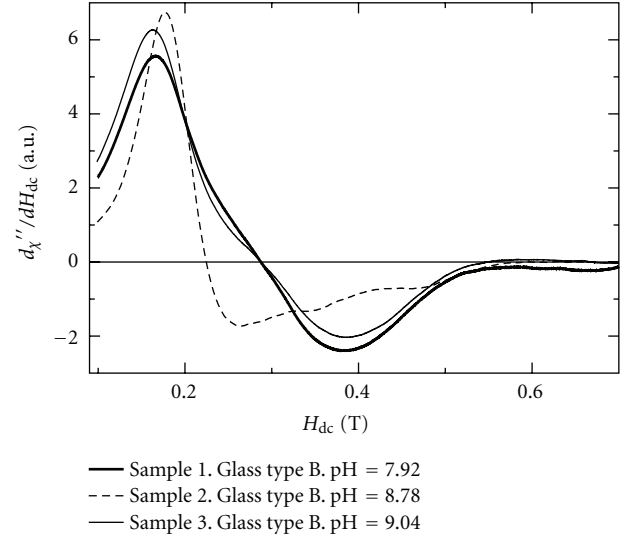


FIGURE 5: The examples of the dependence of the absorption lines derivatives,  $d\chi''/dH_{dc}$ , on dc magnetic field  $H_{dc}$ . The spectral lines were recorded for three different samples of porous glass of type B in the case when magnetic nanoparticles filling the samples come from the magnetic aqueous suspension with pH value 7.92, 8.78, and 9.04, respectively.

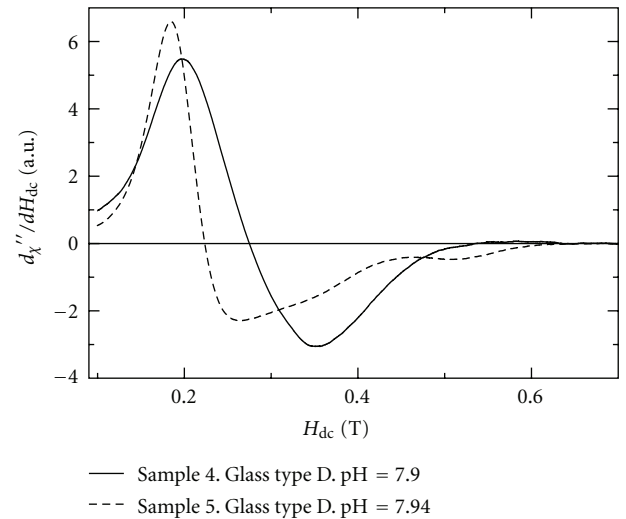


FIGURE 6: The dependence of the absorption lines derivatives,  $d\chi''/dH_{dc}$ , on dc magnetic field  $H_{dc}$  for two samples of type D. The plot made by dashed line relates to magnetic nanoparticles, which in the course of filling the pores of the porous glass were subjected to an external magnetic field of a permanent magnet ( $B_{sat} \sim 0.5$  T). It was not the case for the plot made by continuous line.

with a small pore diameter. The results confirm the importance of porous structure to prevent degradation of the magnetite nanoparticles. This property is promising for using the porous silica glasses filled with magnetite nanoparticles, for example, for the radiofrequency heating applications.

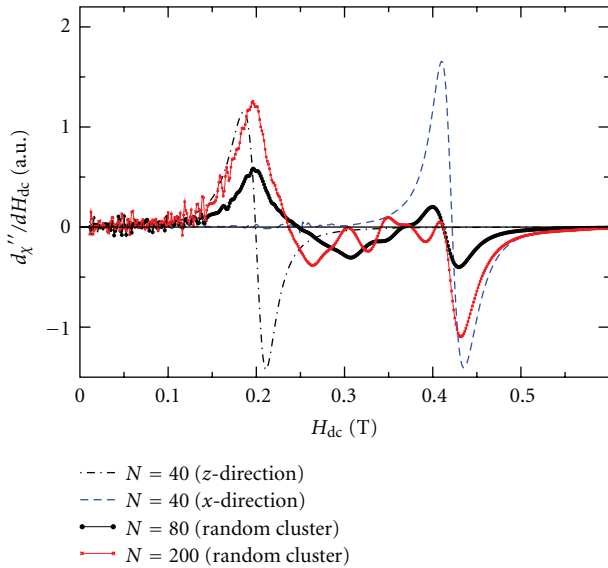


FIGURE 7: Absorption lines derivatives,  $d\chi''/dH_{dc}$ , resulting from the computer simulations in the case when magnetic anisotropy axes orientations represent a chain-like structure of  $N = 40$  magnetic nanoparticles oriented into  $z$ -direction, chain-like structure of  $N = 40$  nanoparticles oriented into  $x$ -direction, or they represent a random cluster consisting of  $N = 80$  and  $N = 200$ , respectively. The parameters of the computer simulation have only a qualitative meaning and they have been taken the same as in [5].

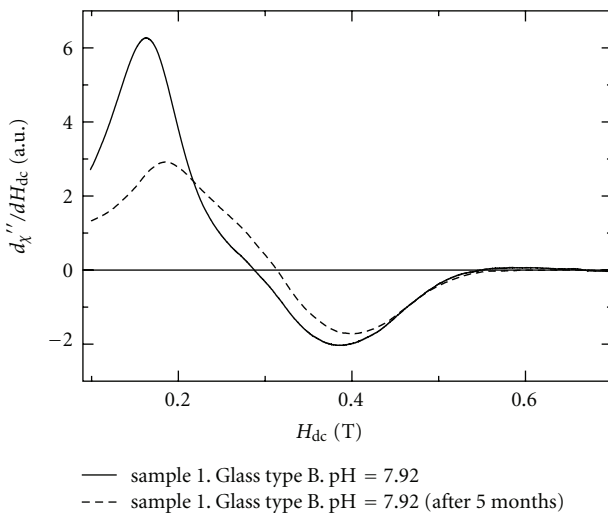


FIGURE 8: Visualization of the effects of ageing of magnetite nanoparticles in porous silicate glass of type B (sample 1) in terms of the FMR signal for the same samples after the expiration of five months.

## 4. Conclusions

We have described the procedure of preparation of silica porous glasses filled with magnetite nanoparticles. We have shown that the magnetic nanoparticles do not degrade for long time, and therefore we suggest the possibility of a simple production of such systems for medical purposes, while

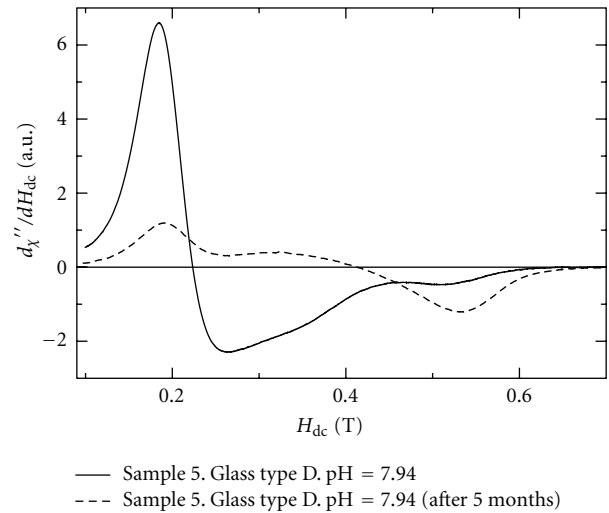


FIGURE 9: The same as in Figure 8 but for sample 5 of the glass of type D.

ensuring no chemical pollutants typical of other methods of coated nanoparticles synthesis. The ability to control the average pore diameter during the synthesis of porous glass provides additional opportunities for specialization of such systems.

## Acknowledgments

The authors thank Adam Drzewiecki, M.S., for the FMR measurements, Professor Krasicka-Cydzik and Agnieszka Kaczmarek, M.S., for the SEM measurements. Some of the computer simulations have been performed in Wrocław Centre for Networking and Supercomputing, Poland.

## References

- [1] P. Tartaj, M. Del Puerto Morales, S. Veintemillas-Verdaguer, T. González-Carreño, and C. J. Serna, "The preparation of magnetic nanoparticles for applications in biomedicine," *Journal of Physics D*, vol. 36, no. 13, pp. R182–R197, 2003.
- [2] Y. Liu, Z. Chen, and J. Wang, "Systematic evaluation of biocompatibility of magnetic  $\text{Fe}_3\text{O}_4$  nanoparticles with six different mammalian cell lines," *Journal of Nanoparticle Research*, vol. 13, p. 199, 2011.
- [3] J. H. Van Vleck, "Concerning the theory of ferromagnetic resonance absorption," *Physical Review*, vol. 78, no. 3, pp. 266–274, 1950.
- [4] N. Guskos, V. Likodimos, S. Glenis et al., "Magnetic properties of  $\gamma\text{-Fe}_2\text{O}_3$ /Poly(Ether-Ester) nanocomposites," *Journal of Nanoscience and Nanotechnology*, vol. 8, no. 4, pp. 2127–2134, 2008.
- [5] M. R. Dudek, N. Guskos, E. Senderek, and Z. Roslaniec, "Temperature dependence of the FMR absorption lines in viscoelastic magnetic materials," *Journal of Alloys and Compounds*, vol. 504, no. 2, pp. 289–295, 2010.
- [6] J. Gao and B. Xu, "Applications of nanomaterials inside cells," *Nano Today*, vol. 4, no. 1, pp. 37–51, 2009.

- [7] T. Y. Liu, S. H. Hu, D. M. Liu, S. Y. Chen, and I. W. Chen, "Biomedical nanoparticle carriers with combined thermal and magnetic responses," *Nano Today*, vol. 4, no. 1, pp. 52–65, 2009.
- [8] M. Vallet-Regí and F. Balas, "Silica materials for medical applications," *Open Biomedical Engineering Journal*, vol. 2, p. 1, 2008.
- [9] S. Li, L. Nguyen, H. Xiong et al., "Nanocarriers for biomedical applications," *Journal of the South Carolina Academy of Science*, vol. 9, no. 1, p. 30, 2011.
- [10] E. Rysiakiewicz-Pasek, P. Łukaszewski, and J. Bogdańska, "Influence of water adsorption on mechanical properties of porous glasses," *Optica Applicata*, vol. 30, no. 1, pp. 173–176, 2000.
- [11] R. Massart, "Preparation of aqueous magnetic liquids in alkaline and acidic media," *IEEE Transactions on Magnetics*, vol. 17, no. 2, pp. 1247–1248, 1981.
- [12] M. Kosmulski, "pH-dependent surface charging and points of zero charge: III. Update," *Journal of Colloid and Interface Science*, vol. 298, no. 2, pp. 730–741, 2006.
- [13] I. Kazeminezhad and S. Mosivand, "Size dependence of electrooxidized  $\text{Fe}_3\text{O}_4$  nanoparticles on surfactant concentration," *Proceedings of World Academy of Science, Engineering and Technology*, vol. 74, pp. 338–341, 2011.
- [14] M. Barale, C. Mansour, F. Carrette et al., "Characterization of the surface charge of oxide particles of PWR primary water circuits from 5 to 320 °C," *Journal of Nuclear Materials*, vol. 381, no. 3, pp. 302–308, 2008.
- [15] E. Tombacz, A. Majzik, Z. S. Horvat, and E. Illes, "Magnetite in aqueous medium: coating its surface and surface coated with it," *Romanian Reports in Physics*, vol. 58, no. 3, pp. 281–286, 2006.
- [16] D. P. J. Barz, M. J. Vogel, and P. H. Steen, "Determination of the zeta potential of porous substrates by droplet deflection. I. The influence of ionic strength and pH value of an aqueous electrolyte in contact with a borosilicate surface," *Langmuir*, vol. 25, no. 3, pp. 1842–1850, 2009.
- [17] E. J. Mathes and W. Friess, "Influence of pH and ionic strength on IgG adsorption to vials," *European Journal of Pharmaceutics and Biopharmaceutics*, vol. 78, no. 2, pp. 239–247, 2011.
- [18] S. Jung, B. Watkins, L. De Long, J. B. Ketterson, and V. Chandrasekhar, "Ferromagnetic resonance in periodic particle arrays," *Physical Review B*, vol. 66, no. 13, Article ID 132401, 2002.
- [19] S. Jung, J. B. Ketterson, and V. Chandrasekhar, "Micromagnetic calculations of ferromagnetic resonance in submicron ferromagnetic particles," *Physical Review B*, vol. 66, no. 13, Article ID 132405, 2002.
- [20] N. Guskos, S. Glenis, V. Likodimos et al., "Matrix effects on the magnetic properties of  $\gamma\text{-Fe}_2\text{O}_3$  nanoparticles dispersed in a multiblock copolymer," *Journal of Applied Physics*, vol. 99, no. 8, Article ID 084307, 2006.
- [21] A. Sukhov, K. D. Usadel, and U. Nowak, "Ferromagnetic resonance in an ensemble of nanoparticles with randomly distributed anisotropy axes," *Journal of Magnetism and Magnetic Materials*, vol. 320, no. 1-2, pp. 31–35, 2008.
- [22] L. Landau and E. Lifshitz, "On the theory of the dispersion of magnetic permeability in ferromagnetic bodies," *Physik Z. Sowjetunion*, vol. 8, p. 153, 1935.
- [23] T. L. Gilbert, "A Lagrangian formulation of the gyromagnetic equation of the magnetic field," *Physical Review*, vol. 100, p. 1243, 1955.

## Research Article

# Electronic and Magnetic Properties of the Interface $\text{LaAlO}_3/\text{TiO}_2$ Anatase from Density Functional Theory

**Mariana Weissmann and V. Ferrari**

*Gerencia de Investigación y Aplicaciones, CNEA, Avenida General Paz 1499, San Martín, 1650 Buenos Aires, Argentina*

Correspondence should be addressed to Mariana Weissmann, weissman@cnea.gov.ar

Received 16 February 2012; Accepted 7 April 2012

Academic Editor: Carlos Martinez-Boubeta

Copyright © 2012 M. Weissmann and V. Ferrari. This is an open access article distributed under the Creative Commons Attribution License, which permits unrestricted use, distribution, and reproduction in any medium, provided the original work is properly cited.

Ab initio calculations using the local spin density approximation and also including the Hubbard  $U$  have been performed for three low-energy configurations of the interface between  $\text{LaAlO}_3$  and  $\text{TiO}_2$  anatase. Two types of interfaces have been considered:  $\text{LaO}/\text{TiO}_2$  and  $\text{AlO}_2/\text{TiO}_2$ , the latter with Ti termination and therefore a missing oxygen. A slab-geometry calculation was carried out, and all the atoms were allowed to relax in the direction normal to the interface. In all the cases considered, the interfacial Ti atom acquires a local magnetic moment, and its formal valence is less than +4. When there are oxygen vacancies, this valence decreases abruptly inside the anatase slab, while in the  $\text{LaO}/\text{TiO}_2$  interface, the changes are more gradual.

## 1. Introduction

Complex oxide heterostructures have been the subject of many recent papers, both experimental and theoretical, as their interesting interface properties promise to pave the way towards novel electronic devices. With the current available experimental techniques, oxide thin films can be produced with a high degree of crystallinity, and the electronic structure of their surfaces and interfaces can be precisely determined. The most studied system of this type has been  $\text{LaAlO}_3/\text{SrTiO}_3$  (LAO/STO) that consists of two perovskite structures stacked along the (001) direction [1, 2], in which they present alternate layers of LaO,  $\text{AlO}_2$ ,  $\text{TiO}_2$ , and SrO with a very small lattice mismatch between them. A similar but less studied interface is that of LAO with  $\text{TiO}_2$  anatase that presents an even smaller lattice mismatch, namely less than 0.1%, along the (001) direction [3].  $\text{TiO}_2$  is a key material for most applications, including catalytic and optical devices, sensors, optoelectronics, and spintronics. Anatase thin films are frequently grown over LAO by pulsed laser deposition. It seems therefore important to perform a careful characterization, both from theory and experiments, of the film/substrate interface. Just to

mention one example where this study may be relevant, room temperature ferromagnetism has been obtained from doped and undoped anatase films grown over LAO, and the results strongly depend on the growth conditions [4].

There are two possible interfaces for the system LAO/ $\text{TiO}_2$ -anatase, namely, LaO facing  $\text{TiO}_2$  and  $\text{AlO}_2$  facing  $\text{TiO}_2$  [5, 6]. Due to the ionicity of the component oxides and, in particular, to the fact that the layers of LAO ( $\text{AlO}_2$  and LaO) have alternating formal charges ( $-1$  and  $+1$ , resp.), there is an interfacial formal excess charge that should be compensated either by the presence of terraces with different stacking, or by oxygen vacancies or by atomic interdiffusion.

Experimental work [6] has shown that, in the case of LAO/ $\text{TiO}_2$ -anatase, terraces with both types of interfaces appear and approximately in the same proportion. For the theoretical modeling of this system, the fact that the  $\text{TiO}_2$ -anatase layers along the (001) direction are not strictly planar must be taken into account. As a consequence, the anatase interface can be either oxygen terminated and thus neutral (with formal valence +4 for the interfacial Ti ion), or Ti-terminated. The latter situation is equivalent to considering surface oxygen vacancies and gives rise to a change in the valence of the interfacial Ti ion.

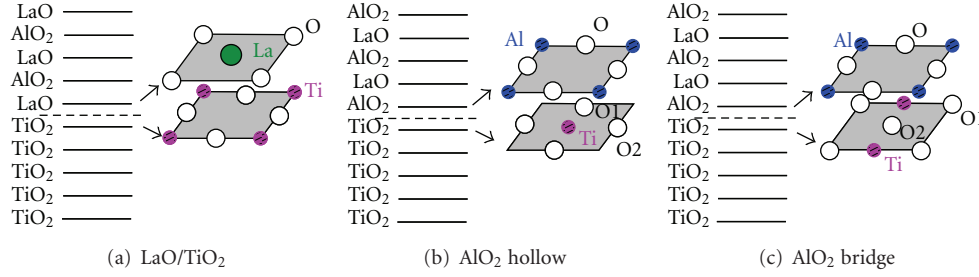


FIGURE 1: Slab structures for three low energy configurations. (a) interface LaO/TiO<sub>2</sub>; (b) interface AlO<sub>2</sub>/TiO, with Ti atom in the hollow position; (c) interface AlO<sub>2</sub>/TiO, with Ti atom in the bridge position. Oxygen atoms are coplanar with La and Al ions and 0.4 Å off-plane in the Ti layers. O1 and O2 are below and above the Ti plane, respectively. Oxygen O2 is closer to LAO, and it is removed in cases (b) and (c).

In this paper, we study the electronic and magnetic properties of interfaces for different stackings of LAO/TiO<sub>2</sub> using density functional theory [7] in the local density approximation (LSDA) and also considering electronic correlations in the framework of the LSDA+U approximation.

## 2. Method of Calculation

To simulate the interfaces, we use a periodically repeated slab geometry with 5 layers of each of the component materials and enough empty space between slabs so that they do not interact with each other (see Figure 1). The cell parameters in the plane of the interface are kept fixed to those of the experimental bulk LAO (3.79 Å) [3], and the positions of all atoms are allowed to relax in the out-of-plane direction until the forces are smaller than 0.05 eV/Å.

As in our previous work [5, 8], we use an odd number of layers of LAO to avoid the formation of a large dipole moment, but we are aware that with this procedure it is difficult to assure whether the interface will be conducting or not. The reason lies in the fact that an LSDA calculation for a positively (negatively) charged system will locate the Fermi level in the conduction (valence) band.

We use the Wien2k code, that is, an implementation of the full-potential linear-augmented plane waves method (FP-LAPW) [9]. The calculations are scalar relativistic, and the parameters used are listed in [10]. It is well known that in the case of oxides there is a band gap underestimation when using local exchange correlation functionals within density functional methods. For this reason, we have performed calculations with both the LSDA and the LSDA+U approximations [11], using  $U = 0.4$  Ry for the Ti  $d$  orbitals [8, 12], as in previous works. The comparison between the two procedures will evidence whether there is a qualitative difference in the interfacial properties due to electron correlations as, for example, a change in the valence of the Ti ions.

## 3. Results

The total energies of different possible structures (at 0K and with collinear spins) have been evaluated in previous works [5, 6], and in this paper, we present the results for

the lowest energy ones. For the interface in which LaO faces TiO<sub>2</sub> (Figure 1(a)), the oxygen termination for anatase is preferred. However, when AlO<sub>2</sub> faces TiO<sub>2</sub>, the lower energy is for the Ti termination, thus with oxygen vacancies [5, 6]. Two types of Ti-terminated interfaces are studied: one where the interfacial Ti atom faces the hollow site of the Al atoms in the AlO<sub>2</sub> layer (Figure 1(b)) and another one where the Ti atom faces a bridge position of the Al sites in the AlO<sub>2</sub> plane (Figure 1(c)).

In all the cases considered, there is a total formal charge of +1 arising in (a) from the LAO slab, while in cases (b) and (c), it is due to the contribution of both the LAO slab and the oxygen vacancy in the anatase slab. We point out that there are more possible structures for each type of stacking, and that in this work, we consider three of the lowest-energy ones, those that require more energy to separate LAO from anatase. LaO/TiO<sub>2</sub> has the lowest energy, followed by AlO<sub>2</sub>/TiO where oxygen vacancies are present [13] (i.e., O2 is removed in Figures 1(b) and 1(c)). In the hollow structure, one oxygen atom from the AlO<sub>2</sub> layer moves towards the interfacial Ti, thus increasing its number of neighbors. This relaxation decreases the total energy of the system with respect to the bridge structure by 0.2 eV in LSDA and 0.4 eV in LSDA+U.

Figure 2 shows the densities of states (DOSs) for the three structures depicted in Figure 1. We present the results for the LSDA+U approximation as they are similar to the LSDA ones, and if there are any differences, they are mentioned in the text. On the left side of Figure 2, we present the total DOS and the partial contributions from the La atoms. On the right side, the DOSs projected on the Ti atoms are shown in a zoomed-in region close to the Fermi energy ( $E_f$ ). As in the case of pure anatase, the valence band is mostly from the oxygen atoms and the conduction band from the Ti atoms, with the  $d$  orbitals clearly separated by symmetry: the  $t_{2g}$  levels closer to  $E_f$  and the  $e_g$  ones at higher energies. There are no Al states close to  $E_f$ , but oxygen atoms from LAO contribute significantly to the higher-energy part of the valence band.

**3.1. LaO/TiO<sub>2</sub> Interface.** In this interface (Figure 1(a)),  $E_f$  is in the conduction band, as expected due to the formal charge in the LAO slab. The largest contribution to the occupied states close to  $E_f$  comes from the interfacial Ti ion, and the rest of the Ti atoms contribute less as the

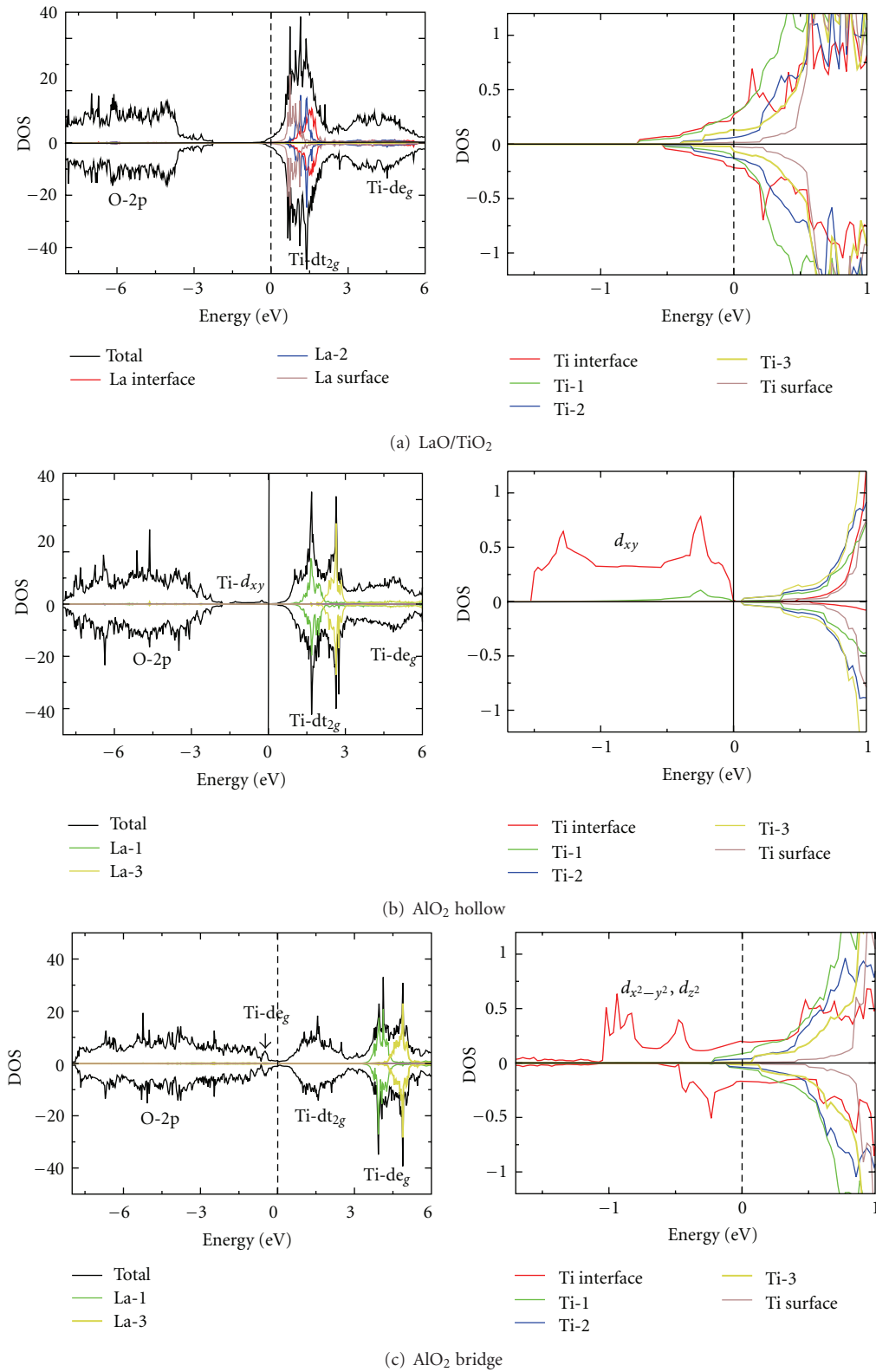


FIGURE 2: Densities of states for the three slabs of Figure 1 in the LSDA+U approximation. (a) Top: LaO/TiO<sub>2</sub>, (b) middle: AlO<sub>2</sub> hollow, (c) bottom: AlO<sub>2</sub> bridge. The Fermi level ( $E_f$ ) is marked by the dotted vertical line. Positive and negative values correspond to majority and minority spins, respectively. Left: total densities of states of the slabs and La levels. Right: partial DOS on the Ti atoms zoomed-in around  $E_f$ . In the legend the numbers by the atoms indicate the number of planes away from the interface.

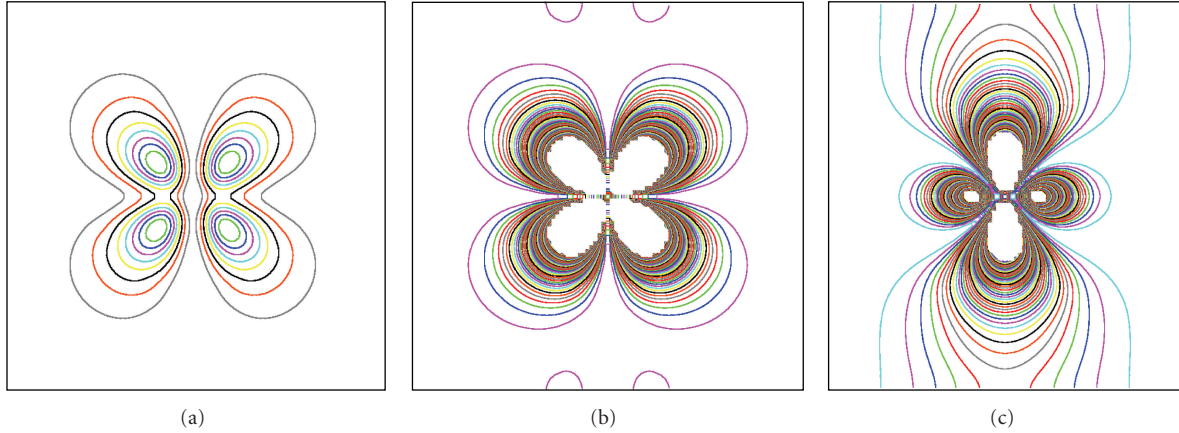


FIGURE 3: LSDA+U charge density of states close to  $E_f$  in the plane defined by the Ti-Ti bonds for one unit cell. The occupied states in the energy range:  $[E_f - 1.5 \text{ eV}, E_f]$  are plotted for the three structures in Figure 1, namely, (a) LaO/TiO<sub>2</sub>, (b) AlO<sub>2</sub> hollow, and (c) AlO<sub>2</sub> bridge. Charge isolines are spaced 0.01, from 0.01 to 1.00. In each case, the Ti interfacial atom is placed at the center of the figure, so as to make them comparable.

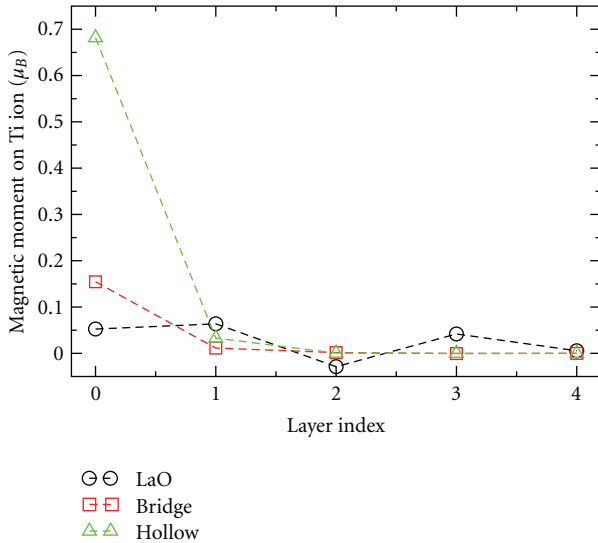


FIGURE 4: Magnetic moment inside the Ti muffin-tin spheres as a function of the penetration in the anatase slab. The interface is at layer 0, and the surface is at layer 4.

distance to the interface increases, as shown in Figure 2 (top right). This is true for both LSDA and LSDA+U approximations. It is interesting to note that similar layer-projected DOSs were obtained for LAO/STO [14] even though in that structure, the TiO<sub>2</sub> planes alternate with SrO layers. The authors also find that the charge distribution is not affected by the inclusion of correlation. There is certainly no contribution from the interfacial La ions to the occupied states, as that peak is shifted towards the right when compared with the La atom at the free surface of the slab (see Figure 2(a)). The charge density at the interface is plotted in Figure 3(a) and shows clearly the shape of the Ti  $d$  orbitals. The main occupation comes from  $d_{xz}$  and  $d_{3z^2-r^2}$ . A

small total magnetic moment is obtained for the unit cell, distributed among all the Ti atoms (see Figure 4).

**3.2. AlO<sub>2</sub>/TiO-Hollow Interface.** This interface (Figure 1(b)), presents a difference between LSDA and LSDA+U approximations. In LSDA+U, the majority spin of the interfacial Ti  $d_{xy}$  orbital shifts towards lower energies, so that the system becomes a semiconductor with a small gap of 0.1 eV (see Figure 2(b)). This shift is smaller in the LSDA, so that the system is metallic. In Figure 3(b), we show the charge density at the anatase side of the interface where the  $d_{xy}$  symmetry is evident. Both the charge and the magnetic moment at the Ti ions are large at the interface and decrease abruptly inside the anatase slab (see Figure 4).

**3.3. AlO<sub>2</sub>/TiO-Bridge Interface.** In this interface (Figure 1(c)),  $E_f$  lies in the conduction band, and the La peaks are further away from it, overlapping the  $t_{2g}$  orbitals of the Ti atoms. The same result is obtained with LSDA. The interfacial Ti orbitals have different symmetry from those of the hollow case, being of  $e_g$  character:  $d_{x^2-y^2}$  and  $d_{3z^2-r^2}$ , as can be seen in Figure 2 and Figure 3. In this case, the  $e_g$  levels split into two regions: one occupied band close to  $E_f$  and another one at energies above the  $t_{2g}$  orbitals, in the conduction band. The extra charge and the magnetic moment are both localized at the interface, near the oxygen vacancy, and their magnitude decreases abruptly inside the anatase slab as can be seen in Figure 4. In this case, the interfacial Ti formal valence and the magnetic moment are smaller than in the hollow structure.

It is interesting to note that in AlO<sub>2</sub>/TiO interfaces, there is no contribution of the Ti atom at the free surface in the occupied region of the conduction band, showing that a slab with 5 layers is a good enough approximation to account for interface properties.

There has been some controversy concerning the appearance of interfacial ferromagnetism in the LAO/STO interface

[15], which may also be the case here. For this reason, we performed calculations with a double-size unit cell (54 atoms), for the  $\text{AlO}_2/\text{TiO}$  interfaces which present localized magnetism at the interface. We studied the magnetic interaction between the interfacial Ti atoms within the LSDA+U method, setting them both in parallel and antiparallel configurations. The two solutions exist, but the antiparallel one is lower in energy, indicating that a long-range ferromagnetic interaction will not arise from the considered concentration and distribution of oxygen vacancies in  $\text{AlO}_2/\text{TiO}$  interfaces. We do not exclude the possibility of ferromagnetism in  $\text{LaO}/\text{TiO}_2$ , but it would be minor, and due to the fact that all the Ti atoms have local magnetic moments, many magnetic configurations should be considered for this study.

To explore the consequences of a lower vacancy concentration, and also of a formally neutral system, we considered the double-size unit cell in the hollow configuration with only one interfacial oxygen vacancy. In this calculation, none of the Ti ions resulted  $\text{Ti}^{+3}$ , and no magnetic moments appeared. Thus, a charge imbalance is needed to obtain  $\text{Ti}^{+3}$  ions and is also a necessary (but not sufficient) condition for the appearance of magnetism.

#### 4. Conclusions

The principal conclusion of this work is that whatever the origin of the charge at the interfaces, its main effect is to change the valence of the Ti atoms, either if it is due to the layered structure of LAO or to the presence of oxygen vacancies in anatase.

In  $\text{AlO}_2/\text{TiO}$ , there are interfacial oxygen vacancies, and the interfacial Ti atom close to the vacancy position acquires an extra charge. In  $\text{LaO}/\text{TiO}_2$ , there are no oxygen vacancies as they are not electrostatically favored, and the extra charge is distributed among all Ti atoms, with decreasing value as the distance from the interface increases. Our results indicate that the  $\text{LaO}/\text{TiO}_2$  interface spans through several anatase layers, while the  $\text{AlO}_2/\text{TiO}$  one is more localized and presents large local magnetic moments.

In experimental samples, coexistence of the studied interfaces and possibly others as well is expected. As a consequence, small patches with different magnetic order might appear [16], thus giving rise to sample-dependent results.

#### Acknowledgments

The authors thank R. Weht for a careful reading of the paper. M. Weissmann and V. Ferrari are members of CONICET-Argentina and acknowledge support by Grant PIP-CONICET00038.

#### References

- [1] P. Zubko, S. Gariglio, M. Gabay, P. Ghosez, and J. M. Triscone, "Interface physics in complex oxide heterostructures," *Annual Review of Condensed Matter Physics*, vol. 2, pp. 141–165, 2011.
- [2] R. Pentcheva and W. E. Pickett, "Electronic phenomena at complex oxide interfaces: insights from first principles,"

*Journal of Physics: Condensed Matter*, vol. 22, no. 4, Article ID 043001, 2010.

- [3] S. I. Kitazawa, Y. Choi, S. Yamamoto, and T. Yamaki, "Rutile and anatase mixed crystal  $\text{TiO}_2$  thin films prepared by pulsed laser deposition," *Thin Solid Films*, vol. 515, no. 4, pp. 1901–1904, 2006.
- [4] S. A. Chambers, "Epitaxial growth and properties of doped transition metal and complex oxide films," *Advanced Materials*, vol. 22, no. 2, pp. 219–248, 2010.
- [5] M. Weissmann and V. Ferrari, "Ab initio study of a  $\text{TiO}_2/\text{LaAlO}_3$  heterostructure," *Journal of Physics: Conference Series*, vol. 167, no. 1, Article ID 012060, 2009.
- [6] Z. Wang, W. Zeng, L. Gu, M. Saito, S. Tsukimoto, and Y. Ikuhara, "Atomic-scale structure and electronic property of the  $\text{LaAlO}_3/\text{TiO}_2$  interface," *Journal of Applied Physics*, vol. 108, no. 11, Article ID 113701, 2010.
- [7] P. Hohenberg and W. Kohn, "Inhomogeneous electron gas," *Physical Review*, vol. 136, no. 3B, pp. B864–B871, 1964.
- [8] M. Weissmann, V. Ferrari, and A. Saul, "Ab initio study of magnetism at the  $\text{TiO}_2/\text{LaAlO}_3$  interface," *Journal of Materials Science*, vol. 45, no. 18, pp. 4945–4951, 2010.
- [9] P. Blaha, K. Schwarz, G. K. H. Madsen, D. Kvasnicka, and J. Luitz, *WIEN2k, An Augmented Plane Wave + Local Orbitals Program for Calculating Crystal Properties*, (Karlheinz Schwarz, Technology Universität Wien, Vienna, Austria, 2001.
- [10] For the FP-LAPW calculations we use the following parameters: Atomic sphere radii of 1.7 Bohr for Ti and Al, 1.4 Bohr for O and 2.5 for La. The convergence control parameter RKmax is chosen to be 6, that corresponds to an energy cutoff of 250 eV. The employed vacuum space between slabs is 20 Å.
- [11] V. I. Anisimov, I. V. Solov'ev, M. A. Korotin, M. T. Czyzyk, and G. A. Sawatzky, "Density-functional theory and NiO photoemission spectra," *Physical Review B*, vol. 48, no. 23, pp. 16929–16934, 1993.
- [12] M. Weissmann and R. Weht, "Electronic and magnetic properties of the different phases of  $\text{Ti}_4\text{O}_7$  from density functional theory," *Physical Review B*, vol. 84, no. 14, Article ID 144419, 4 pages, 2011.
- [13] In this work the number of vacancies considered is large, but the simulation of smaller vacancy concentrations would imply, due to the anatase structure, to start from corrugated interfaces that may be the the subject of future work.
- [14] K. Janicka, J. P. Velez, and E. Y. Tsymal, "Quantum nature of two-dimensional electron gas confinement at  $\text{LaAlO}_3/\text{SrTiO}_3$  interfaces," *Physical Review Letters*, vol. 102, no. 10, Article ID 106803, 4 pages, 2009.
- [15] M. R. Fitzsimmons, N. W. Hengartner, S. Singh et al., "Upper limit to magnetism in  $\text{LaAlO}_3/\text{SrTiO}_3$  heterostructures," *Physical Review Letters*, vol. 107, no. 21, Article ID 217201, 5 pages, 2011.
- [16] J. A. Bert, B. Kalisky, C. Bell et al., "Direct imaging of the coexistence of ferromagnetism and superconductivity at the  $\text{LaAlO}_3/\text{SrTiO}_3$  interface," *Nature Physics*, vol. 7, pp. 767–771, 2011.

## Research Article

# Effect of Titanium Substitution on Magnetic Properties and Microstructure of Nanocrystalline Monophase Nd-Fe-B Magnets

Wang Cong,<sup>1</sup> Guo ZhiMeng,<sup>1</sup> Sui YanLi,<sup>2</sup> Bao XiaoQian,<sup>2</sup> and Chen ZhiAn<sup>3</sup>

<sup>1</sup>Department of Materials Engineering, University of Science and Technology Beijing, Beijing 100083, China

<sup>2</sup>State Key Laboratory for Advanced Metals and Materials, University of Science and Technology Beijing, Beijing 100083, China

<sup>3</sup>Beijing Zhong Ke San Huan Hi-Tech Co., Ltd., Beijing 100190, China

Correspondence should be addressed to Sui YanLi, yls@ustb.edu.cn

Received 1 March 2012; Revised 1 April 2012; Accepted 9 April 2012

Academic Editor: Ovidiu Crisan

Copyright © 2012 Wang Cong et al. This is an open access article distributed under the Creative Commons Attribution License, which permits unrestricted use, distribution, and reproduction in any medium, provided the original work is properly cited.

Nd<sub>12.3</sub>Fe<sub>81.7-x</sub>Ti<sub>x</sub>B<sub>6.0</sub> ( $x = 0.5-3.0$ ) ribbons have been prepared by rapid quenching and subsequent annealing treatment. Effect of Ti substitution and annealing treatment on the microstructure, magnetic properties, and crystallization behavior of the ribbons was systematically investigated by the methods of differential scanning calorimeter (DSC), X-ray diffraction (XRD), transmission electron microscopy (TEM), and vibrating sample magnetometer (VSM). It is found that Ti addition may increase the crystallization temperature and stabilize the amorphous phase. Ti element inhibits the grain growth during crystallization process and finally refines the microstructure. The exchange coupling interactions and magnetic properties of the ribbons increase with increasing  $x$  from 0.5 to 1 and then decrease with further increasing  $x \geq 1.5$ . Optimum magnetic properties with  $(BH)_{\max} = 151.6 \text{ kJ/m}^3$ ,  $H_{\text{ci}} = 809.2 \text{ kA/m}$ ,  $J_r = 1.02 \text{ T}$  are achieved in the Nd<sub>12.3</sub>Fe<sub>80.7</sub>Ti<sub>1</sub>B<sub>6.0</sub> ribbons annealed at 600°C for 10 min.

## 1. Introduction

Nanocomposite Nd-Fe-B permanent magnets have attracted considerable attention as a probable new generation of permanent magnets because of their high remanence, high maximum energy product, and low cost [1, 2]. The presence of the soft phases such as  $\alpha$ -Fe and Fe<sub>3</sub>B increases the remanence but the coercive field is decreased, so that their application is limited [3]. The alloys with Nd content higher than 11 at %, that is, close to the stoichiometry composition of Nd<sub>2</sub>Fe<sub>14</sub>B and usually believed to be single phase structure, are being studied to further improve coercivity. Since the discovery of the nanocrystalline Nd-Fe-B magnets, extensive efforts have been made to improve magnetic properties of Nd<sub>2</sub>Fe<sub>14</sub>B-based magnets [4–6]. However, the obtainable  $(BH)_{\max}$  is still significantly lower than that predicted by theory. This phenomenon can be practically attributed to the difference between practical microstructure and theoretical model, which is of fine mixture of aligned hard magnetic grains and two ferromagnetic phases suitably dispersed, crystallographically, coherent, and mutually coupled. Elements such as Zr and Nb have been found to improve overall hard

magnetic properties effectively by refining the microstructure [7–10]. Chang et al. [11] have reported that Zr and Ti addition can modify phase constitution and refine the grain size of the Nd-Fe-Ti-Zr-B rod fabricated by direct casting method, and to lead to the enhancement of the magnetic properties of the rods. The effect of Ti&C addition on the phase composition, microstructure, magnetic properties, temperature characteristics, and corrosion behavior of rapid-quenched Nd-Fe-B alloy has been investigated [9, 10, 12]. The combined addition of Ti and other elements such as C and Zr has been discussed a lot. However, the report of the single addition of pure Ti to Nd-Fe-B alloy is seldom. In this work, we present our research about the crystallization behavior, microstructure, and magnetic properties of single-phase Nd<sub>12.3</sub>Fe<sub>81.7-x</sub>Ti<sub>x</sub>B<sub>6.0</sub> ribbons.

## 2. Experimental

The ingots with nominal composition of Nd<sub>12.3</sub>Fe<sub>81.7-x</sub>Ti<sub>x</sub>B<sub>6.0</sub> ( $x = 0, 0.5, 1.0, 1.5, 2.0, 2.5, 3.0$ ) were prepared by arc melting pure constituent elements under high-purity Ar atmosphere. The ingots were remelted four

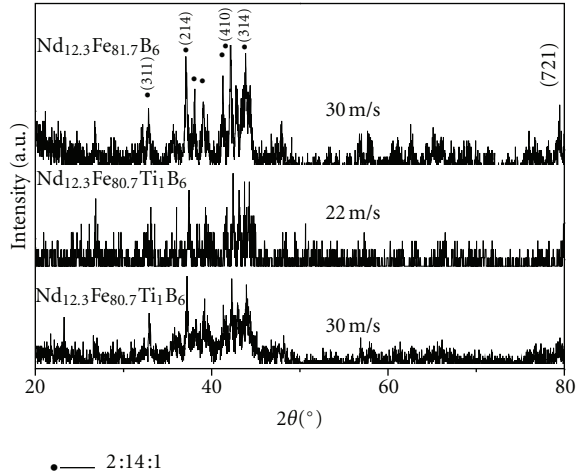


FIGURE 1: XRD patterns of  $\text{Nd}_{12.3}\text{Fe}_{81.7-x}\text{Ti}_x\text{B}_{6.0}$  ribbons quenched at various wheel speeds.

times to ensure homogeneity. Ribbons with a width of 2–4 mm and thickness of 30–50  $\mu\text{m}$  were obtained by ejecting the molten alloys from a quartz tube with an orifice diameter about 0.6 mm onto a copper wheel at a surface speed ( $V_s$ ) of 22 m/s. The melt spun ribbons were then sealed in a quartz tube under a vacuum of  $4 \times 10^{-3}$  Pa and annealed at 550–800°C for 10 min to crystallize and develop desired fine nanoscale microstructure. Thermal analysis of the ribbons was carried out using NETZSCHSTA449 differential scanning calorimeter at a heating rate of 10°C/min to determine the crystallization temperature. Phases' analysis of the samples was characterized by D/max-rB X-ray diffractometer (Cu  $K\alpha$  radiation). The microstructure of the ribbons was performed using with H-800 transmission electron microscopy (TEM). The thin foils for TEM observation were made by Ar-ion beam polishing. Hysteresis loops of the ribbons were measured using an LDJ 9600 vibrating sample magnetometer (VSM) with an applied field of up to 2 T (1600 kA/m). The length direction of the ribbons was parallel to the applied field in order to minimize the demagnetization effect. Wohlfarth's remanence analysis was employed to determine the strength of exchange-coupling interactions of the materials obtained.

### 3. Results and Discussion

**3.1. Phase Analysis.** Figure 1 shows XRD patterns of the as-spun  $\text{Nd}_{12.3}\text{Fe}_{81.7-x}\text{Ti}_x\text{B}_{6.0}$  ( $x = 0, x = 1$ ) ribbons with  $V_s$  of 22 m/s and 30 m/s. It can be seen that the ribbons are composed of amorphous phase and some  $\text{Nd}_2\text{Fe}_{14}\text{B}$  phase, and the quantity and the relative intensity of diffraction peak for 2:14:1 decreases with increasing  $V_s$  from 22 m/s to 30 m/s and the addition Ti element, suggesting that the amount of 2:14:1 phase decreases and amorphous phase increases with increasing  $V_s$  and Ti content. The ribbons with  $x = 0$  melt-spun by 30 m/s consist of hard magnetic 2:14:1 phase and some amorphous phase. The XRD patterns of the ribbons with  $x = 1.0$  melt-spun by 20 m/s and

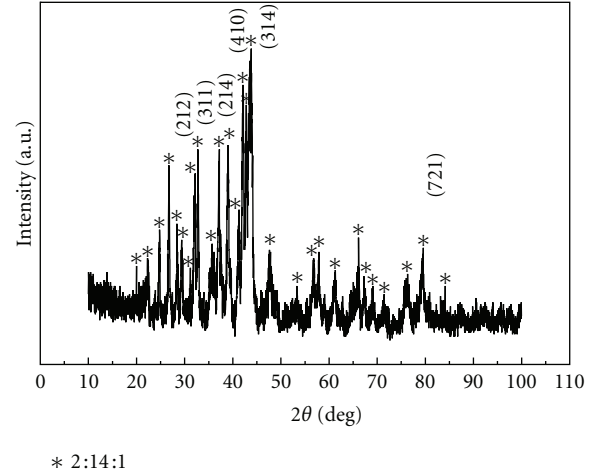


FIGURE 2: XRD patterns of as-cast  $\text{Nd}_{12.3}\text{Fe}_{80.7}\text{Ti}_1\text{B}_6$  alloy annealed at 1050°C for 10 h.

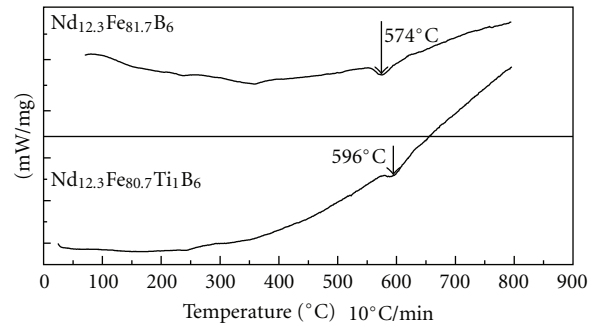


FIGURE 3: DSC curves of as-spun  $\text{Nd}_{12.3}\text{Fe}_{81.7-x}\text{Ti}_x\text{B}_{6.0}$  ribbons at 30 m/s.

30 m/s present primarily amorphous phase. This indicates that Ti addition improves significantly the amorphization tendency of  $\text{Nd}_{12.3}\text{Fe}_{81.7-x}\text{Ti}_x\text{B}_{6.0}$  alloys. Figure 2 shows XRD patterns of as-cast  $\text{Nd}_{12.3}\text{Fe}_{80.7}\text{Ti}_1\text{B}_6$  alloy annealed at 1050°C for 10 h. It can be seen that amorphous phase transforms completely to 2:14:1 phase.

#### 3.2. Effect of Ti on Crystallization Process and Microstructure.

Figure 3 shows the differential scanning calorimetry (DSC) curves of the melt-spun  $\text{Nd}_{12.3}\text{Fe}_{81.7-x}\text{Ti}_x\text{B}_{6.0}$  ribbons at a heating rate of 10 K/min from room temperature to 1073 K. The ribbons with  $x = 0$  and 1 show one exothermic peak corresponding to transformation from amorphous to 2:14:1 structure. Compared to the ribbon with  $x = 0$ , the crystallization temperature peak  $T_p$  for the ribbon with  $x = 1$  increases by approximately 20 K, indicating that Ti element enhances the thermal stability of amorphous phase in Nd-Fe-B alloy. Enrichment of Ti atoms along grain boundary stabilizes amorphous phase in the melt-spun and annealing process of the ribbons, which is believed to be a main reason that thermal stability is enhanced by Ti addition in the studied nanocrystalline  $\text{Nd}_{12.3}\text{Fe}_{81.7}\text{B}_6$  magnets.

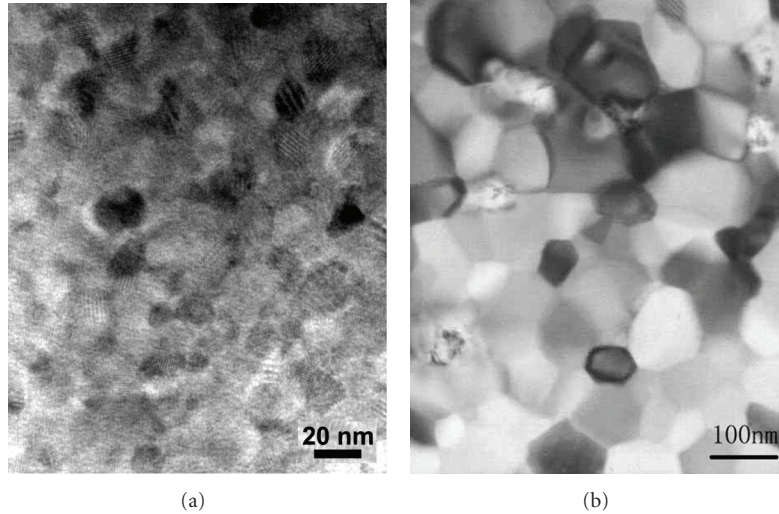


FIGURE 4: TEM images of  $\text{Nd}_{12.3}\text{Fe}_{80.7}\text{Ti}_1\text{B}_6$  (a) and  $\text{Nd}_{12.3}\text{Fe}_{81.7}\text{B}_6$  (b) ribbons annealed at  $600^\circ\text{C}$  for 10 min.

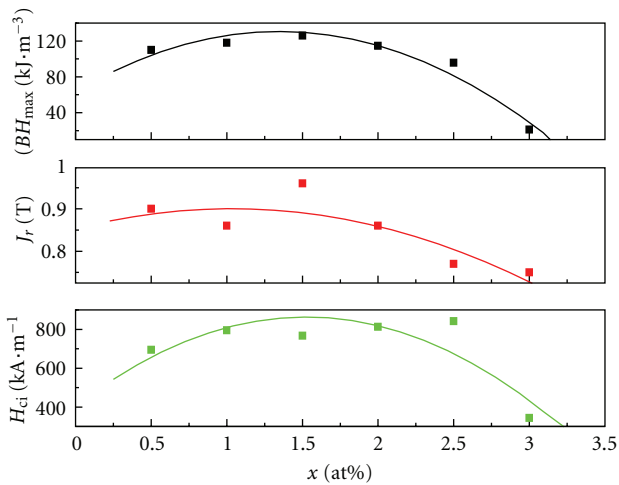


FIGURE 5: Variation of the  $J_r$ ,  $H_{ci}$  and  $(BH)_{\max}$  with Ti content of as-spun  $\text{Nd}_{12.3}\text{Fe}_{81.7-x}\text{Ti}_x\text{B}_{6.0}$  ribbons.

Figure 4 shows TEM bright field micrographs of (a)  $\text{Nd}_{12.3}\text{Fe}_{80.7}\text{Ti}_1\text{B}_6$  and (b)  $\text{Nd}_{12.3}\text{Fe}_{81.7}\text{B}_6$  ribbons annealed at  $600^\circ\text{C}$  for 10 min. The  $\text{Nd}_{12.3}\text{Fe}_{81.7}\text{B}_6$  alloy shows an average grain size of around 80 nm and the grain size distribution is nonuniform. Large grains up to about 260 nm are present in the microstructure of the sample, which decreases exchange coupling interactions between neighbor grains. The average grain size is estimated to be 25 to 35 nm for the  $\text{Nd}_{12.3}\text{Fe}_{80.7}\text{Ti}_1\text{B}_6$  alloy and the grains become more uniformly distributed. Thus, it can be concluded that the addition of a small amount of Ti to the ternary alloy is effective for reducing the grain size of the magnets, which enhances the coercive field and remanence. So the best magnetic property with  $(BH)_{\max} = 151.6 \text{ kJ/m}^3$  is obtained for the sample.

**3.3. Effect of Ti Content on Magnetic Properties of Ribbons.** The  $J_r$ ,  $H_{ci}$ , and  $(BH)_{\max}$  of the  $\text{Nd}_{12.3}\text{Fe}_{81.7-x}\text{Ti}_x\text{B}_{6.0}$  melt-spun ribbons by 22 m/s are shown in Figure 5. It is clear that

the magnetic properties of melt-spun ribbons increase first with increasing Ti content, reaching the maximum value at  $x = 1.5$ , and then decrease with further increasing Ti content. The sample with  $x = 3.0$  shows a very low coercivity and remanence.

The intrinsic coercivity  $H_{ci}$ , remanence polarization  $J_r$ , and maximum energy product  $(BH)_{\max}$  of the melt-spun ribbons are relatively low, which can be ascribed to incomplete crystallization of the ribbons, as evidenced by the superposition of broad peaks of amorphous precursor alloy and the characteristic of 2:14:1 peaks shown in Figure 1. In order to achieve the best magnetic properties for each alloy, a thermal treatment was employed individually to quenched ribbons to induce a fine grain structure crystallizing from the amorphous state. Figure 6 summarizes the effect of annealing temperature  $T_a$  and Ti content  $x$  on  $H_{ci}$ ,  $J_r$ , and  $(BH)_{\max}$  of  $\text{Nd}_{12.3}\text{Fe}_{81.7-x}\text{Ti}_x\text{B}_{6.0}$  ribbons. It can be seen that  $H_{ci}$ ,  $J_r$ , and  $(BH)_{\max}$  increase first with increasing  $T_a$  and Ti content  $x$ , until reaching the maximum values, then decrease with further increasing  $T_a$  and Ti content  $x$ . Optimum magnetic properties with  $(BH)_{\max} = 151.6 \text{ kJ/m}^3$ ,  $H_{ci} = 809.2 \text{ kA/m}$ ,  $J_r = 1.02 \text{ T}$  are achieved by annealing the melt-spun ribbons with  $x = 1.0$  at  $600^\circ\text{C}$  for 10 min, which are much higher than the magnetic properties of  $\text{Nd}_6\text{Pr}_1\text{Fe}_{80}\text{B}_{13}$  ribbons with Ti&C addition reported by Ohkubo et al. [13].

Table 1 shows the variation of the optimum  $J_r/J_s$ ,  $J_r$ ,  $H_{ci}$ , and  $(BH)_{\max}$  with Ti content of the  $\text{Nd}_{12.3}\text{Fe}_{81.7-x}\text{Ti}_x\text{B}_{6.0}$  ( $x = 0.5\text{--}3.0$ ) ribbons. It can be seen that Ti addition significantly affects the magnetic properties of the samples. The  $J_r/J_s$ ,  $J_r$ ,  $H_{ci}$ , and  $(BH)_{\max}$  of optimally processed  $\text{Nd}_{12.3}\text{Fe}_{81.7-x}\text{Ti}_x\text{B}_{6.0}$  ribbons initially increase with increasing Ti content from  $x = 0.5$  to 1.0, but all of them decrease with further increasing Ti content. The  $J_r$  and  $H_{ci}$  increase from 0.79 T and 616.1 kA/m for the sample with  $x = 0.5$  to 1.02 T and 809.2 kA/m for the sample with  $x = 1.0$ , respectively. The  $(BH)_{\max}$  of the 1.0 at.% Ti-doped sample increases from  $76.2 \text{ kJ/m}^3$  to  $151.6 \text{ kJ/m}^3$ . Ti elements are benefit to refine grain sizes and enhance exchange coupling

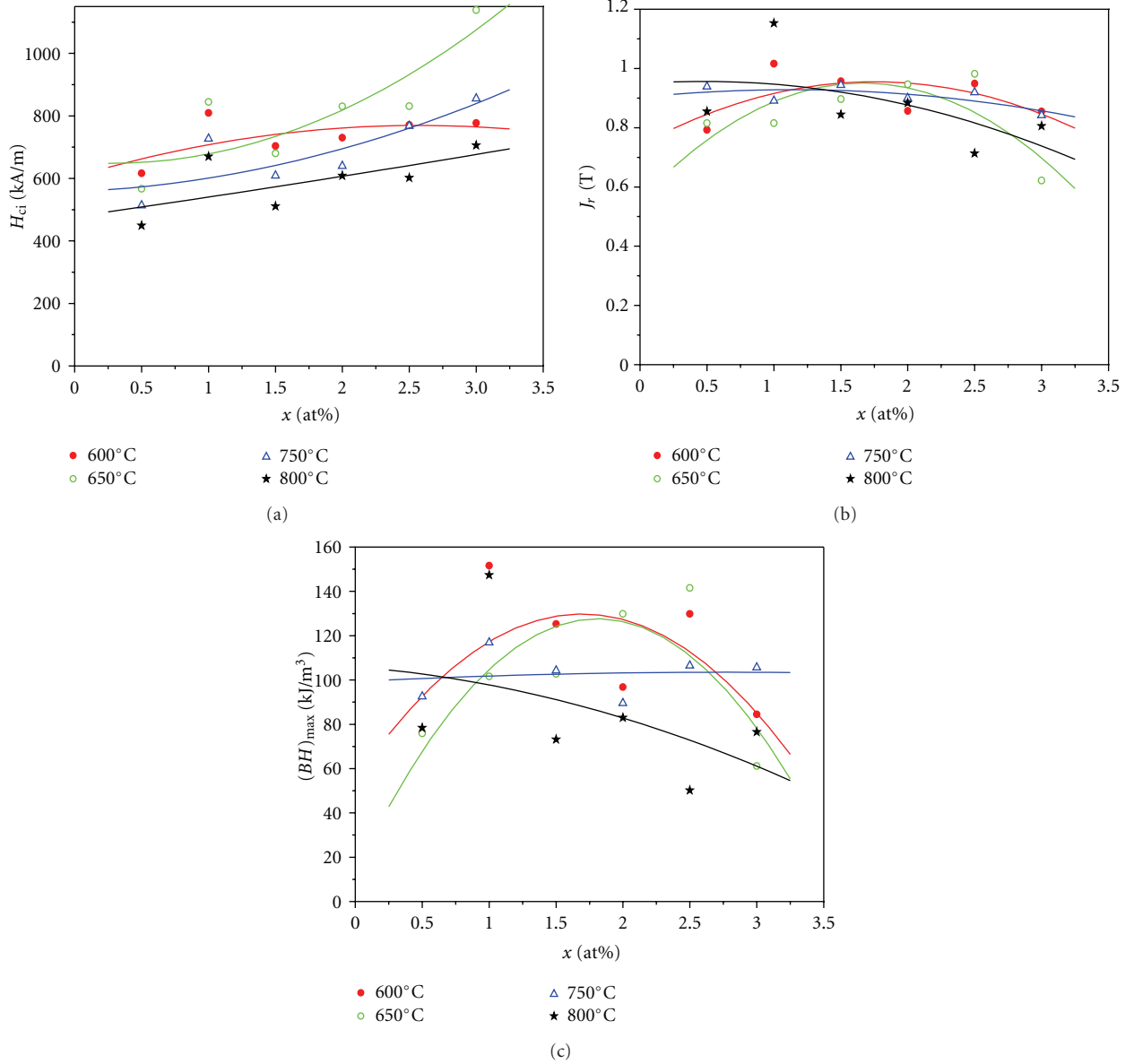


FIGURE 6: Magnetic properties of  $\text{Nd}_{12.3}\text{Fe}_{81.7-x}\text{Ti}_x\text{B}_{6.0}$  ribbons annealed at various temperatures for 10 min.

TABLE 1: Magnetic properties of  $\text{Nd}_{12.3}\text{Fe}_{81.7-x}\text{Ti}_x\text{B}_6$  ( $x = 0.5, 1.0, 2.0, 3.0$ ) ribbons annealed at  $600^\circ\text{C}$  for 10 min.

$x$	$(BH)_{\max}$ ( $\text{kJ}/\text{m}^3$ )	$H_{\text{ci}}$ ( $\text{kA}/\text{m}$ )	$J_r$ (T)	$J_r/J_s$
0.5	76.2	616.1	0.79	0.73
1.0	151.6	809.2	1.02	0.74
2.0	96.7	730.2	0.86	0.71
3.0	84.5	777.2	0.85	0.67

interactions between the neighbor grains. But the strength of exchange coupling interactions in the ribbons is determined by two opposite factors: (1) grain refinement and (2) magnetic dilution and grain isolation especially at higher Ti content.

**3.4. Effect of Ti on Exchange Coupling.** The exchange coupling interaction is often evaluated using  $\delta M$  plots, which can be defined as  $m_d(H) - (1 - 2m_r(H))$ ; where  $m_d$  is demagnetization remanence and  $m_r$  is isothermal magnetization remanence [14]. Both of these values are normalized by the saturation remanence. According to Wohlfarth's analysis, higher positive  $\delta M$  peaks indicate stronger exchange coupling interactions. Figure 7 shows the  $\delta M$  plots with respect to the applied magnetic field of the  $\text{Nd}_{12.3}\text{Fe}_{81.7-x}\text{Ti}_x\text{B}_{6.0}$  annealed ribbons, respectively. The positive peak in the  $\delta M$  plots suggests the existence of exchange coupling interaction between  $\text{Nd}_2\text{Fe}_{14}\text{B}$  and  $\text{Nd}_2\text{Fe}_{14}\text{B}$  phases. It can be seen that the strength of exchange coupling interaction is significantly enhanced at a dilute Ti-substitution (1.0 at.% Ti) and then weakened when Ti content is further increased. This trend

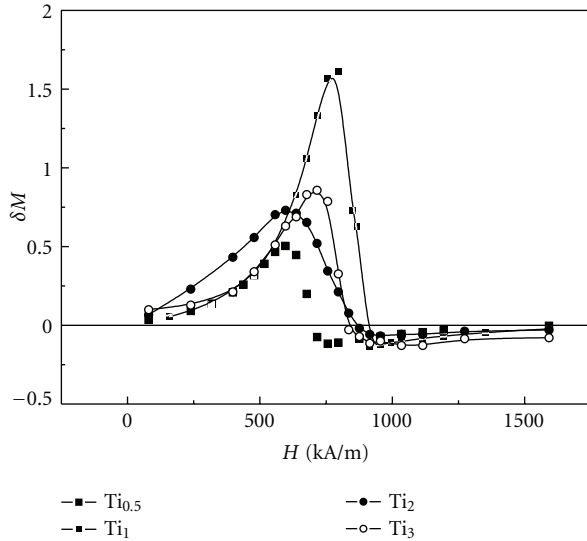


FIGURE 7: The  $\delta M(H)$  curves of  $\text{Nd}_{12.3}\text{Fe}_{81.7-x}\text{Ti}_x\text{B}_6$  ( $x = 0.5, 1.0, 2.0, 3.0$ ) ribbons annealed at  $600^\circ\text{C}$  for 10 min.

agrees well with the variation of magnetic properties with Ti content previously shown in Figure 6. Hence, the changes in magnetic properties of the samples on increasing Ti content may mainly arise from the variation of the exchange-coupling interaction in the samples. Meanwhile, it is worth noting that the decrease of saturation magnetization with increasing Ti content also contributes to the reduction of  $J_r$  and  $(BH)_{\text{max}}$ , in the samples with higher Ti substitution.

#### 4. Conclusion

The effect of Ti addition and annealing treatment on the magnetic properties and microstructure of nanocrystalline  $\text{Nd}_{12.3}\text{Fe}_{81.7-x}\text{Ti}_x\text{B}_{6.0}$  ( $x = 0.5-3.0$ ) alloys has been systematically investigated. The remanence polarization  $J_r$ , intrinsic coercivity  $H_{ci}$ , and maximum energy product  $(BH)_{\text{max}}$  of optimally processed  $\text{Nd}_{12.3}\text{Fe}_{81.7-x}\text{Ti}_x\text{B}_{6.0}$  ribbons increased first with an increase in Ti content, reached the maximum values at  $x = 1.0$ , then decreased with further increasing Ti content. The excellent magnetic properties with  $(BH)_{\text{max}} = 151.6 \text{ kJ/m}^3$ ,  $H_{ci} = 809.2 \text{ kA/m}$ ,  $J_r = 1.02 \text{ T}$  were obtained by annealing a melt-spun amorphous  $\text{Nd}_{12.3}\text{Fe}_{80.7}\text{Ti}_{1.0}\text{B}_{6.0}$  alloy at  $600^\circ\text{C}$  for 10 min. The variation of magnetic properties with increasing Ti content can be attributed to both the variation of the exchange coupling interactions and the decrease in saturation magnetization in the ribbons.

#### Acknowledgment

This work has been supported by the National Natural Science Foundation of China under Grant no. 51174030.

#### References

[1] E. F. Kneller and R. Hawig, "The exchange-spring magnet: a new material principle for permanent magnets," *IEEE Transactions on Magnetics*, vol. 27, no. 4, pp. 3588–3600, 1991.

[2] T. Schrefl, R. Fischer, J. Fidler, and H. Kronmüller, "Two- and three-dimensional calculation of remanence enhancement of rare-earth based composite magnets," *Journal of Applied Physics*, vol. 76, no. 10, pp. 7053–7058, 1994.

[3] C. P. Yang, Z. L. Jiang, X. Y. Chen et al., "Microstructure and magnetic properties of two-phase nanocomposite  $\text{Nd}_9\text{Fe}_{85.5}\text{Nb}_{1.0}\text{B}_{4.5-y}\text{Cy}$  ( $y = 0.5-4.5$ ) magnets," *Journal of Alloys and Compounds*, vol. 316, no. 1-2, pp. 269–274, 2001.

[4] Z. W. Liu and H. A. Davies, "The practical limits for enhancing magnetic property combinations for bulk nanocrystalline NdFeB alloys through Pr, Co and Dy substitutions," *Journal of Magnetism and Magnetic Materials*, vol. 313, no. 2, pp. 337–341, 2007.

[5] R. Gholamipour, A. Beitollahi, V. K. Marghussian, and T. Ohkubo, "Cu effects on coercivity and microstructural features in nanocrystalline Nd-Fe-Co-B annealed melt-spun ribbons," *Physica B*, vol. 398, no. 1, pp. 51–54, 2007.

[6] X. H. Li, Z. S. Gao, W. Li, K. W. Zhang, J. W. Zhang, and X. Y. Zhang, "Study of the microstructure of  $\alpha\text{-Fe/Nd}_2\text{Fe}_{14}\text{B}$  nanocomposites prepared by electropulsing heating amorphous NdFeCoB," *Materials Letters*, vol. 59, no. 22, pp. 2782–2785, 2005.

[7] R. Zhang, Y. Liu, J. Ye, W. Yang, Y. Ma, and S. Gao, "Effect of Nb substitution on the temperature characteristics and microstructures of rapid-quenched NdFeB alloy," *Journal of Alloys and Compounds*, vol. 427, no. 1-2, pp. 78–81, 2007.

[8] C. Wang, M. Yan, and W. Y. Zhang, "Significant changes in the microstructure, phase transformation and magnetic properties of  $(\text{Nd,Pr})_2\text{Fe}_{14}\text{B}/\alpha\text{-Fe}$  magnets induced by Nb and Zr additions," *Materials Science and Engineering B*, vol. 123, no. 1, pp. 80–83, 2005.

[9] A. D. Crisan, "Compositional studies and thermal analysis in amorphous and nanocrystalline FePtNbB melt spun ribbons," *Journal of Optoelectronics and Advanced Materials*, vol. 12, no. 2, pp. 250–256, 2010.

[10] M. Seqqat, M. Nogues, O. Crisan et al., "Magnetic properties of  $\text{Fe}_{100-x}\text{Sm}_x$  thin films and  $\text{Fe}_{80-x}\text{Sm}_x\text{B}_v$  thin films and ribbons," *Journal of Magnetism and Magnetic Materials*, vol. 157-158, pp. 225–226, 1996.

[11] H. W. Chang, C. H. Chiu, C. W. Chang, W. C. Chang, A. C. Sun, and Y. D. Yao, "Effect of Ti substitution on the magnetic properties, microstructure, and aftereffect of melt spun PrFeB nanocomposites," *Scripta Materialia*, vol. 55, no. 6, pp. 529–532, 2006.

[12] R. Zhang, Y. Liu, J. Li, S. Gao, and M. Tu, "Effect of Ti&C substitution on the magnetic properties and microstructures of rapidly-quenched NdFeB alloy," *Materials Characterization*, vol. 59, no. 5, pp. 642–646, 2008.

[13] T. Ohkubo, T. Miyoshi, S. Hirotsawa, and K. Hono, "Effects of C and Ti additions on the microstructures of  $\text{Nd}_9\text{Fe}_{77}\text{B}_{14}$  nanocomposite magnets," *Materials Science and Engineering A*, vol. 448–451, pp. 435–439, 2007.

[14] M. Nezakat, R. Gholamipour, A. Amadeh, A. Mohammadi, and T. Ohkubo, "Corrosion behavior of  $\text{Nd}_{9.4}\text{Pr}_{0.6}\text{Fe}_{bal}\text{Co}_6\text{B}_6\text{Ga}_{0.5}\text{Ti}_x\text{C}_x$  ( $x = 0, 1.5, 3, 6$ ) nanocomposites annealed melt-spun ribbons," *Journal of Magnetism and Magnetic Materials*, vol. 321, no. 20, pp. 3391–3395, 2009.

## Research Article

# Interlayer Thickness Effects on Magnetic Properties of X/FePtAg (X = FePt/Fe and Fe/FePt) Trilayers

Jai-Lin Tsai, Jian-Chiang Huang, and Hsueh-Wei Tai

*Department of Materials Science and Engineering, National Chung Hsing University, Taichung 402, Taiwan*

Correspondence should be addressed to Jai-Lin Tsai, tsaijl@dragon.nchu.edu.tw

Received 13 December 2011; Revised 7 February 2012; Accepted 2 March 2012

Academic Editor: Makis Angelakeris

Copyright © 2012 Jai-Lin Tsai et al. This is an open access article distributed under the Creative Commons Attribution License, which permits unrestricted use, distribution, and reproduction in any medium, provided the original work is properly cited.

A soft/hard FePt/Fe/FePtAg and Fe/FePt/FePtAg trilayers with perpendicular magnetization were prepared on a glass substrate. Inserting disordered FePt layer allowed modification of magnetic anisotropy of the Fe/FePtAg sharp interface to Fe/FePt/FePtAg stepwise interface. The out-of-plane coercivity field was modulated as a function of the FePt thickness because of the interface coupling attenuation between Fe and FePtAg. The coercivity was inversely proportional to the FePt thickness as evidenced by the pinning effect at the stepwise interface. Additionally, the out-of-plane magnetization was controlled by domain wall pinning effect. The in-plane magnetization reversal processes occurred in two steps like in exchange spring systems and attributed to the domain wall nucleation and its propagation from Fe/FePt layer into FePtAg layer.

## 1. Introduction

Exchange spring media and exchange coupled composite (ECC) media were introduced to reduce the write field requirement and maintain the same thermal stability and greater tolerance to easy axis distribution. ECC media and exchange spring media seem to be methods of achieving area densities of several (Tbit/in<sup>2</sup>) [1–5]. In ECC composite media, an intermediate nonmagnetic layer modulates the exchange coupling between the hard and soft phase. In exchange spring media, a direct exchange coupling between hard and soft phase occurs where the interface between hard- and soft-magnetic materials can be ideal or graded [6, 7]. Theoretically, the coercivity field is proportional to the gradient of the densities of domain wall energy [8–11]. In graded media, the switching field can be tuned and thus enhance the exchange coupling between the hard- and soft-magnetic layer. In experimental studies, the exchange-spring soft/hard bilayer has been discussed extensively in Fe/LL<sub>0</sub> FePt bilayer systems [12–16].

This work discusses, first, the Fe magnetic interlayer thickness effects on magnetic properties of (disordered FePt)/Fe/(ordered FePtAg) trilayer. Although, the addition of a ferromagnetic intermediate layer is not suitable to tailor the coupling efficiency of an exchange-coupled bilayer, this

study focuses on the effect of an additional soft magnetic layer and its effect on perpendicular magnetic anisotropy features. The interface effects are studied with the variations of in-plane and out-of-plane magnetic hysteresis loops. Second this work addresses the disordered FePt thickness effects on the magnetic properties of Fe/FePt/FePtAg trilayer. The variation of the out-of-plane coercivity was fitted by a model considering domain wall pinning and nucleation. The shape of in-plane demagnetization curves is varying with FePt thickness and correlated with inverse domain nucleation and corresponding domain wall propagation.

## 2. Experimental Procedures

The FePt(2 nm)/Fe(*t*)/FePtAg(10 nm) (*t* = 0, 0.5, 1, 2, 3, 5 nm) and Fe(2 nm)/FePt(*t* nm)/(FePtAg)(10 nm) (*t* = 0, 1, 3, 5, 7 nm) trilayers were fabricated with DC (direct current) magnetron sputtering. The base pressure of the sputtering system was  $2 \times 10^{-8}$  Torr and the working pressure was  $1.5 \times 10^{-3}$  Torr under high purity argon gas. The FePt alloy target and Ag element target were used and the Ag(1 nm)/FePt(10 nm) bilayer was deposited on a glass substrate. The film chemical composition was Fe<sub>48</sub>Pt<sub>52</sub> measured by energy dispersive spectroscopy (EDS). After

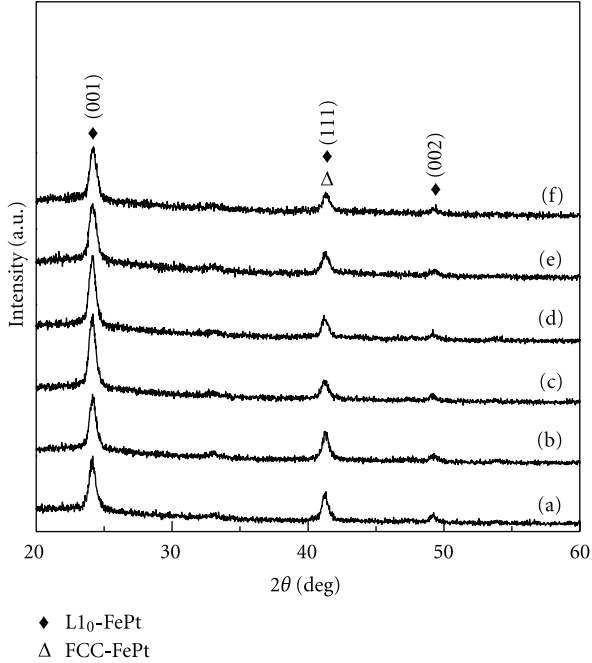


FIGURE 1: GID patterns of (a) FePt/FePtAg film, FePt/Fe(*t*)/(FePtAg) film, (b) *t* = 0.5 nm, (c) *t* = 1 nm, (d) *t* = 2 nm, (e) *t* = 3 nm, (f) *t* = 5 nm.

deposition, the films were annealed by a rapid thermal process (RTP) at 800°C for 3 minutes and formed the FePtAg alloy film. There are two types of soft magnetic structures fabricated following two different procedures. Procedure I: Fe layer with different thicknesses from 0.5 nm to 5 nm was deposited on L1<sub>0</sub>FePtAg at room temperature and capped with 2 nm of a disordered FePt layer. Finally, the FePt/Fe/FePtAg sandwich layer structure was formed. Procedure II: FePt layer was deposited on L1<sub>0</sub>FePtAg layer and finally Fe layer with thickness of 2 nm was deposited on disordered FePt (*t* nm) layer at room temperature. The crystal structure of the samples was identified using grazing incident X-ray diffraction (GID) with Cu K<sub>α</sub> radiation and a standard X-ray diffraction (XRD) technique (BRUKER, D8 Discover). Magnetic hysteresis loops were measured at room temperature using a vibration sample magnetometer (VSM, Lakeshore 7400) with a maximum magnetic field of 2 Tesla. The film microstructure was observed using transmission electron microscopy (TEM, Philips Tecnai F30).

### 3. Results and Discussion

From standard XRD pattern in previous work, the (001) superlattice diffraction peak and the (002) fundamental reflection of the L1<sub>0</sub> FePt are clearly observed in FePtAg film [17, 18]. The XRD profiles suggest that the L1<sub>0</sub> FePt crystal has a [001] texture. The ordering parameter, *S* can be estimated from  $0.492[I(001)/I(002)]^{1/2}$ ,  $\{[(I(001)/I(002))_{\text{obs}}/I(001)/I(002)_{\text{cal}}]\}^{1/2}$  or is proportional to the ratio  $I(001)/I(002)$  [19]. The GID was used to tailor the surface structure variation of Fe/(disordered FePt) or (disordered FePt)/Fe layer. Figure 1 show GID patterns

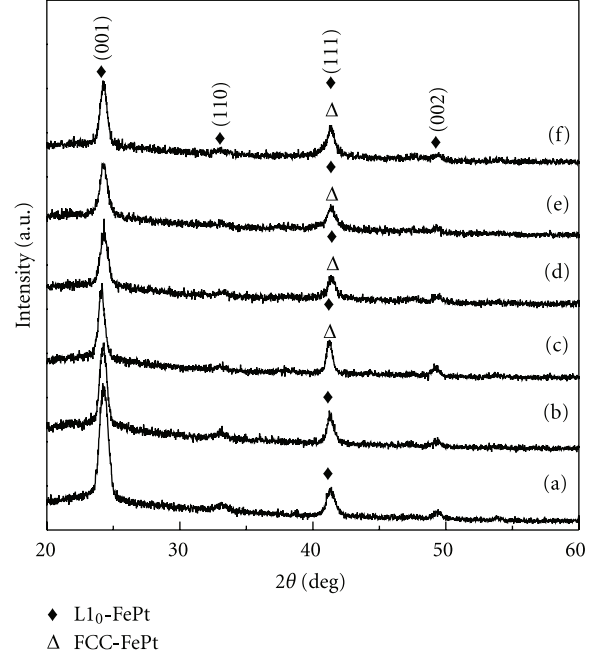


FIGURE 2: GID patterns of (a) Fe/(FePtAg) film, Fe/FePt(*t* nm)/(FePtAg) film, (b) *t* = 1 nm, (c) *t* = 3 nm, (d) *t* = 5 nm, (e) *t* = 7 nm.

of FePt/Fe(*t*)/(FePtAg) (*t* = 0, 0.5, 1, 2, 3, 5 nm) films. In Figure 1(a), the FePt/FePtAg bilayer was preferred oriented at [001] direction and the relative intensity of (111) peak was low. Without the intermediate Fe layer, the interface anisotropy variation between FePt and FePtAg layer was expected to be sharp. In Figures 1(b)–1(f), the Fe layer with thickness 0.5, 1, 2, 3, or 5 nm was inserted between FePt/FePtAg bilayer. The relative intensity of diffraction peaks were almost not changed when the Fe layer was inserted. The FePt/Fe/FePtAg trilayers have (001) texture and the (111) diffraction peaks were the summation of disordered FePt and ordered FePtAg layers. Figure 2 show GID patterns of Fe(2 nm)/FePt(*t* nm)/(FePtAg)(10 nm) (*t* = 0, 1, 3, 5, 7 nm) films. In Figures 2(a)–2(b), the FePtAg single layer and Fe/FePtAg bilayer was preferred oriented at [001] direction and the relative intensity of (111) peak was low. Without disordered FePt intermediate layer, it is supposed that the interface anisotropy between Fe and FePtAg layer was sharp. In Figures 2(c)–2(f), the FePt layer with thickness of 1, 3, 5 or 7 nm was inserted between Fe/FePtAg bilayer. When the thickness of disordered FePt layer increased to 3, 5, 7 nm, the (111) diffraction peak was become rough and the full width of half maximum (FWHM) of (111) peak was increased. The disordered FePt phase existed and was proved in the variation of (111) peak. The interface anisotropy was stepwise from ordered FePtAg to disordered FePt and Fe layer. To prove the layer structure of films, the cross-section TEM images of Fe/FePtAg bilayer and Fe/FePt(3, 5 nm)/FePtAg trilayers were shown in Figure 3. With increased FePt thickness, the interface between Fe/FePt bilayer became rough but the smooth interface between FePt/FePtAg was maintained as shown in Figures 3(b)–3(c).

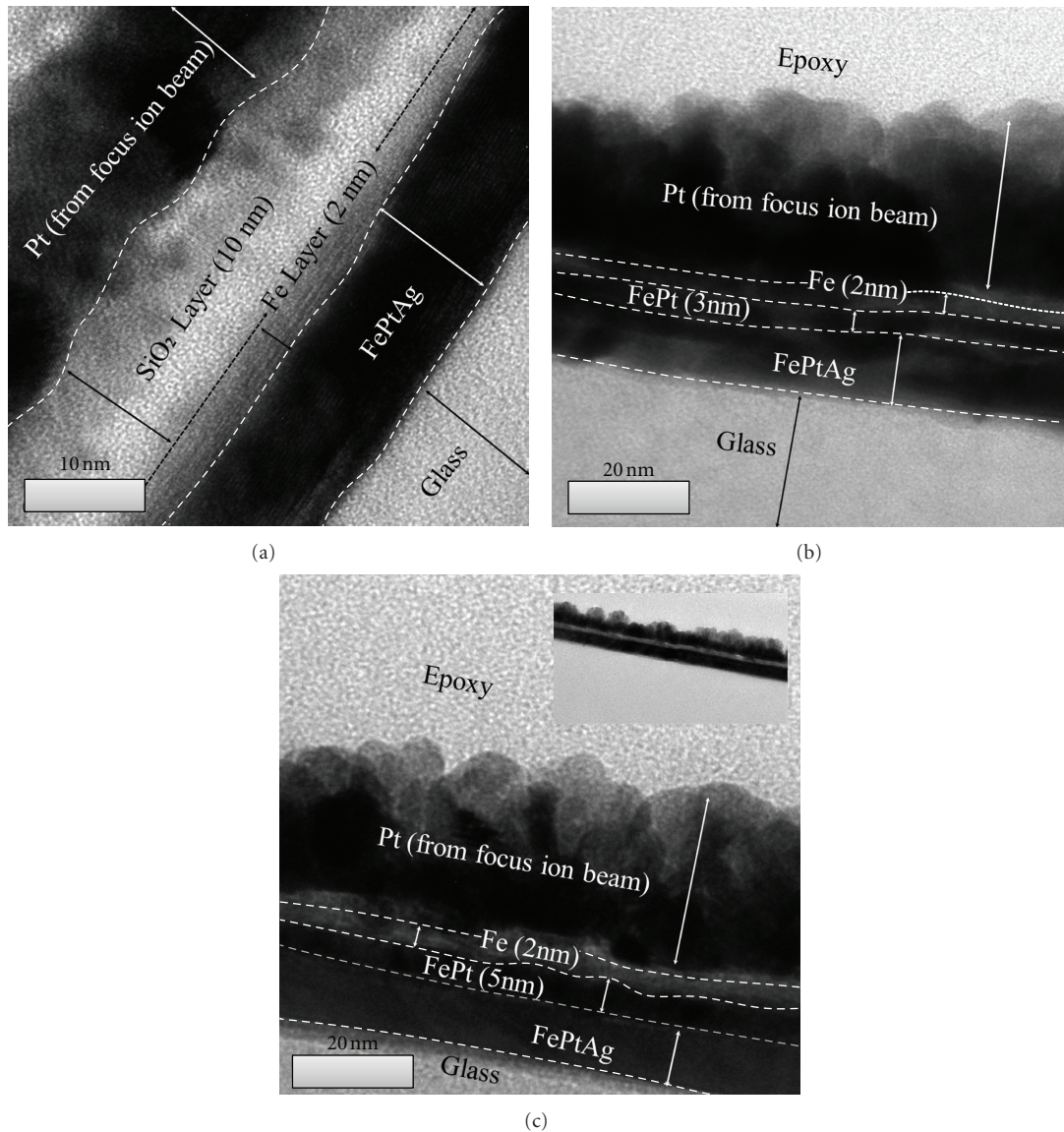


FIGURE 3: Cross-section TEM images of (a) Fe/FePtAg bilayer, (b) Fe/FePt(3 nm)/FePtAg trilayer, and (c) Fe/FePt(5 nm)/FePtAg trilayer.

From morphology, the reversed domain wall may originate from the rough interface between soft Fe/FePt. Based on the different magnetocrystalline anisotropy in Fe, FePt, and FePtAg individual layer, the magnetization was reversed stepwise from soft- to hard-magnetic layer. The coercivity was influenced more in Fe/FePt thickness and less in interface morphology.

Figure 4 show the in-plane and out-of-plane magnetic hysteresis loops of FePt/Fe/FePtAg films measured at room temperature. The in-plane and out-of-plane magnetization of glass substrate was linear with negative slope and the diamagnetic effect in FePt/glass films was computationally subtracted. In Figure 4(a), the FePt/FePtAg bilayer shows perpendicular magnetization and the out-of-plane  $H_c$  is 10.5 kOe. The disordered FePt layer with thickness of 2 nm contributed both to magnetization, in-plane and out-of-plane coercivity in FePt/FePtAg bilayer. The amount of soft-magnetic phase (FePt/Fe) increased with Fe layer thickness.

The in-plane and out-of-plane coercivities decreased with amount of soft magnetic phase (FePt/Fe) or Fe layer thickness. In Figure 4(b), the Fe layer with thickness of 0.5 nm was inserted and the magnetic properties were similar to Figure 4(a). Figure 4(c) shows magnetic hysteresis loops of FePt/Fe(1 nm)/FePtAg film. For a soft magnetic Fe layer with 1 nm thickness, the out-of-plane  $H_c$  is 11.1 kOe and in-plane  $H_c$  is 3.2 kOe. The in-plane hysteresis loop is near linear and the out-of-plane hysteresis shows high perpendicular magnetization but not better than coupling of Fe/FePt bilayer in previous work [15]. The FePt/Fe/FePtAg trilayer was coupled with rigid magnetization in remanence ( $M_r$ ). The remanence ratio measured at 2T is 0.72 high enough but relatively smaller than 0.98 presented in previous work on bilayer [15].

In Figures 4(d)–4(f), the FePt/Fe(2, 3, 5 nm)/FePtAg film maintains perpendicular magnetization but in-plane hysteresis also appears. The slight shoulders were measured

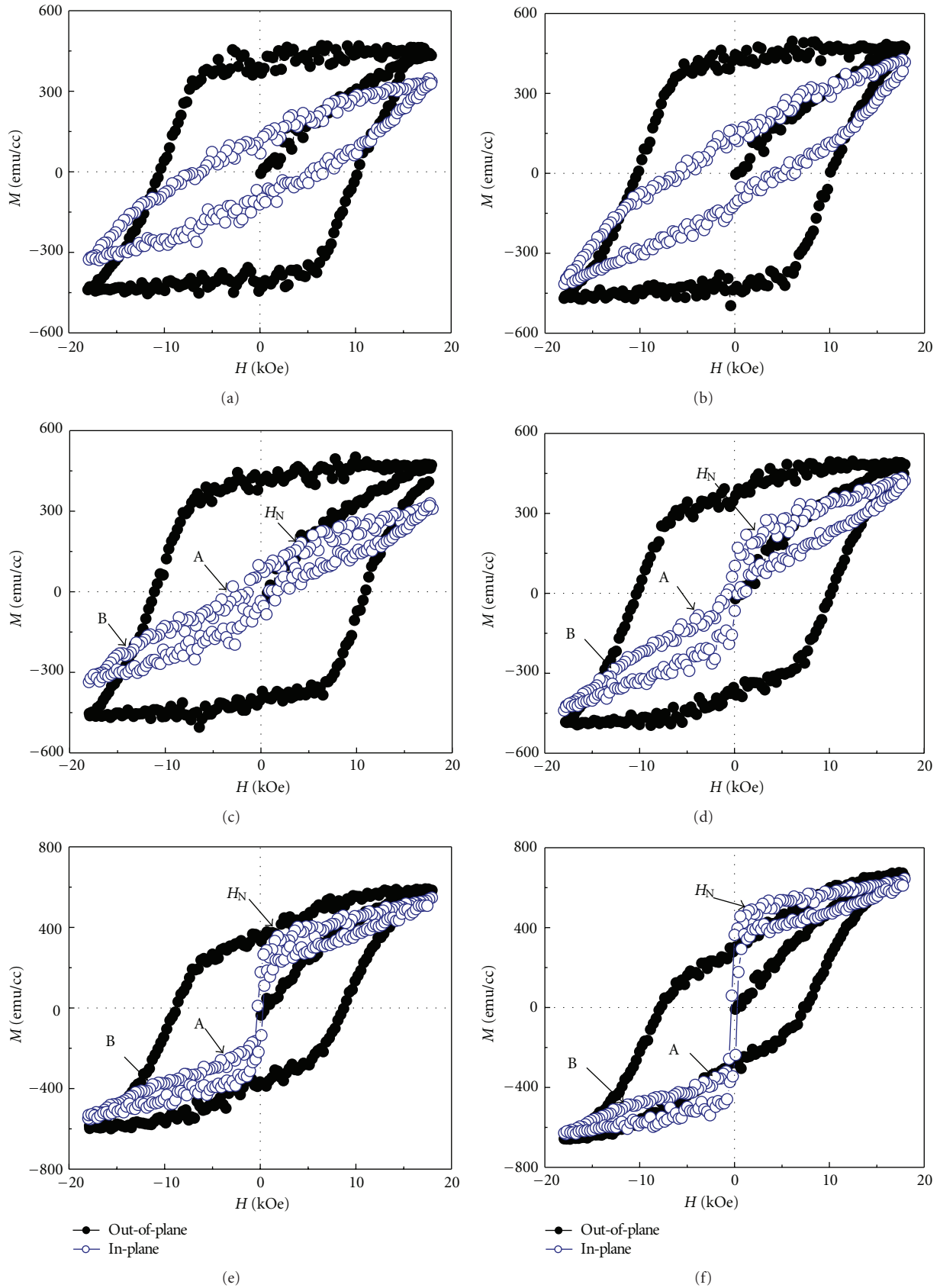


FIGURE 4: In-plane and out-of-plane magnetic hysteresis loops of (a) FePt/FePtAg film, FePt/Fe( $t$ )/FePtAg film, (b)  $t = 0.5$  nm, (c)  $t = 1$  nm, (d)  $t = 2$  nm, (e)  $t = 3$  nm, (f)  $t = 5$  nm.

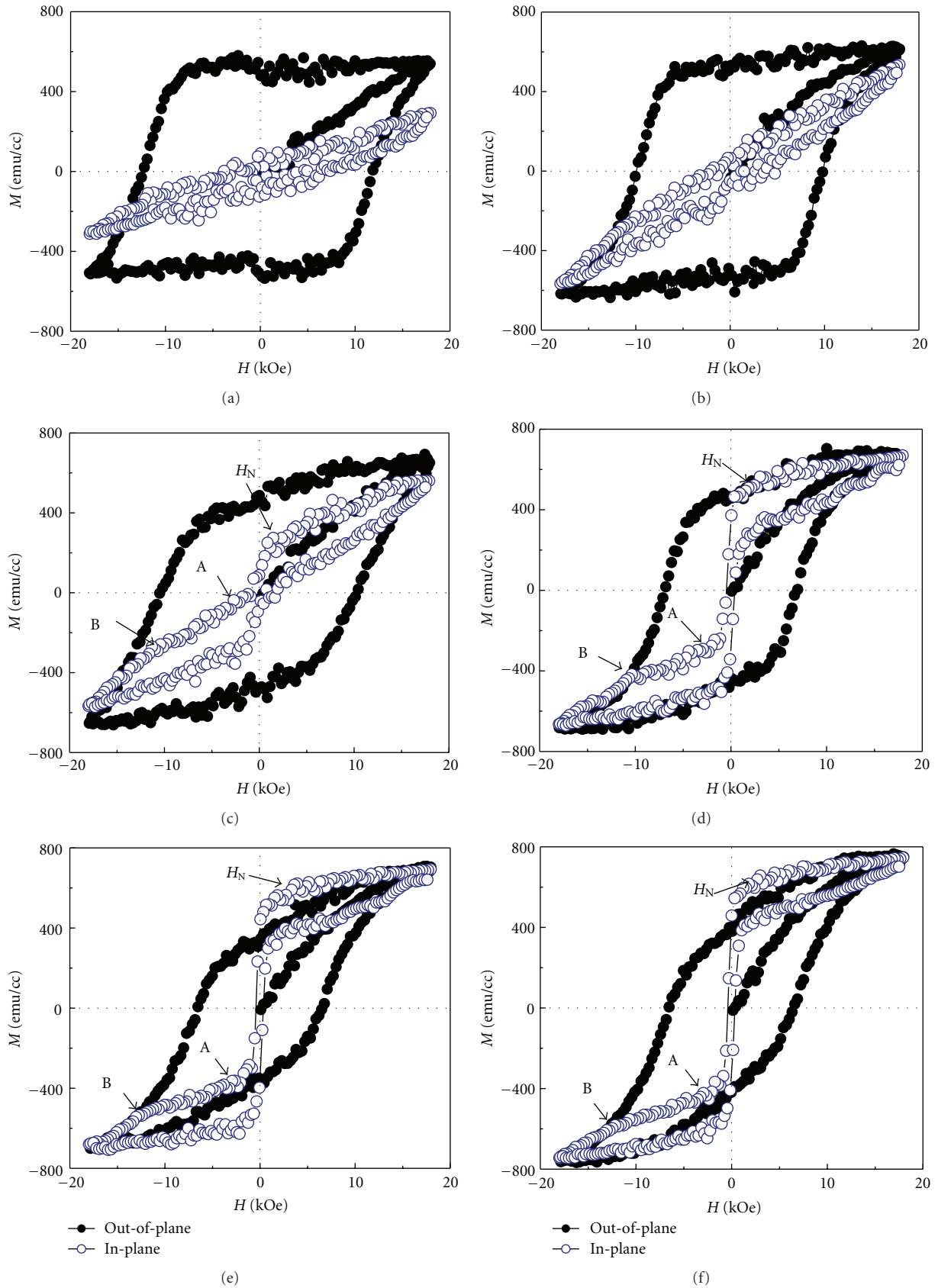


FIGURE 5: In-plane and out-of-plane magnetic hysteresis loops of (a) FePtAg film, (b) Fe(2 nm)/FePtAg film, and Fe/FePt( $t$ )/(FePtAg) trilayer, (c)  $t = 1$  nm, (d)  $t = 3$  nm, (e)  $t = 5$  nm, (f)  $t = 7$  nm.

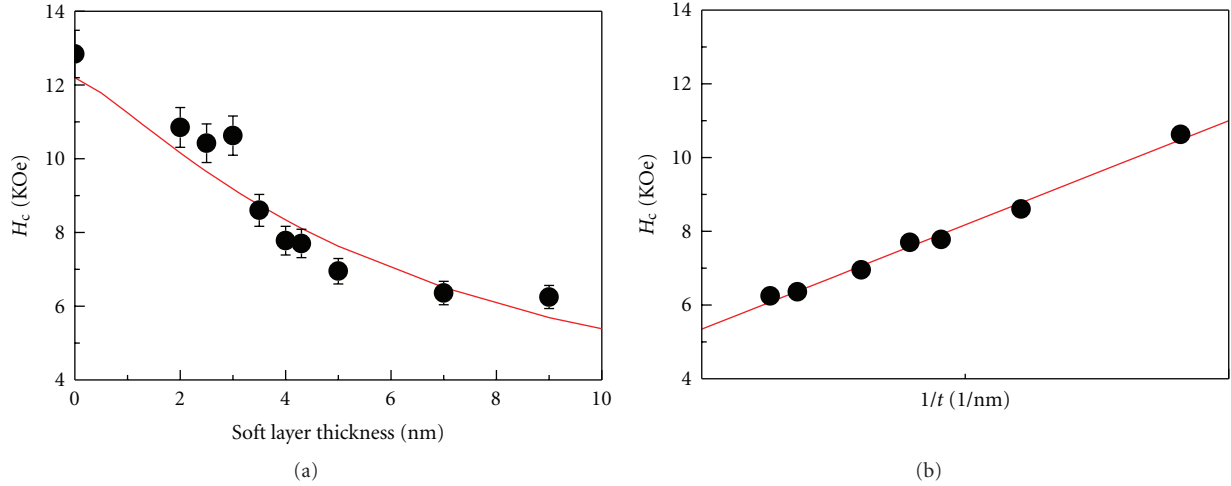


FIGURE 6: The out-of-plane  $H_c$ , as a function of (a) Fe/FePt thickness, (b)  $1/t$  ( $t$ : thickness of disordered FePt layer).

in the  $M_r$  of out-of-plane hysteresis loops. The nucleation field ( $H_N$ ), the switching fields of soft magnetic FePt/Fe layer ( $H_A$ ) and hard magnetic FePtAg layer ( $H_B$ ), and the magnetization change ( $\Delta M$ ) from  $H_N$  to  $H_A$  be marked in Figures 4(c)–4(f). The  $H_A$  and  $H_B$  mean the applied field of point A and B in Figures 4(c)–4(f). In the in-plane hysteresis loops, the magnetization reversal process seems to change to two-step reversal processes. The reversal domain wall was first nucleated at nucleation field ( $H_N$ ) in soft-magnetic FePt/Fe layer and the magnetization of FePt/Fe was reversed at  $H_A$  field. Then the domain wall was propagated from the FePt/Fe layer into the FePtAg layer. The magnetization of FePtAg layer was switched at  $H_B$  field. Moreover, the values of positive  $H_N$  and  $\Delta M$  were increased with inserted Fe layer thickness due to the amount of soft magnetic phase FePt/Fe( $t$ ). The Fe layer was used to test the maximum amount of soft phase FePt/Fe. Above the limited Fe layer thickness, the two steps magnetization reversal was appeared in in-plane loop and the shoulder or remanence declination was evidenced in out-of-plane loop.

Figure 5 shows in-plane and out-of-plane magnetic hysteresis loops of FePtAg film and Fe/FePt( $t$  nm)/(FePtAg) trilayer measured at room temperature. In Figure 5(a), the FePtAg film shows perpendicular magnetization and the out-of-plane  $H_c$  is 12.8 kOe. Figure 5(b) shows magnetic hysteresis loops of Fe(2 nm)/(FePtAg) bilayer. The out-of-plane  $H_c$  is 11.7 kOe and in-plane  $H_c$  is 0.12 kOe. Without disordered FePt layer, the in-plane loop is linear shape due to less amount of soft magnetic phase. Both in-plane and out-of-plane coercivity decreased with the thickness of disordered FePt layer. The in in-plane hysteresis loops deviated from a linear shape, indicating that the amount of soft-magnetic phase Fe/FePt( $t$ ) increased and the magnetization turns easily to the in-plane direction under an applied field. In Figures 5(c)–5(f), the interface coupling was changed to exchange-spring like behavior in the in-plane hysteresis loops. The magnetization reversal process was changed from a single switching field to two-step reversal processes. The reversed domain wall appeared in positive nucleation

field ( $H_N$ ) and the magnetization of soft Fe/FePt layer was switched at  $H_A$  field. The varied magnetization in-between  $H_N$  and  $H_A$  increased with the thickness disordered FePt. Finally, the domain walls were propagated from the Fe/FePt layer into the FePtAg layer. The magnetization of hard FePtAg layer was reversed at  $H_B$  field.

Figure 6(a) shows the soft magnetic layer (Fe/(disordered FePt)) thickness effect on the out-of-plane coercivity field of Fe/FePt/FePtAg composite films. The coercivity is reduced from 12.8 kOe to 6.5 kOe for FePtAg film and Fe/FePt(7 nm)/FePtAg composite film, respectively. The coercivity field is reduced drastically by a factor of 2 when the total thickness of Fe(2 nm)/FePt(7 nm) bilayer reaches 9 nm. This behavior is a typical two-phase system in which the soft layer thickness exceeds the Bloch wall domain wall width of hard phase [3, 9]. According to the analytical result with modified coefficients,  $H_c(\text{Fe/FePt}) = [10.5/(t_{\text{soft}}^{1.27} + 8.6) + 0.17]$ , the measured coercivities were fitted approximately by a  $1/t_{\text{soft}}^{1.27}$  relation [6, 7]. The measured coercivities were fitted by a  $1/d_{\text{soft}}^{1.27}$  relation. In Figure 6(b), the out-of-plane coercivity of Fe/FePt/FePtAg film is plotted against  $(1/t_{\text{FePt}})$ . The linear relationship is optimally obtained in  $H_c$  versus  $(1/t_{\text{FePt}})$  curve which was due to pinning at stepwise interface created by disordered FePt layer. The slope of line is given by 4.34. The value of the saturation magnetization ( $M_s$ ) and the exchange stiffness constant ( $A$ ) were assumed to be 1600 emu/cm<sup>3</sup> and 10<sup>-6</sup> erg/cm<sup>3</sup>. The maximum hard phase magnetocrystalline anisotropy energy ( $K_u$ ) is  $2.7 \times 10^6$  erg/cm<sup>3</sup> that derived from slope in Figure 6(b) with equation  $(AK)^{1/2}/(2M_s)$  [4, 9]. Nucleation controlled magnetization reversal is expected in  $1/t_s^2$  law and the magnetization reversal of Fe/FePt/FePtAg film is suppose to follow  $1/t_{\text{FePt}}$  law evidenced in Figure 6.

The results obtained previously by Kronmüller and Goll [8] for the thickness dependence of the nucleation fields are  $1/d$  and  $1/d^2$ . Fullerton et al. [12] clearly show that the coercivity field decreased strongly by a factor of 3 or 4 for soft-magnetic layer thickness up to 4 nm. Experimental results of the thickness dependence of the coercivity field of

composite films have been determined by Goll and Breitling [6, 7] for the ledge-type Fe/FePt system indicating a  $d^{-1.38}$  law for the thickness dependence.

#### 4. Conclusions

In conclusion, FePt/Fe/FePtAg and Fe/FePt/FePtAg films with perpendicular magnetization were prepared on glass substrate. The Fe interlayer thickness increased the amount of soft magnetic phase in (disordered FePt)/Fe/(L1<sub>0</sub> FePt-Ag) film. When the thickness of Fe layer is kept under 1 nm, the perpendicular anisotropy was maintained. In Fe/FePt/FePtAg trilayer, the disordered FePt layer was inserted as pinning layer and actually reduced the coupling between Fe and FePtAg. The coercivity field was modulated and found inversely proportional to the thickness of FePt layer. The in-plane magnetization reversal process of exchange spring like Fe/FePt/FePtAg film was interpreted by domain wall-assisted depinning and motion around the hard/soft interface. Finally, the inserted disordered FePt or Fe layer only increased the amount of soft magnetic phase and acted as an attenuating mechanism of the perpendicular magnetization of bilayer revealing thickness-dependent variations of magnetic properties.

#### Acknowledgments

The authors would like to thank the NSC for financial support under Grant no. NSC 100-2221-E-005-044-MY2. They also thank Dr. Y. H. Pai and the Center of Nanoscience and Nanotechnology in NCHU for the TEM investigation.

#### References

- [1] R. H. Victora and X. Shen, "Composite media for perpendicular magnetic recording," *IEEE Transactions on Magnetics*, vol. 41, no. 2, pp. 537–542, 2005.
- [2] J. P. Wang, W. K. Shen, J. M. Bai, R. H. Victora, J. H. Judy, and W. L. Song, "Composite media (dynamic tilted media) for magnetic recording," *Applied Physics Letters*, vol. 86, Article ID 142504, 3 pages, 2005.
- [3] A. Y. Dobin and H. J. Richter, "Domain wall assisted magnetic recording," *Applied Physics Letters*, vol. 89, no. 6, Article ID 062512, 2006.
- [4] D. Suess, T. Schrefl, S. Fähler et al., "Exchange spring media for perpendicular recording," *Applied Physics Letters*, vol. 87, no. 1, Article ID 012504, 3 pages, 2005.
- [5] D. Weller, A. Moser, L. Folks et al., "High  $k_u$  materials approach to 100 gbits/in<sup>2</sup>," *IEEE Transactions on Magnetics*, vol. 36, no. 1, pp. 10–15, 2000.
- [6] D. Goll, A. Breitling, L. Gu, P. A. Van Aken, and W. Sigle, "Experimental realization of graded L1<sub>0</sub>-FePt/Fe composite media with perpendicular magnetization," *Journal of Applied Physics*, vol. 104, no. 8, Article ID 083903, 2008.
- [7] D. Goll and R. Breitling, "Coercivity of ledge-type L1<sub>0</sub>-FePt/Fe nanocomposites with perpendicular magnetization," *Applied Physics Letters*, vol. 94, Article ID 052502, 3 pages, 2009.
- [8] H. Kronmüller and D. Goll, "Pinning of domain walls in composite particles," *Physica B*, vol. 403, no. 2-3, pp. 237–241, 2008.
- [9] D. Suess, "Multilayer exchange spring media for magnetic recording," *Applied Physics Letters*, vol. 89, no. 18, Article ID 113105, 2006.
- [10] A. Goncharov, T. Schrefl, G. Hrkac et al., "Recording simulations on graded media for area densities of up to 1 Tbit/in<sup>2</sup>," *Applied Physics Letters*, vol. 91, no. 22, Article ID 222502, 2007.
- [11] R. Skomski, T. A. George, and D. J. Sellmyer, "Nucleation and wall motion in graded media," *Journal of Applied Physics*, vol. 103, no. 7, Article ID 07F531, 2008.
- [12] E. E. Fullerton, J. S. Jiang, M. Grimsditch, C. H. Sowers, and S. D. Bader, "Exchange-spring behavior in epitaxial hard/soft magnetic bilayers," *Physical Review B*, vol. 58, no. 18, pp. 12193–12200, 1998.
- [13] J. P. Wang, W. Shen, and S. Y. Hong, "Fabrication and characterization of exchange coupled composite media," *IEEE Transactions on Magnetics*, vol. 43, no. 2, pp. 682–686, 2007.
- [14] F. Casoli, F. Albertini, L. Nasi et al., "Strong coercivity reduction in perpendicular FePt/Fe bilayers due to hard/soft coupling," *Applied Physics Letters*, vol. 92, no. 14, Article ID 142506, 2008.
- [15] J. L. Tsai, H. T. Tzeng, and G. B. Lin, "Magnetization reversal process in Fe/FePt films," *Applied Physics Letters*, vol. 96, Article ID 032505, 3 pages, 2010.
- [16] J. L. Tsai, H. T. Tzeng, and B. F. Liu, "Magnetic properties and microstructure of graded Fe/FePt films," *Journal of Applied Physics*, vol. 107, no. 11, Article ID 113923, 2010.
- [17] J. L. Tsai, H. W. Tai, J. C. Huang, C. S. Lin, and L. H. Chen, "Magnetic properties and microstructure of exchange coupled Fe/(FePt-Ag<sub>2</sub>Se) particulate films," *IEEE Transactions on Magnetics*, vol. 47, no. 10, pp. 3625–3628, 2011.
- [18] J. L. Tsai, J. C. Huang, and H. W. Tai, "Magnetic properties and microstructure of perpendicular FePt(B-Ag) granular films," *Journal of Applied Physics*, vol. 111, Article ID 07A709, 3 pages, 2012.
- [19] L. Zhang, Y. K. Takahashi, A. Perumal, and K. Hono, "L1<sub>0</sub>-ordered high coercivity (FePt)AgC granular thin films for perpendicular recording," *Journal of Magnetism and Magnetic Materials*, vol. 322, no. 18, pp. 2658–2664, 2010.

## Review Article

# Positive Contrast Imaging of SPIO Nanoparticles

**Chenghong Lin, Shuhui Cai, and Jianghua Feng**

*Department of Electronic Science and Fujian Provincial Key Laboratory of Plasma and Magnetic Resonance, Xiamen University, Xiamen 361005, China*

Correspondence should be addressed to Jianghua Feng, [jianghua.feng@xmu.edu.cn](mailto:jianghua.feng@xmu.edu.cn)

Received 14 December 2011; Revised 19 January 2012; Accepted 27 February 2012

Academic Editor: Carlos Martinez-Boubeta

Copyright © 2012 Chenghong Lin et al. This is an open access article distributed under the Creative Commons Attribution License, which permits unrestricted use, distribution, and reproduction in any medium, provided the original work is properly cited.

It is advantageous to achieve positive contrast images instead of negative contrast images in superparamagnetic iron-oxide (SPIO) nanoparticles-based MR imaging in order to distinguish the signal surrounding SPIO nanoparticles from the dark signal due to local field inhomogeneity and the artifacts due to tissue interface and background noise, eliminate the inherent defects in the traditional MRI such as partial-volume effects and large void volume for reliable visualization, and increase contrast-to-noise ratio. Many methods generating positive signal with SPIO nanoparticles have been developed in the last decade. This paper provides an overview of current visualization methods and states their advantages and disadvantages. In practice, these techniques have been widely applied to cell labeling and disease diagnosis and monitoring. However, there is still a need for an ideal method to achieve both accuracy and sensitivity.

## 1. Introduction

Biocompatible superparamagnetic iron-oxide (SPIO) nanoparticles have been becoming an important class of magnetic resonance imaging (MRI) contrast agents in clinic. The size of these particles ranges from tens to 100 nm, allowing the particles to achieve longer circulation time than other contrast agents such as gadolinium chelates *in vivo* [1]. These particles consist of iron oxide cores, which are coated with dextran [2] or siloxanes [3] encapsulated by a polymer [4] such as polyethylene glycol (PEG) [5] and further modified to facilitate internalization. Due to their low toxicity and high relaxivity (i.e., lower concentration) in medical practice, they display favorable nanosize-dependent properties beyond gadolinium chelates for MRI diagnosis. However, in the practical use, magnetic heterogeneity is inevitable in the region of interest (ROI) around SPIO nanoparticles due to their superparamagnetic property. Such local field inhomogeneity shortens both  $T_2^*$  and apparent  $T_2$  relaxation times since spins can relax through different paths, thus giving dark signal in MR images. Meantime, many other factors such as tissue interfaces and background noise can also result in signal loss by inducing local incoherence, which confounds the detection efficiency [6]. Moreover,

these negative contrast agents suffer from partial-volume effects, and the void volume for reliable visualization must be larger than voxel size which depends critically on the resolution of the image. Therefore, it is necessary to produce SPIO-specific-positive contrast in order to distinguish the signal surrounding SPIO nanoparticles from the dark signal derived from local field inhomogeneity and reduce the artifacts due to tissue interface and background noise, eliminate the inherent defects in the traditional MRI such as partial-volume effects and large void volume for reliable visualization, and increase contrast-to-noise ratio (CNR).

## 2. Magnetic Properties of SPIO Nanoparticles in MRI

SPIO nanoparticles are sufficiently small so that their magnetizations can randomly flip in direction at room temperature. Similar to paramagnets, they can be magnetized by an external magnetic field. However, they have much larger magnetic susceptibility than paramagnets, thus once the external magnetic field disappears, the magnetism of SPIO nanoparticles will reduce to zero immediately.

Because SPIO nanoparticles are easily magnetized in a static field and tend to agglomerate, a local magnetic field will be correspondingly produced surrounding SPIO nanoparticles when SPIO nanoparticles are magnetized. The magnetic field is approximately equal to the dipole field from a magnetized sphere [7, 8]. Moreover, the range of the magnetic field patterns from a collection of SPIO nanoparticles will reduce steeply with the radius of collection. In practice, an agglomeration of SPIO nanoparticles could not be treated as a sphere, but it may be considered as summing patterns from a group of spheres [9].

For the existence of local magnetic heterogeneity, the protons surrounding SPIO nanoparticles are actually in a heterogeneous field with different precession frequency, which leads to faster dephasing. Meanwhile, there are interactions between dipoles of protons and electronic dipoles of SPIO nanoparticles. Accordingly, the  $T_2$  of protons shortens, which will induce dark signal in the area around SPIO nanoparticles in the conventional MRI.

### 3. Positive Contrast Imaging of SPIO Nanoparticles

In the conventional MRI, SPIO nanoparticles give negative signals that are often confounded by the presence of artifacts due to hemorrhage, air, and partial-volume effects. To address these issues, many attempts have been made to generate positive contrast in the last decade. However, these positive-contrast methods can be classified into three categories as perturbation of magnetic field gradient-based, proton precession frequency-based, and phase (postprocessing)-based according to the main theory (see Table 1 for details). It is necessary to have a detailed introduction and evaluation of these methods for a suitable application.

#### 3.1. Positive Contrast Based on Perturbation of Magnetic Field Gradient

**3.1.1. Gradient Echo Acquisition for Superparamagnetic Particles (GRASP).** The GRASP is a typical method for generating positive signal via the perturbation of magnetic field gradient. Originally, Seppenwoolde et al. obtained MR images in which  $Dy_2O_3$  marker acted as positive contrast agents [10]. They conserved the signal surrounding the  $Dy_2O_3$  marker and dephased the background signal with a slice gradient, and this method was named “white marker”. Mani et al. applied this “white marker” to generate positive signal in the presence of SPIO nanoparticles, which was called GRASP [11]. The GRASP sequence is a little different from the conventional gradient echo (GRE) sequence, as shown in Figure 1. It decreases the amplitude of the rephasing gradient (e.g., to 25%), which is normally 100% as slice selection gradient to compensate the slice selection area. The signal of normal circumstances will be effectively weakened due to the gradient imbalance. However, the signal near SPIO nanoparticles will be enhanced, for the gradient balance is restored by added negative local gradient induced by the dipole field of SPIO nanoparticles. The GRASP sequence

effectively highlights the regions where SPIO nanoparticles are presented and suppresses the signal of background.

The phantom experiments demonstrated the success of the GRASP sequence in generating positive contrast of SPIO nanoparticles both in 1.5 and 3 T clinical MRI systems [11, 12]. Basically, the GRASP sequence can be performed on conventional MRI scanner within short acquisition time, but preliminary experiment is needed to optimize the amplitude of the rephasing gradient. The GRASP sequence is sensitive to field inhomogeneity and background noise is unavoidable. Moreover, it is more effective and sensitive at a moderate field (1.5 T) than at a higher field (3 T) due to the higher baseline  $R_2^*$  values at 3 T; therefore the field changes produced by the control cells is actually similar to that from the cells incubated with low concentration of SPIO nanoparticles at 1.5 T [11, 12]. High localization and relatively low concentration of SPIO nanoparticles may give optimal enhancement effect [13].

**3.1.2. iDQC Anisotropy Map Imaging.** In general, intermolecular double-quantum coherences (iDQCs) are sensitive to local magnetic field gradients [14, 15]. Bouchard et al. obtained three images with the coherence selection gradients oriented in three orthogonal directions ( $G_x$ ,  $G_y$ , and  $G_z$ ), and combined these images to detect the anisotropy in structured samples [14, 16]. Branca et al. applied this method to generate positive contrast of SPIO nanoparticles called iDQC anisotropy map imaging [6]. The iDQC signal of isotropic media has a spatial dependence  $(1 - 3\cos^2\theta)$ , where  $\theta$  is the angle between the direction of the coherence selection gradient and the external magnetic field  $B_0$ . When the correlation gradient is set along the magic angle ( $x + y + z$ ), the iDQC signal should be null in the combined image of  $G_x + G_y + G_z$  (or  $G_y + G_x - G_z$ ) since the image of  $G_z$  is twice as strong as the images of  $G_x$  and  $G_y$ . However, the intensity and phase of a structured sample is not zero in the combined image but reflects the local sample structure [16].

The iDQC anisotropy map imaging was proven effective in simulation, phantom, and animal experiments [6]. By using the iDQC imaging techniques, positive signal surrounding SPIO particles can be generated even in a heterogeneous magnetic field, and this technique is insensitive to susceptibility gradients present in most *in vivo* environments. Therefore it is promising to image the highly heterogeneous areas such as breast tumor and prostate tumor tissues. In addition, the iDQC imaging is feasible for differentiating the focal region (the live part of the tumor) from the background necrotic area in the tumor tissue. It shows exciting possibilities for tumor stage assessment through MRI with specially targeted SPIO nanoparticles [6]. Nevertheless, the major limitation of this method is lower signal-to-noise ratio (SNR) relative to the standard methods. In addition, this method needs a long echo time (TE) for sampling; thus it is unsuitable for tissue with very short  $T_2$ . Promisingly, iDQC imaging could be improved by incorporating new methods for sensitivity enhancement [17–20].

TABLE 1: Advantages and disadvantages of the currently used positive contrast imaging methods with SPIO nanoparticles.

	Perturbation of magnetic field gradient based methods		Proton precession frequency based methods				Phase (postprocessing) based methods		
	GRASP	iDQC	SR-SPSP	ORS	IRON	SSFP	PSM	SWI	SGM/PGM
Effective and sensitive	Fair	Low	Fair	Fair	Fair	Fair	High	High	High
Sensitivity to field inhomogeneity	Yes	No	Yes	Yes	Yes	Yes	Yes	Yes	Yes
Sensitivity to susceptibility gradients	Yes	No	Yes	Yes	Yes	Yes	Yes	Yes	Yes
Suppression of background signal	Poor	Good	Fair	Fair	Fair	Fair	Poor	Fair	Fair
Suppression of water signal	Poor	Good	Good	Good	Fair	Good	Poor	Fair	Fair
Signal-to-noise ratio	Fair	Low	High	High	High	High	Fair	Fair	High
Intrinsic drawback	Low sensitivity in high field	Require long TE	Two acquisitions required	Spurious signals from field inhomogeneity					

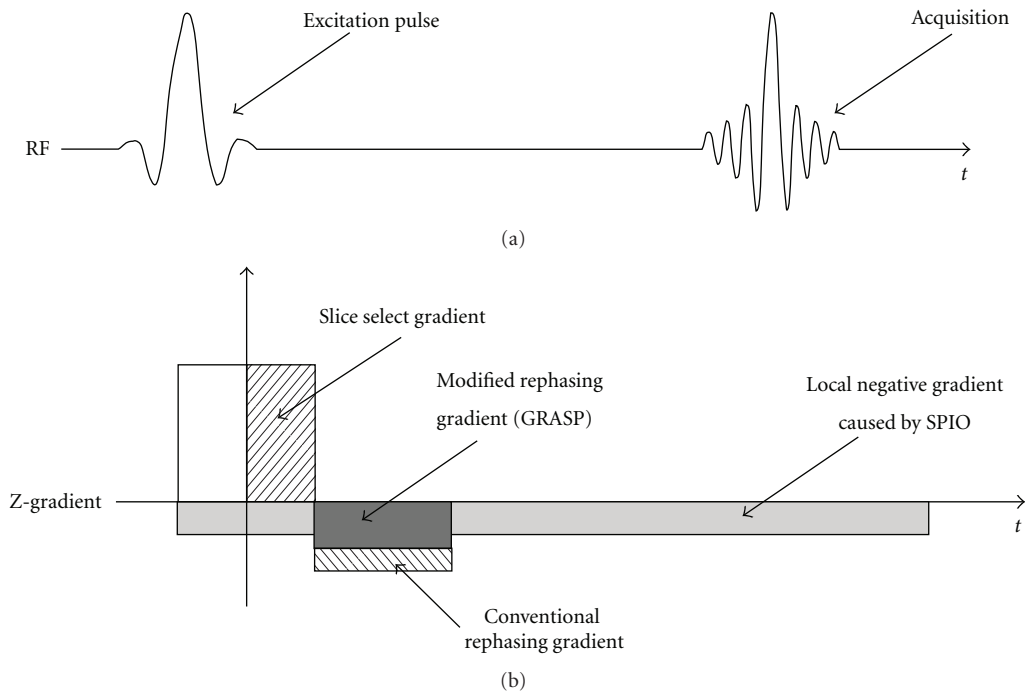


FIGURE 1: Diagram illustrating the gradients on the slice-select axis for conventional GRE imaging and GRASP sequence for bright imaging of SPIO, regenerated according to the description in [11].

### 3.2. Positive Contrast Based on Proton Precession Frequency

**3.2.1. Selective Excitation Imaging.** The SPIO nanoparticles will create large magnetization aligned with the static magnetic field, thus inducing an anisotropic resonance frequency distribution with a very well-defined spatial distribution

over a short (microns) distance scale surrounding the SPIO nanoparticles [21]. Cunningham et al. used a  $90^\circ$ – $180^\circ$  pulse pair to selectively excite and refocus a narrow band of water molecules [9]. The sequence they used also gave millionfold (120 dB) suppression of on-resonance water (Figure 2). A frequency selective was used in this sequence [22], and the

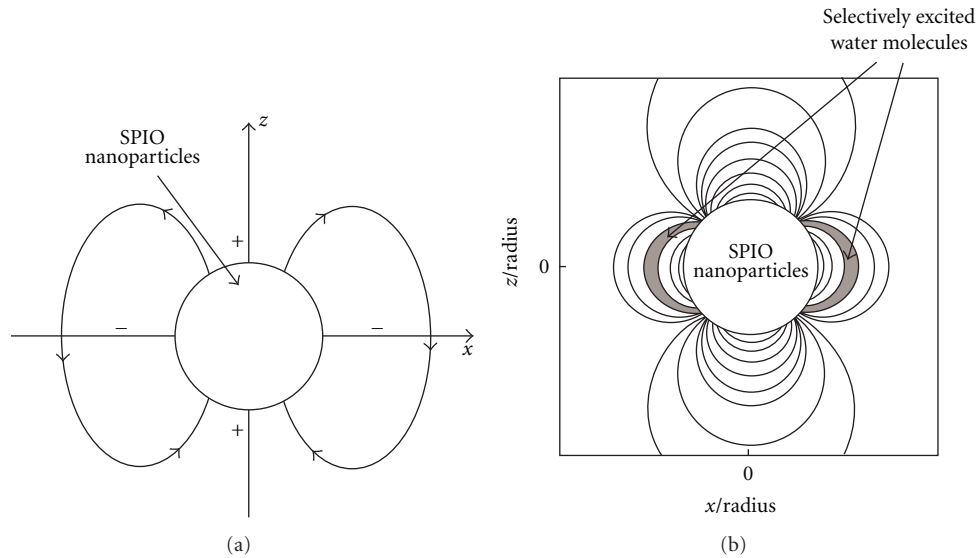


FIGURE 2: (a) Magnetic-field lines induced outside a magnetized sphere; (b) water molecules selectively excited by  $90^\circ$ – $180^\circ$  pulse pair, regenerated according to the description in [9].

$90^\circ$ – $180^\circ$  pair only excites and refocuses a thin shell of spins located at a particular frequency offset surrounding the SPIO nanoparticles [9]. Because the sources of off-resonance outside the slice of interest result in interfering signal, Balchandani et al. developed a self-refocused spatial-spectral (SR-SPSP) pulse [23], instead of  $90^\circ$ – $180^\circ$  pair, to achieve slice-selective spin-echo imaging of off-resonant spins. The spatial selectivity achieved by the SR-SPSP radio frequency (RF) pulse not only eliminates background signal from regions outside the slice of interest but also reduces the on-resonant water suppression requirement. Such pulse has been tested with phantom and *in vivo* experiments [23].

The images from phantom and *in vivo* experiments demonstrated the feasibility of selective excitation imaging on generating positive contrast [9]. Since the sequence never excites on-resonant spins and limits water suppression only in region of interest, water suppression is more efficient [9, 23]. By changing the transmit frequency and spectral offset of the pulse, it is possible to select flexibly the exciting frequency range with no need to modify the sequence or pulse and gradient waveforms in any static field. However, one limitation of this technique is that two acquisitions are required to eliminate unrefocused components of the magnetization, thus doubling the minimum scan time. In addition, the SR-SPSP pulse lasts 31.8 ms, which leads to another limitation that the minimum achievable repetition time (TR) of the whole pulse is  $\sim 43$  ms, which is  $\sim 20$  ms longer than the TR of the selective excitation imaging used by Cunningham et al. spurious signals from other off-resonant sources are still unavoidable [23]. Moreover, its applicability needs to be further investigated due to the employment of high-energy RF pulses that yield increased specific absorption rate (SAR) compared with other methods such as the GRASP sequences.

**3.2.2. Off-Resonance Saturation (ORS).** Zurkiya and Hu presented a diffusion-mediated off-resonance saturation method to generate positive contrast of ultrasmall SPIO (USPIO) nanoparticles [24]. A 6 ms Gaussian pulse was applied in each TR prior to imaging pulses to achieve off-resonance irradiation. To quantify the magnitude of the ORS effect, the ORS ratio,  $1 - (M_{\text{sat}}/M_0)$ , was calculated, where  $M_{\text{sat}}$  was the values of amplitude with off-resonance saturation, and  $M_0$  was values of amplitude without off-resonance saturation. Since the ORS ratio goes linearly with concentration below saturation concentration, the ORS approach can be used to quantify nanoparticles in an image. This method not only allows assessment of pathophysiological states but also allows reveal of the evolution of disease [25, 26].

The ORS demonstrated the favorable feasibility to generate positive signal correlated with USPIO nanoparticle concentration by agarose gel phantom experiments [24, 27]. The ORS effect is highly dependent on diffusion, suggesting that this approach may be useful for the assessment of pathological changes correlating with alteration of the diffusion [28]. However, the use of high-energy RF pulses in this method limits its application due to the increased specific absorption rate.

**3.2.3. Inversion-Recovery with On-Resonant Water Suppression (IRON).** Stuber et al. developed another technique to visualize the surroundings of SPIO nanoparticles with positive enhancement [29]. As depicted in Figure 3, it was achieved by adding a broadband dual inversion prepulse for fat and on-resonant water suppression to a conventional imaging sequence, thus the signals from fat and background were attenuated significantly. Simultaneously, the area of

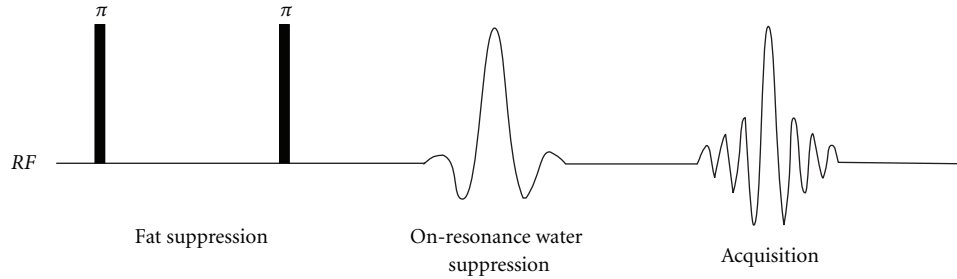


FIGURE 3: Diagram illustrating IRON sequence. Regenerated according to the description in [29].

the positive signal can be controlled by changing the pulse parameters.

IRON imaging facilitates the use of either GRE or fast spin echo (FSE) imaging protocols, for it is unnecessary to modify the imaging part of the sequence [29]. Even so, the prolonged TE may lead a weaker positive signal when IRON is combined with a GRE acquisition. Moreover, when IRON is added to a FSE acquisition, there will be a further increase in absorption rate, especially at higher magnetic field strength. The IRON imaging has been proven to be effective in cylindrical gelatin phantom and *in vivo* experiments [12, 30]. The signal of IRON is twice as the signal obtained using selective excitation method because the positive signal is simultaneously contributed from positive and negative frequency components. Additionally, the volume of positive signal shows highly correlated with the concentration of SPIO-labeled cells *in vitro* [29]. Therefore, IRON may be feasible to quantify the amount of SPIO-labeled cells. However, the volume of positive signal depends on the local concentration and spatial distribution of SPIO-labeled cells which may change quickly *in vivo*. As a result, the volume of positive signal is not exactly correlated with the number of SPIO-labeled cells *in vivo*. Moreover, as one of the sequences that use signal dephasing or off-resonance as a way of selecting SPIO signal, spurious positive signal could be unavoidable at tissue borders or air-tissue interfaces during IRON imaging, and residual background noise due to  $B_1$  inhomogeneity could also lead to local “over/under tipping” of the magnetization [29]. Furthermore, because the time of  $T_1$  recovery during the RF excitation train suffers from the dual inversion for fat suppression, the broadband dual inversion needs to be replaced with another spectrally selective prepulse for fat saturation to achieve more effective on-resonant water suppression. Finally, the threshold of detectability of SPIO-labeled cells is not clear yet for IRON imaging.

**3.2.4. Balanced Steady-State Free Precession.** Alternative dual inversion prepulse and on-resonant water suppression pulse was proposed by Dharmakumar et al. to generate positive contrast from off-resonant spins with steady-state free precession (SSFP) magnetic resonance imaging [31]. On that basis, Mascheri et al. got positive contrast imaging of USPIO-labeled macrophages with a low-tip-angle balanced

steady-state free precession (bSSFP) sequence at clinical field strength (1.5 T) and resolution ( $0.8 \times 0.8 \times 3 \text{ mm}^3$ ) [32]. Further, Çukur et al. presented an improved method, positive contrast with alternating repetition time steady-state free precession (PARTS) [33], which coupled low tip angles for generating off-resonant signal with alternating repetition times [34, 35] for water suppression. This sequence is combined with a separate acquisition where the stopband is instead centered at the fat resonance.

Both PARTS and bSSFP shows effective in phantom and *in vivo* experiments [32, 33, 35, 36]. PARTS improved background suppression, thus allowing quantitative positive contrast measurements *in vitro* [33]. However, absolute quantification *in vivo* may be impossible due to the unexpected processes such as the migration, clustering, proliferation, or death of cells. Meanwhile, PARTS is difficult to fit with higher field strength unless giving shorter TRs. Spurious signals from considerable field inhomogeneity and susceptibility boundaries are inescapable in PARTS images as other off-resonance techniques, which limit the specificity of positive contrast images with PARTS around the SPIO-labeled cells. Based on a low-tip-angle alternating repetition time (ATR) SSFP sequence, PARTS has higher SNR, lower specific absorption rate, and lower flow sensitivity than other off-resonance methods. The acquisition time of PARTS is extraordinarily short, even four to five times shorter than GRE sequences. Furthermore, PARTS can produce three-dimensional high-resolution images with positive contrast within less than one minute. The smallest number of cells detectable with the method (0.1 million *in vitro*) is not inferior to other methods [9, 29], but the detectability thresholds are yet to be determined.

### 3.3. Positive Contrast Based on Phase

**3.3.1. Phase Slope Magnitude (PSM) Imaging.** Exploiting the characteristic of phase or susceptibility is another feasible approach to generate positive signal of sites surrounding SPIO nanoparticles, which is one of postprocessing methods. The PSM image applied a high-pass filtering to the phase images [37, 38], which preserved image resolution and improved quantification sensitivity simultaneously.

The PSM imaging was proven to be effective in gel phantom and mouse experiments [37, 38]. Extraordinarily, the

images exhibit a 1- to 8-fold CNR improvement in regions containing the SPIO deposits. Moreover, it benefits from the increased sensitivity to magnetic susceptibility effects while retaining the critical anatomic backdrop by superimposing PSM images onto magnitude images. Unlike many other positive contrast imaging methods, PSM imaging does not require any modification to acquisition, and it can be combined with any imaging sequence. However, there are several inherent drawbacks for the PSM method. Firstly, the spurious signals which derived from some tissue interfaces will be unavoidable. Secondly, computational artifacts caused by rapid spatial changes in phase angle are possibly introduced into PSM images under the existence of highly relaxative SPIO nanoparticles [25]. If image resolution is too low to sample the rapid phase changes induced by highly relaxative SPIO nanoparticles in phase angle, undersampling will occur, which can potentially cause phase unwrapping problem, thus leads to an additional phase to each phase image pixel with multiple of  $2\pi$ . Finally, as a postprocessing method, the PSM images are more sensitive to motion artifacts than those mentioned above [39].

**3.3.2. Variation of Susceptibility-Weighted Imaging (SWI).** Eibofner et al. proposed a positive contrast technique combining the magnitude image with phase image of a gradient-echo dataset [40]. It is a variation of SWI technique developed by Haacke et al. [41]. A mask generated from the values of phase is multiplied by the values of amplitude, resulting in the susceptibility weighted image. By changing the properties of the phase mask, the sites surrounding SPIO nanoparticles can be highlighted against the homogeneous sites. Three different masks defined zero on phase values, Hanning mask, V-shaped mask, and step function mask were implemented in order to suppress the on-resonant spins which were defined on a certain phase shift to keep signals from protons surrounding SPIO nanoparticles.

The SWI method for SPIO nanoparticles showed good potential for positive contrast imaging on agar phantom and *ex vivo* bovine liver experiment [40]. This method can be regarded as a simple version of PSM imaging [40, 42]. Moreover, this postprocessing is insensitive toward an inaccurate shimming or inhomogeneous magnetic field because the phase filter procedure removes the low spatial frequency components. Another advantage of this technique is that the negative and the positive dipole distortions contribute positive signal simultaneously, which is accomplished by the symmetrical phase mask. However, the accuracy of this technique is limited by the inhomogeneities of the tissues around the SPIO nanoparticles and the inhomogeneity of the magnetic field, even the excitation profile of the coil. In inhomogeneous tissues such as bovine liver, due to a complete suppression of the background signal, the smallest number of SPIO-labeled cells detected significantly increases to 23,000 while concentration of 1000 cells/20 mL could be visualized in agar phantom [40]. Furthermore, this method can only be applied to the gradient echo sequence, in which lower readout bandwidth (BW) and longer TE would be better.

**3.3.3. Susceptibility Gradient Mapping (SGM) and Phase Gradient Mapping (PGM).** Dahnke et al. presented another postprocessing method called SGM [42], which was based on the fact that susceptibility-induced field gradients could be visualized after applying Fourier transform on image subsets [43]. Zhao et al. introduced an improved method PGM in which a fast Fourier transform (FFT) approach was implemented and no phase unwrapping procedure was required [44]. The PGM method generates effective positive contrast maps coming from the susceptibility gradients associated with SPIO particles. The PGM method generates positive signal with sensitivity higher than that of SGM at medium and low concentrations of SPIO, while SGM is more sensitive than PGM at longer TEs.

Both PGM and SGM show accurate estimation on the SPIO concentration from phantom dataset [12, 42, 44]. These postprocessing methods offer additional information from a  $T_2^*$ -weighted image without any extra measurement. Moreover, they can be used to discriminate hypointensities induced by susceptibility gradients from others though the provided susceptibility gradient map has a lower resolution than the original image. PGM and SGM show a great potential to detect the susceptibility induced by contrast agents or medical devices [45]. However, the unavoidable spurious signal from some tissue interfaces and the detected threshold of cells from inhomogeneous tissues are still a concern practical application.

## 4. Application of Positive Contrast Imaging with SPIO Nanoparticles

The traditional MR image could be significantly improved by positive contrast imaging of SPIO nanoparticles as contrast agents, and that has stimulated an increasing number of new techniques. Their applications have been expanded to the field of disease diagnosis and monitoring even clinical use [32], with tracking transplanted cells in various organs being the most widely investigation [46–48].

Cunningham et al. [9] and Balchandani et al. [23] achieved frequency-selective excitation positive signal of SPIO-labeled cells, in which the cells were injected into the hind limbs of a living mouse. Stuber et al. obtained three-dimensional IRON FSE images of rabbit hind limbs with 250,000 and 125,000 SPIO-labeled stem cells, respectively [29]. Both injection sites can be readily detected as areas of hyperintense signal at 3 T. Suzuki et al. compared off-resonance (OR) positive contrast with GRE acquisition of SPIO-luc-mESC (mouse embryonic stem cell transfected with luciferase reporter gene) transplanted to mice and calculated the SNR and CNR obtained from OR and GRE acquisition. Both SNR and CNR from OR acquisition are significantly higher than those from GRE acquisition [49]. Çukur et al. tracked SPIO-labeled human bone marrow stromal cells injected into mice with PARTS sequence [33]. No longer satisfied with locating the site of cells, Brisset et al. quantified cells with GRASP sequence in mouse brains [50]. They found that the measurement of cloverleaf artifact volume was significantly related to the given range

of cells. Zhao et al. used PGM and SGM images to quantify SPIO-labeled cells which were injected subcutaneously and bilaterally into the flanks of rats [44]. Besides tracking cells, positive contrast imaging with SPIO nanoparticles shows effective in detection of burn infection [51], atherosclerosis [52, 53], crush injury [13], and so on.

Although positive contrast imaging with SPIO nanoparticles solves some problems in conventional MRI, such as differentiation of SPIO nanoparticles and other noise, some problems still need further investigate, such as accuracy of detection, dependability of cells tracking with long-term, spurious signal, and elimination of susceptibility boundaries.

Besides, the research of multifunctional materials is very active in last years. Some multifunctional SPIO materials have been produced as  $T_2$ -agent in MRI, biological indicators, rhodamine B isothiocyanate,  $T_1$ -agent (dual MR contrast), and antibacterials [54–59]. These materials will bring many fresh applications of positive contrast imaging with SPIO.

## 5. Conclusions and Future Work

It is advantageous to achieve positive contrast images of SPIOs. An ideal SPIO-based positive-contrast imaging technique ought to (1) have high sensitivity and good specificity, (2) have insensitivity for field inhomogeneity and susceptibility gradients not associated with SPIOs, (3) have good suppression capability for background and on-resonant water signals, and (4) have high signal-to-noise ratio. In reality, no method will meet all these requirements as shown in Table 1 but a good positive-contrast method ideally should meet as many criteria as possible in the specific application. In practice, positive contrast imaging with SPIO nanoparticles has been successfully applied to tracking cells and disease diagnosis and monitoring. In all currently used methods, every method has its advantages, but a better method is expected to detect the SPIO nanoparticles with improved accuracy and sensitivity. It is clear that the best choice would be to take advantages of the combination of some existing methods. It is predictable that such integrate method will become increasing important and facilitate the clinical application in the future.

## Acknowledgments

This work was financially supported by the NNSF of China (11074209), Fundamental Research Funds for the Central Universities (2011121046), and Xiamen Research Platform on Systems Biology of Metabolic Disease.

## References

- [1] C. Boyer, M. R. Whittaker, V. Bulmus, J. Liu, and T. P. Davis, "The design and utility of polymer-stabilized iron oxide nanoparticles for nanomedicine applications," *NPG Asia Materials*, vol. 2, no. 1, pp. 23–30, 2010.
- [2] T. Shen, R. Weissleder, M. Papisov, A. Bogdanov, and T. J. Brady, "Monocrystalline iron oxide nanocompounds (MION): physicochemical properties," *Magnetic Resonance in Medicine*, vol. 29, no. 5, pp. 599–604, 1993.
- [3] C. W. Jung and P. Jacobs, "Physical and chemical properties of superparamagnetic iron oxide MR contrast agents: ferumoxides, ferumoxtran, ferumoxsil," *Magnetic Resonance Imaging*, vol. 13, no. 5, pp. 661–674, 1995.
- [4] K. A. Hinds, J. M. Hill, E. M. Shapiro et al., "Highly efficient endosomal labeling of progenitor and stem cells with large magnetic particles allows magnetic resonance imaging of single cells," *Blood*, vol. 102, no. 3, pp. 867–872, 2003.
- [5] M. Mahmoudi, A. Simchi, M. Imani, and U. O. Hafeli, "Superparamagnetic iron oxide nanoparticles with rigid cross-linked polyethylene glycol fumarate coating for application in imaging and drug delivery," *Journal of Physical Chemistry C*, vol. 113, no. 19, pp. 8124–8131, 2009.
- [6] R. T. Branca, Y. M. Chen, V. Mouraviev et al., "IDQC anisotropy map imaging for tumor tissue characterization *in vivo*," *Magnetic Resonance in Medicine*, vol. 61, no. 4, pp. 937–943, 2009.
- [7] D. A. Yablonskiy and E. M. Haacke, "Theory of NMR signal behavior in magnetically inhomogeneous tissues: the static dephasing regime," *Magnetic Resonance in Medicine*, vol. 32, no. 6, pp. 749–763, 1994.
- [8] J. F. Schenck, "The role of magnetic susceptibility in magnetic resonance imaging: MRI magnetic compatibility of the first and second kinds," *Medical Physics*, vol. 23, no. 6, pp. 815–850, 1996.
- [9] C. H. Cunningham, T. Arai, P. C. Yang, M. V. McConnell, J. M. Pauly, and S. M. Conolly, "Positive contrast magnetic resonance imaging of cells labeled with magnetic nanoparticles," *Magnetic Resonance in Medicine*, vol. 53, no. 5, pp. 999–1005, 2005.
- [10] J. H. Seppenwoolde, M. A. Viergever, and C. J. G. Bakker, "Passive tracking exploiting local signal conservation: the white marker phenomenon," *Magnetic Resonance in Medicine*, vol. 50, no. 4, pp. 784–790, 2003.
- [11] V. Mani, K. C. Briley-Saebo, V. V. Itskovich, D. D. Samber, and Z. A. Fayad, "Gradient echo acquisition for superparamagnetic particles with positive contrast (GRASP): sequence characterization in membrane and glass superparamagnetic iron oxide phantoms at 1.5T and 3T," *Magnetic Resonance in Medicine*, vol. 55, no. 1, pp. 126–135, 2006.
- [12] W. Liu, H. Dahnke, E. K. Jordan, T. Schaeffter, and J. A. Frank, "In vivo MRI using positive-contrast techniques in detection of cells labeled with superparamagnetic iron oxide nanoparticles," *NMR in Biomedicine*, vol. 21, no. 3, pp. 242–250, 2008.
- [13] V. Mani, K. C. Briley-Saebo, F. Hyafil, and Z. A. Fayad, "Feasibility of *in vivo* identification of endogenous ferritin with positive contrast MRI in rabbit carotid crush injury using GRASP," *Magnetic Resonance in Medicine*, vol. 56, no. 5, pp. 1096–1106, 2006.
- [14] L. S. Bouchard, R. R. Rizi, and W. S. Warren, "Magnetization structure contrast based on intermolecular multiple-quantum coherences," *Magnetic Resonance in Medicine*, vol. 48, no. 6, pp. 973–979, 2002.
- [15] Z. Chen, X. Zhu, B. Zheng, S. Cai, and J. Zhong, "Double-quantum-filtered intermolecular single-quantum coherences in nuclear magnetic resonance spectroscopy and imaging," *Chemical Physics Letters*, vol. 429, no. 4–6, pp. 611–616, 2006.
- [16] L. S. Bouchard and W. S. Warren, "Multiple-quantum vector field imaging by magnetic resonance," *Journal of Magnetic Resonance*, vol. 177, no. 1, pp. 9–21, 2005.

- [17] C. Cai, F. Gao, S. Cai, J. Zhong, and Z. Chen, "Highly efficient square wave distant dipolar field and its application for *in vivo* MRI," *Magnetic Resonance in Medicine*, vol. 64, no. 4, pp. 1128–1134, 2010.
- [18] R. T. Branca, G. Galiana, and W. S. Warren, "Enhanced non-linear magnetic resonance signals via square wave dipolar fields," *Journal of Chemical Physics*, vol. 129, no. 5, Article ID 054502, 2008.
- [19] R. T. Branca, G. Galiana, and W. S. Warren, "Signal enhancement in CRAZED experiments," *Journal of Magnetic Resonance*, vol. 187, no. 1, pp. 38–43, 2007.
- [20] T. Hou, Z. Chen, D. W. Hwang, J. H. Zhong, and L. P. Hwang, "Intermolecular double-quantum coherence MR microimaging of pig tail with unique image contrast," *Magnetic Resonance Imaging*, vol. 22, no. 4, pp. 543–550, 2004.
- [21] T. Enss, S. Ahn, and W. S. Warren, "Visualizing the dipolar field in solution NMR and MR imaging: three-dimensional structure simulations," *Chemical Physics Letters*, vol. 305, no. 1-2, pp. 101–108, 1999.
- [22] A. N. Garroway, P. K. Grannell, and P. Mansfield, "Image formation in NMR by a selective irradiative process," *Journal of Physics C*, vol. 7, no. 24, article no. 006, pp. L457–L462, 1974.
- [23] P. Balchandani, M. Yamada, J. Pauly, P. Yang, and D. Spielman, "Self-refocused spatial-spectral pulse for positive contrast imaging of cells labeled with SPIO nanoparticles," *Magnetic Resonance in Medicine*, vol. 62, no. 1, pp. 183–192, 2009.
- [24] O. Zurkiya and X. Hu, "Off-resonance saturation as a means of generating contrast with superparamagnetic nanoparticles," *Magnetic Resonance in Medicine*, vol. 56, no. 4, pp. 726–732, 2006.
- [25] C. Zimmer, S. C. Wright, R. T. Engelhardt et al., "Tumor cell endocytosis imaging facilitates delineation of the glioma-brain interface," *Experimental Neurology*, vol. 143, no. 1, pp. 61–69, 1997.
- [26] H. C. Roberts, T. P. L. Roberts, S. Ley, W. P. Dillon, and R. C. Brasch, "Quantitative estimation of microvascular permeability in human brain tumors: correlation of dynamic Gd-DTPA-enhanced MR imaging with histopathologic grading," *Academic Radiology*, vol. 9, no. 1, supplement, pp. S151–S155, 2002.
- [27] C. Khemtong, O. Togao, J. Ren et al., "Off-resonance saturation MRI of superparamagnetic nanoprobe: theoretical models and experimental validations," *Journal of Magnetic Resonance*, vol. 209, no. 1, pp. 53–60, 2011.
- [28] P. Krämer, X. Helluy, T. Kampf, E. Lang, and P. M. Jakob, "Flow-enhanced off-resonance saturation for remote detection of iron-based contrast agents," *Magnetic Resonance in Medicine*, vol. 63, no. 6, pp. 1708–1715, 2010.
- [29] M. Stuber, W. D. Gilson, M. Schär et al., "Positive contrast visualization of iron oxide-labeled stem cells using inversion-recovery with ON-resonant water suppression (IRON)," *Magnetic Resonance in Medicine*, vol. 58, no. 5, pp. 1072–1077, 2007.
- [30] G. Korosoglou, L. Tang, D. Kedziorek et al., "Positive contrast MR-lymphography using inversion recovery with ON-resonant water suppression (IRON)," *Journal of Magnetic Resonance Imaging*, vol. 27, no. 5, pp. 1175–1180, 2008.
- [31] R. Dharmakumar, I. Koktzoglou, and D. Li, "Generating positive contrast from off-resonant spins with steady-state free precession magnetic resonance imaging: theory and proof-of-principle experiments," *Physics in Medicine and Biology*, vol. 51, no. 17, article no. 006, pp. 4201–4215, 2006.
- [32] N. Mascheri, R. Dharmakumar, Z. Zhang, T. Paunesku, G. Woloschak, and D. Li, "Fast low-angle positive contrast steady-state free precession imaging of USPIO-labeled macrophages: theory and *in vitro* experiment," *Magnetic Resonance Imaging*, vol. 27, no. 7, pp. 961–969, 2009.
- [33] T. Çukur, M. Yamada, W. R. Overall, P. Yang, and D. G. Nishimura, "Positive contrast with alternating repetition time SSFP (PARTS): a fast imaging technique for SPIO-labeled cells," *Magnetic Resonance in Medicine*, vol. 63, no. 2, pp. 427–437, 2010.
- [34] J. Leupold, J. Hennig, and K. Scheffler, "Alternating repetition time balanced steady state free precession," *Magnetic Resonance in Medicine*, vol. 55, no. 3, pp. 557–565, 2006.
- [35] K. S. Nayak, H. L. Lee, B. A. Hargreaves, and B. S. Hu, "Wideband SSFP: alternating repetition time balanced steady state free precession with increased band spacing," *Magnetic Resonance in Medicine*, vol. 58, no. 5, pp. 931–938, 2007.
- [36] S. Patil, D. Jiráč, F. Saudek, M. Hájek, and K. Scheffler, "Positive contrast visualization of SPIO-labeled pancreatic islets using echo-dephased steady-state free precession," *European Radiology*, vol. 21, no. 1, pp. 214–220, 2011.
- [37] P. H. Mills, Y. J. L. Wu, C. Ho, and E. T. Ahrens, "Sensitive and automated detection of iron-oxide-labeled cells using phase image cross-correlation analysis," *Magnetic Resonance Imaging*, vol. 26, no. 5, pp. 618–628, 2008.
- [38] P. H. Mills and E. T. Ahrens, "Enhanced positive-contrast visualization of paramagnetic contrast agents using phase images," *Magnetic Resonance in Medicine*, vol. 62, no. 5, pp. 1349–1355, 2009.
- [39] A. Rauscher, M. Barth, J. R. Reichenbach, R. Stollberger, and E. Moser, "Automated unwrapping of MR phase images applied to BOLD MR-venography at 3 Tesla," *Journal of Magnetic Resonance Imaging*, vol. 18, no. 2, pp. 175–180, 2003.
- [40] F. Eibofner, G. Steidle, R. Kehlbach, R. Bantleon, and F. Schick, "Positive contrast imaging of iron oxide nanoparticles with susceptibility-weighted imaging," *Magnetic Resonance in Medicine*, vol. 64, no. 4, pp. 1027–1038, 2010.
- [41] E. M. Haacke, Y. Xu, Y. C. N. Cheng, and J. R. Reichenbach, "Susceptibility weighted imaging (SWI)," *Magnetic Resonance in Medicine*, vol. 52, no. 3, pp. 612–618, 2004.
- [42] H. Dahnke, W. Liu, D. Herzka, J. A. Frank, and T. Schaeffter, "Susceptibility gradient mapping (SGM): a new postprocessing method for positive contrast generation applied to superparamagnetic iron oxide particle (SPIO)-labeled cells," *Magnetic Resonance in Medicine*, vol. 60, no. 3, pp. 595–603, 2008.
- [43] J. R. Reichenbach, R. Venkatesan, D. A. Yablonskiy, M. R. Thompson, S. Lai, and E. M. Haacke, "Theory and application of static field inhomogeneity effects in gradient-echo imaging," *Journal of Magnetic Resonance Imaging*, vol. 7, no. 2, pp. 266–279, 1997.
- [44] Q. Zhao, J. Langley, S. Lee, and W. Liu, "Positive contrast technique for the detection and quantification of superparamagnetic iron oxide nanoparticles in MRI," *NMR in Biomedicine*, vol. 24, no. 5, pp. 464–472, 2011.
- [45] H. Zhu, K. Demachi, and M. Sekino, "Phase gradient imaging for positive contrast generation to superparamagnetic iron oxide nanoparticle-labeled targets in magnetic resonance imaging," *Magnetic Resonance Imaging*, vol. 29, no. 7, pp. 891–898, 2011.
- [46] A. A. Gilad, P. Walczak, M. T. McMahon et al., "MR tracking of transplanted cells with "positive contrast" using manganese oxide nanoparticles," *Magnetic Resonance in Medicine*, vol. 60, no. 1, pp. 1–7, 2008.

- [47] D. Li, Z. Zhang, R. Dharmakumar, N. Mascheri, Z. Fan, and S. Wu, "Comparison of superparamagnetic and ultrasmall superparamagnetic iron oxide cell labeling for tracking green fluorescent protein gene marker with negative and positive contrast magnetic resonance imaging," *Molecular Imaging*, vol. 8, no. 3, pp. 148–155, 2009.
- [48] J. Chung, K. Kee, J. K. Barral et al., "In vivo molecular MRI of cell survival and teratoma formation following embryonic stem cell transplantation into the injured murine myocardium," *Magnetic Resonance in Medicine*, vol. 66, no. 5, pp. 1347–1381, 2011.
- [49] Y. Suzuki, C. H. Cunningham, K. I. Noguchi et al., "In vivo serial evaluation of superparamagnetic iron-oxide labeled stem cells by off-resonance positive contrast," *Magnetic Resonance in Medicine*, vol. 60, no. 6, pp. 1269–1275, 2008.
- [50] J. C. Brisset, M. Sigovan, F. Chauveau et al., "Quantification of iron-labeled cells with positive contrast in mouse brains," *Molecular Imaging and Biology*, pp. 1–7, 2010.
- [51] O. C. Andronesi, D. Mintzopoulos, N. Psychogios et al., "Combined off-resonance imaging and T2 relaxation in the rotating frame for positive contrast MR imaging of infection in a murine burn model," *Journal of Magnetic Resonance Imaging*, vol. 32, no. 5, pp. 1172–1183, 2010.
- [52] G. Korosoglou, R. G. Weiss, D. A. Kedziorek et al., "Noninvasive detection of macrophage-rich atherosclerotic plaque in hyperlipidemic rabbits using "positive contrast" magnetic resonance imaging," *Journal of the American College of Cardiology*, vol. 52, no. 6, pp. 483–491, 2008.
- [53] K. C. Briley-Saebo, V. Mani, F. Hyafil, J. C. Cornily, and Z. A. Fayad, "Fractionated Feridex and positive contrast: in vivo MR imaging of atherosclerosis," *Magnetic Resonance in Medicine*, vol. 59, no. 4, pp. 721–730, 2008.
- [54] G. Zabow, S. Dodd, J. Moreland, and A. Koretsky, "Micro-engineered local field control for high-sensitivity multispectral MRI," *Nature*, vol. 453, no. 7198, pp. 1058–1063, 2008.
- [55] T. H. Kim, J. K. Kim, W. Shim, S. Y. Kim, T. J. Park, and J. Y. Jung, "Tracking of transplanted mesenchymal stem cells labeled with fluorescent magnetic nanoparticle in liver cirrhosis rat model with 3-T MRI," *Magnetic Resonance Imaging*, vol. 28, no. 7, pp. 1004–1013, 2010.
- [56] Y. Onuki, I. Jacobs, D. Artemov, and Y. Kato, "Noninvasive visualization of in vivo release and intratumoral distribution of surrogate MR contrast agent using the dual MR contrast technique," *Biomaterials*, vol. 31, no. 27, pp. 7132–7138, 2010.
- [57] Z. Wei, Z. Zhou, M. Yang et al., "Multifunctional Ag@Fe<sub>2</sub>O<sub>3</sub> yolk-shell nanoparticles for simultaneous capture, kill, and removal of pathogen," *Journal of Materials Chemistry*, vol. 21, no. 41, Article ID 16344, 2011.
- [58] H. Yang, Y. Zhuang, Y. Sun et al., "Targeted dual-contrast T<sub>1</sub> and T<sub>2</sub>-weighted magnetic resonance imaging of tumors using multifunctional gadolinium-labeled superparamagnetic iron oxide nanoparticles," *Biomaterials*, vol. 32, no. 20, pp. 4584–4593, 2011.
- [59] F. Wang, X. Chen, Z. Zhao et al., "Synthesis of magnetic, fluorescent and mesoporous core-shell-structured nanoparticles for imaging, targeting and photodynamic therapy," *Journal of Materials Chemistry*, vol. 21, no. 30, pp. 11244–11252, 2011.

## Research Article

# Simulation of Magnetophoretic Separation Processes in Dispersions of Superparamagnetic Nanoparticles in the Noncooperative Regime

Jordi S. Andreu,<sup>1,2</sup> Pablo Barbero,<sup>2</sup> Juan Camacho,<sup>2</sup> and Jordi Faraudo<sup>1</sup>

<sup>1</sup>Materials Simulation and Theory Department, Institut de Ciència de Materials de Barcelona (ICMAB-CSIC), Campus UAB, 08193 Bellaterra, Spain

<sup>2</sup>Departament de Física, Universitat Autònoma de Barcelona, Campus UAB, 08193 Bellaterra, Spain

Correspondence should be addressed to Jordi S. Andreu, jandreu@icmab.es

Received 15 December 2011; Accepted 30 January 2012

Academic Editor: Carlos Martinez-Boubeta

Copyright © 2012 Jordi S. Andreu et al. This is an open access article distributed under the Creative Commons Attribution License, which permits unrestricted use, distribution, and reproduction in any medium, provided the original work is properly cited.

Magnetic separation has gained much attention due to its implications in different fields, becoming feasible as an alternative to existent technologies at the industrial and lab scale. Substantial efforts are focused to improve the magnetic particles used in these applications. Here we show how a relatively simple and low-cost simulation strategy (tracer simulations) can be employed to predict the effect of various key factors in magnetic separation processes, namely, particle properties and magnetic separator designs. For concreteness, we consider here specific problems in magnetic separation. The first one is the effect of different profiles of the magnetic field in the separation of magnetic nanoparticles, and the second one is the magnetophoresis of colloidal particles in a dispersion of magnetic nanoparticles.

## 1. Introduction

The manipulation of magnetic particles by the use of inhomogeneous magnetic fields has emerged as a topic of great interest in a wide range of research and technological areas [1]: from wastewater treatments [2, 3] or pollutants removal [4] to biomedical applications like protein isolation, drug delivery, magnetic hyperthermia, or magnetic particle imaging [5, 6]. The use of inhomogeneous magnetic fields to drive magnetic particles apart from solution, what is known as magnetic separation or magnetophoresis, has provided new techniques capable to improve standard technologies, especially in biotechnological applications [7].

The idea behind magnetic separation is to take advantage of the distinctive magnetic response of the particles in solution to remove them from complex mixtures by the use of applied inhomogeneous magnetic fields [8]. In a wide range of applications, magnetic particles are typically functionalized with proper chemical groups, designed to bind to specific nonmagnetic components, thus enabling the separation

of nonmagnetic materials by combining the use of magnetic particles and magnetic fields. This combination has many advantages over traditional fixed-bed separation methods, such as activated carbon adsorption for organics and affinity chromatography for proteins. In particular, magnetic nanoparticles offer large exposed surface areas without the use of porous materials, which are often plagued by high mass transfer resistances [9]. Therefore, it is not surprising that magnetic separation has been presented as an alternative to typical centrifugation and filtration steps in industrial processes as well as in lab applications. In the biomedical field, magnetic separation may help to overcome some disadvantages of standard column liquid chromatography in the separation of proteins and peptides, and it serves as a basis of various immunoassays systems. Moreover, magnetic separation can also be used to concentrate large volumes of diluted protein solutions in a very gentle way [7].

The basic ingredients in any magnetic separation application are two: the selection of appropriate magnetic particles

and the design of the magnetic separator. Typically, the particles employed in these applications are superparamagnetic particles. One has to bear in mind that superparamagnetism emerges as a quantum effect in some ferromagnetic and ferromagnetic materials, below the single domain size. This implies that this phenomenon is limited to nanocrystals of size below a certain critical size which depends on the material [10]. Since the magnetic force is proportional to the particle magnetization, superparamagnetic nanoparticles with large magnetic response are desired. A standard way to enhance the magnetic response of the carrier particles is to synthesize larger particles by embedding superparamagnetic nanocrystals in a matrix of nonmagnetic material (such as polystyrene [11] or silica [12]), thus preserving the superparamagnetic behavior of these crystals and guaranteeing the stability and biocompatibility of the solutions. In this manner, particles with larger magnetizations are obtained, increasing the magnetic response under an external field. Nevertheless, one has to balance this increase on the magnetic response (which could enhance the separation process) with the reduction on the active surface area of the particles, implying a reduction on the capture and retention of target entities. Actually, a wide range of different particles are already commercially available (from nanoparticles to larger superparamagnetic colloids) combining different magnetic response, size and decorated surfaces designed to target specific components.

A second issue about the separation process is the application of a specific magnetic field over the target sample, inducing a magnetic moment in the carrier particles. This magnetic field has not only to induce a magnetic moment but also to generate a magnetic gradient (which produces a magnetic force on the particle) in order to drive carrier particles apart from solution. Then, the conditions to be fulfilled by the magnetic field source are two: it has to induce large magnetizations but also a gradient in the intensity of the magnetic field. The simplest option to induce magnetophoresis in a lab tube or vial is by the application of a simple bar magnet, but this option is highly inefficient, since typically only those particles near the magnet really experience enough magnetic force to move. However, it is possible to obtain efficient magnetic separators by combining permanent magnets in convenient arrangements in order to generate magnetic fields suitable for magnetic separation. Among the possible arrangements of the magnets, we will discuss here the advantages and drawbacks of two possible cylindrical tube geometries, which have been called open and closed arrangements. Essentially, the closed structure consists of an arrangement of magnets around the tube containing the suspension, which generates a uniform magnetic gradient pointing towards the wall of the tube (see, e.g., [13–17]). In this case, one obtains uniform magnetophoretic conditions, a desirable feature in order to characterize, model, and scale-up the magnetophoresis process. The open-type magnetic separator [18, 19] is similar to the previous one, but in this case the design contains an aperture, that is, there is a region near the tube walls which does not contain magnets. These open structures are designed to operate directly to test tube racks and helps on the visual monitoring of the process. In a preliminary communication [20], we noted that these

two different separator designs induce substantial differences in the dynamics of the magnetic separation process.

Here, we propose a simple simulation methodology which allows to model the magnetophoretic separation of nanoparticles inside different designs of magnetic separators. As a first application, the methodology proposed here will be employed to compare the performance of open and closed separator designs. In a second one, we will study the magnetophoretic separation process of a mixture containing particles with different sizes and magnetic responses.

## 2. Tracer Simulation of Magnetophoresis of Superparamagnetic Nanoparticles

*2.1. Basic Equations and Simulation Methodology.* Let us start by describing the equations of motion of superparamagnetic nanoparticles (NPs) in a liquid dispersion under the effects of an external magnetic field. In this situation, NPs will move in the direction of the magnetic gradient (magnetophoresis). As shown experimentally and theoretically in previous works [13, 17], we have two different kinds of magnetophoretic separation processes. The first case is called cooperative magnetophoresis, and it is characterized by fast separation times (magnetophoretic velocities can be roughly estimated as of the order of a cm per minute) which depend strongly on the concentration of the sample. It is usually found for composite colloids of several hundreds of nm in diameter (made of magnetic NPs embedded in a nonmagnetic matrix) and its driving force is the reversible formation of chains of colloids under the magnetic field [13]. The second case corresponds to noncooperative magnetophoresis, and it is typically found for dispersions of small NPs [17]. In this case, magnetophoretic velocities are much lower, and they do not depend on particle concentration; instead, they depend strongly on the magnetic gradient and the design of the magnetic separator [17, 20]. In this case, the magnetophoretic separation process is ruled by the individual motion of the superparamagnetic NPs. In addition to experimental characterization of both situations, we have formulated a mathematical criterion which allows us to predict whether we will observe cooperative or noncooperative magnetophoresis. This criterion (see [17] for details) establishes that cooperative magnetophoresis is observed when the aggregation parameter  $N^*$  verifies  $N^* > 1$ . This parameter is given by

$$N^* = \sqrt{\phi_0 e^{\Gamma-1}}, \quad (1)$$

where  $\phi_0$  is the initial volume fraction of particles in suspension, and  $\Gamma$  is the magnetic coupling parameter characterizing the strength of magnetic interaction of particles at contact as compared with thermal agitation and defined as

$$\Gamma = \frac{\mu_0 m_s^2}{2\pi d^3 k_B T}. \quad (2)$$

In (2)  $\mu_0$  is the permeability of the free space,  $m_s$  is the magnetic moment of a particle at saturation,  $d$  is its diameter, and  $T$  the absolute temperature.

In this work, we will consider only the noncooperative case characterized by  $N^* < 1$ , which is typically the case for

dispersions of NPs. For example, a 10 g/L dispersion of superparamagnetic  $\gamma$ -Fe<sub>2</sub>O<sub>3</sub> NPs (diameter 12 nm) employed in [17] provide  $\Gamma = 2.5$  and  $N^* = 0.1$ .

Under these conditions, we thus need to consider only the individual motion of NPs in the magnetic gradient to obtain the magnetophoretic behavior, ignoring the interaction between NPs. The magnetophoretic velocity of a NP immersed in a fluid with viscosity  $\eta$  submitted to a magnetic gradient can be obtained as follows. The magnetic force acting on a magnetic particle can be written as

$$\vec{F}_{\text{mag}} = \mu_0 V \rho_p (\vec{M}(H) \cdot \nabla) \vec{H}, \quad (3)$$

where  $\vec{H}$  is the magnetic field,  $V$  is the volume of the particle,  $\rho_p$  is its density, and  $\vec{M}$  is the magnetization of the particle per unit mass. Notice here that this expression assumes that the magnetization of the particle is uniform [8] so that the magnetic moment is given by

$$m(H) = V \rho_p M(H). \quad (4)$$

Nevertheless, in the case of a superparamagnetic particle, its total magnetic moment aligns parallel to the applied magnetic field and (3) can be written as

$$\vec{F}_{\text{mag}} = \mu_0 V \rho_p M(H) \vec{\nabla} H, \quad (5)$$

where  $H$  is the modulus of the magnetic field. On the other hand, the viscous drag force exerted by the solvent over a single spherical particle of radius  $R$  is

$$\vec{F}_{\text{vis}} = -6\pi\eta R \vec{v}. \quad (6)$$

The magnetophoretic velocity of a particle in the steady state is obtained by balancing the magnetic force  $F_{\text{mag}}$  and the viscous drag force  $F_{\text{vis}}$  exerted by the solvent:

$$\vec{v} = \frac{2\mu_0 \rho_p M(H) R^2}{9\eta} \vec{\nabla} H. \quad (7)$$

In order to apply (7) in a real situation, one needs to know not only the profile of the applied magnetic field but also a full characterization of the magnetic response  $M(H)$  of the NPs. In our calculations, we will assume that the magnetization  $M(H)$  of a single superparamagnetic nanoparticle under an external magnetic field  $H$  is described within a good approximation by a Langevin function typical in theoretical descriptions of this superparamagnetic behavior [10, 21–23]

$$M(H) = M_s \mathcal{L}[b\mu_0 H], \quad \mathcal{L}[x] = \coth x - \frac{1}{x}, \quad (8)$$

where  $M_s$  denotes the saturation magnetic moment per unit mass, and  $b$  is related to  $M_s$  and  $R$  by (see [17, 22])

$$b = \frac{m_s}{k_B T} = \frac{4\pi R^3 M_s \rho_p}{3k_B T}. \quad (9)$$

The value of  $b^{-1}$  can be interpreted as a characteristic magnetic field required to reach saturation. Equations (7)–(9) allow one to predict the magnetophoretic motion of a

superparamagnetic NP if the spatial profile of the magnetic field of the magnetic separator is known.

In the case of a very simple geometry for the magnetic field, it has been possible [17] to obtain analytically an exact equation for the trajectory of a NP inside a magnetic separator and also obtain the kinetics of the separation process (number of particles remaining in solution as a function of time). However, for a general magnetic field geometry, finding an analytical solution is not possible. The option explored in this paper will be to perform simulations of tracer particles under known magnetic profiles. In this simulation method, each particle tracer is not intended to represent a real particle but it effectively describes the dynamics of a given particle under the external conditions imposed (tracer simulations are common in fields such as fluid mechanics, see, e.g., [24]).

The simulation technique is as follows. First of all, we need to know the geometry of the magnetic separator and the magnetic field  $H(\vec{r})$  in all points inside the magnetic separator. Then, we consider the motion of  $N_p$  tracers inside the given geometry and magnetic field. Initially ( $t = 0$ ), the positions  $\vec{r}_i(t = 0)$  ( $i = 1, \dots, N_p$ ) of these tracers are generated to be distributed uniformly inside the magnetic separator. The simulation then proceeds by assuming that each of these tracers behaves as a superparamagnetic NP. The position  $\vec{r}_i(t)$  of a tracer evolves obeying

$$\frac{d\vec{r}_i}{dt} = \vec{v}(\vec{r}_i), \quad (10)$$

where the magnetophoretic velocity  $\vec{v}(\vec{r}_i)$  is computed from (7)–(9) taking into account the local value of the magnetic field and the magnetic gradient evaluated at position  $\vec{r}_i$ . The equation of motion of the tracers ((10) supplemented with (7)–(9)) is integrated numerically in discrete time steps  $\Delta t$  by employing a Verlet [25] type integration algorithm which provides good accuracy at a reasonable cost of CPU time. All these calculations were implemented in a C code developed in house, which is available under request to the authors.

**2.2. Validation of the Simulation Methodology.** In this subsection, we will consider a magnetophoretic separation problem for which we obtained both experimental results and an analytical solution. Comparison of the results of our simulations with previously known results is a necessary step in order to ensure the validity of our simulation approach. After this validation step, we will employ our simulation method in the following subsection to explore other situations in which previous theoretical results are not available.

Here we consider the closed geometry for the magnetic separator, similar to the actual separators employed in recent experimental works [13, 15–17]. The geometry of the separator is a cylinder (radius  $L = 1.5$  cm), and it contains a magnetic field increasing from zero in the center to a maximum value at the walls, as shown in Figure 1 (see also inset in Figure 2 for a sketch of the separator). Note that the gradient of the modulus of the magnetic field is approximately uniform inside the system ( $\approx 30$  T/m). The parameters for the simulation were selected in order to match the experimental system considered in Figure 1 of [17]. In

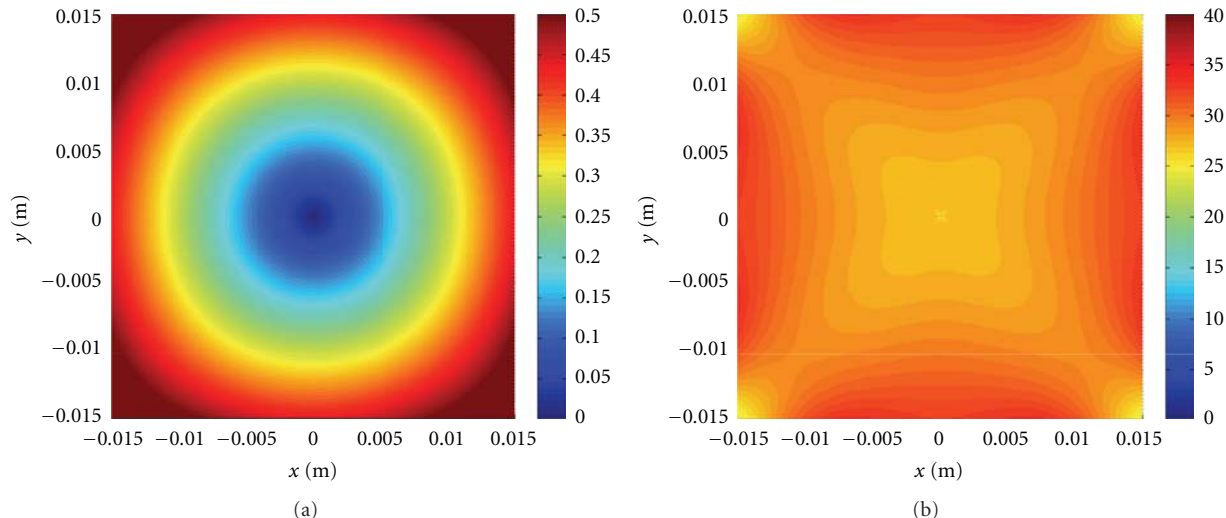


FIGURE 1: Profile of the magnitude (modulus) of the quadrupolar magnetic field in Tesla (a) and its gradient in Tesla/m (b) for the closed type magnetic separator (top view) employed in the simulations. Note that the magnitude of gradient of the field intensity corresponds to  $\approx 30$  T/m in most regions of the separator; however, inhomogeneities due to the quadrupolar nature of the field can be clearly seen.

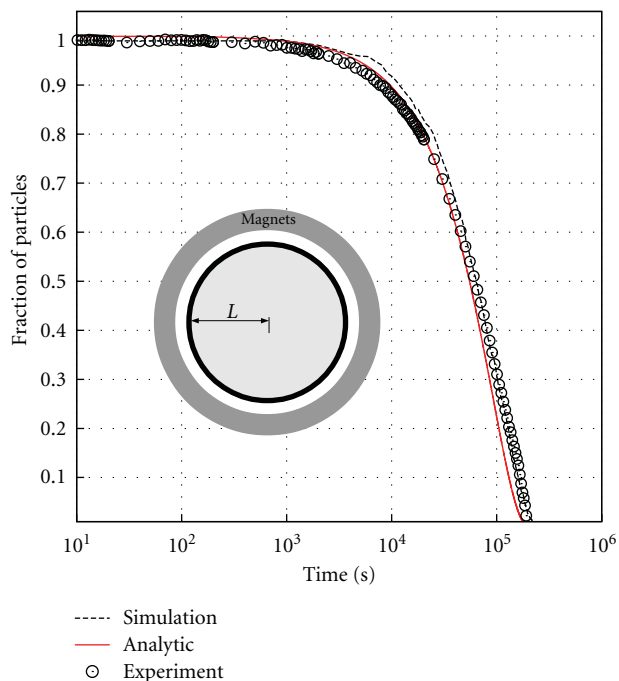


FIGURE 2: Magnetophoretic separation of superparamagnetic  $\gamma$ -Fe<sub>2</sub>O<sub>3</sub> NPs of diameter 12 nm inside a 30 T/m magnetic separator. Comparison between the simulations performed here, the analytical solution and the experimental results reported in [17] for the evolution of the fraction of particles remaining in the separator. Inset: sketch (top view) of the magnetic separator.

this experiment, a 10 g/L dispersion of superparamagnetic  $\gamma$ -Fe<sub>2</sub>O<sub>3</sub> NPs (diameter 12 nm) was placed inside the separator. The magnetization curve for these NPs was given also in [17], and it was shown that they obey (8) and (9) with  $m_s = (4/3)\pi R^3 \rho_p M_s = 3 \times 10^{-19}$  J/T and  $b = 68$  T<sup>-1</sup>. The

employed solvent was water (with viscosity  $\eta \approx 0.001$  Pa  $\cdot$  s at 298 K). Our tracer simulations were performed considering  $N_p = 10^3$  tracer particles and a time step of  $\Delta t = 10^2$  s. The simulations were performed until a simulation time of  $2 \times 10^5$  s. The calculations required only 26 min of CPU running in a single core of an AMD Opteron Magny Cours 6136 processor. During the simulation, we saved the trajectories of the tracer particles for further analysis. From these results, we estimated the concentration profile of the NPs at different times and we also computed the time evolution of the fraction of particles inside the dispersion (i.e., the number of tracers which have not reached the walls of the system divided by the total number of tracers). This last quantity is compared in Figure 2 with the experimental results obtained in [17]. We also show the results corresponding to the analytical expression developed in [17]. Our simulation results are in good agreement with these previous results, thereby validating our simulation technique.

**2.3. Comparison between Different Separator Designs.** Now, we employ our simulation methodology to compare the performance of two different designs of magnetic separators. The first design we consider here is the one considered in the previous subsection, which we will call “closed type” separator from now on. As we said previously, the main advantage of this geometry for the magnetic separator is the fact that the magnetic gradient is approximately uniform inside the system. The second design we will consider here is an “open type” separator. In this case, the geometry of the separator is the same as the closed type considered in the previous subsection, but now part of the magnets were removed. As we have mentioned in the introduction, this partial removal of magnets is made in commercial separators in order to facilitate visual contact with the dispersion during the separation process so that the separation can be monitored easily

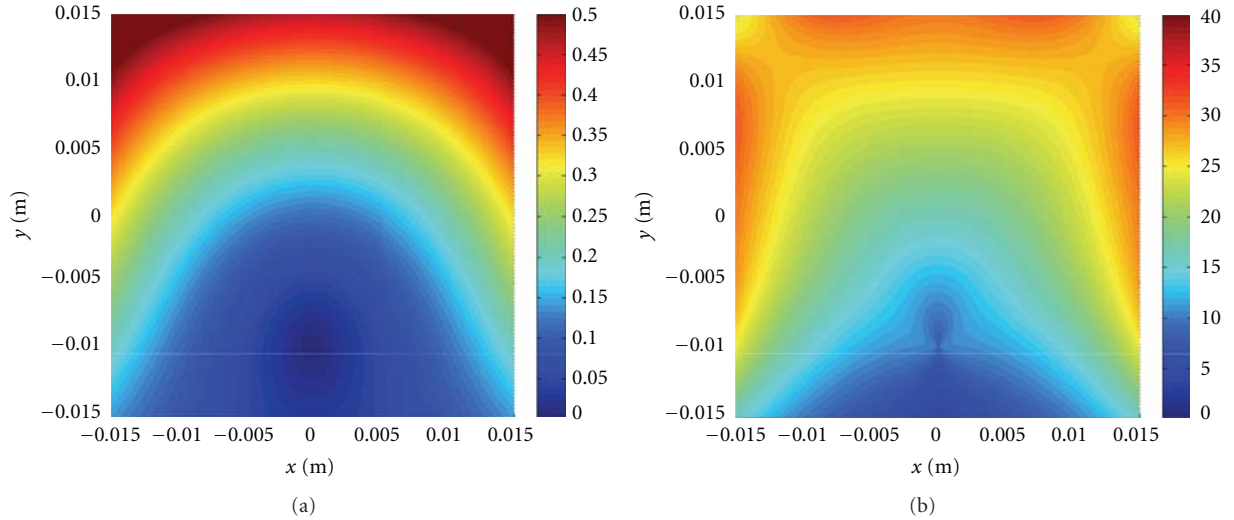


FIGURE 3: Profile of the magnitude of the magnetic field  $B$  in Tesla (a) and its gradient in Tesla/m (b) in the open-type magnetic separator employed in the simulations.

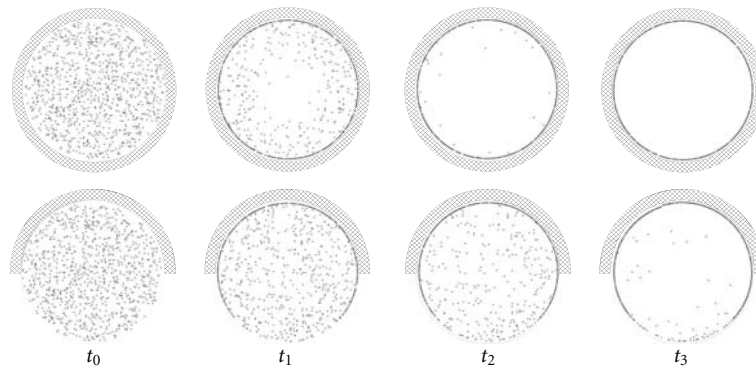


FIGURE 4: Series of snapshots extracted from simulations comparing the time evolution of the separation process in the closed-geometry (upper row) and open-geometry (bottom row) schemes. The snapshots are taken from a top view of the cylindrical separator with radial geometry. The different snapshots correspond to different times during separation ( $t_0 = 0$ ,  $t_1 = 1 \times 10^5$  s,  $t_2 = 2 \times 10^5$  s and  $t_3 = 5 \times 10^5$  s).

by eye inspection [19] (in closed type separators as the one considered in the previous subsection, monitoring of the separator process is made by an optical sensor, see, e.g., [13]). In Figure 3 we show the profile of the magnetic field generated by a hypothetical open-type magnetic separator constructed by removing half of the magnets from the closed type magnetic separator employed in the previous subsection. In this open case, the magnetic gradient is far from uniform. It is again about 30 T/m near the magnets, but now it is less than 10 T/m in a substantial part of the separator (the region far from the magnets). We will employ these profiles of magnetic field and gradient in order to compare the performance of the open and closed separator designs in a simulation of a specific example of magnetic separation.

In order to compare the different performance between the open and the closed type separators, we consider the same suspension of  $\gamma$ - $\text{Fe}_2\text{O}_3$  NPs of diameter 12 nm described in the previous subsection. Now we perform simulations for this suspension in the case of open-type geometry of the magnetic separator. The technical details (number of tracer

particles, time step, etc.) were the same as employed in the simulation of the previous subsection. Here, the simulations were performed until a simulation time of  $1.2 \times 10^6$  s, and the calculations required 39 min of CPU in a AMD Opteron Magny Cours 6136 processor. The corresponding results are presented in Figure 4 (snapshots) and Figure 5 (fraction of remaining particles as a function of time). The differences between results for both types of separators are clear. In the closed type geometry, the motion of particles is much more uniform since the magnetic gradient is nearly uniform in the whole system. In this case, separation proceeds by a radial motion of the particles towards the wall (following the magnetic gradient, see (7)), leaving a circle of “clear” solution (free of particles) which increases with time. In the open-type case, the distribution of particles becomes inhomogeneous as separation proceeds, because of the inhomogeneities in the magnetic gradient (see Figure 3). Particles close to the magnets move faster than the ones placed far from the magnets (Figure 4, top) since they experience larger magnetizations and larger magnetic gradients (see Figure 3). Also,

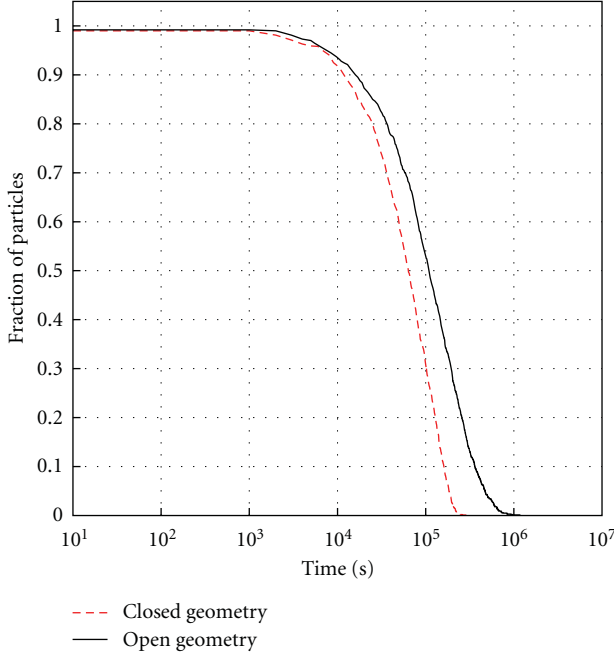


FIGURE 5: Comparison of the fraction of particles in solution as a function of time as obtained in tracer simulations for open and closed type magnetic separators with magnetic profiles shown in Figures 1 and 3 (see text for details).

these slow-moving particles have to travel distances larger than the cylinder radius in order to reach the walls of the system and become separated from the liquid. As a consequence, separation times are substantially longer in open-type separators than in closed type separators, as shown in Figure 5.

### 3. Magnetophoresis of Colloidal Particles in a Magnetic Fluid

**3.1. Motivation and Basic Equations.** The problem we would like to consider in this section is the motion of colloidal particles (with sizes of the order of hundreds of nm or larger) in a dispersion containing superparamagnetic NPs. This particularly asymmetric mixture has a fascinating behavior which has received significant attention in recent years. For example, it is possible to induce the assembly and transport of nonmagnetic colloids immersed in a dispersion of superparamagnetic NPs by applying external magnetic fields [26, 27]. Physically, this interesting behavior is due to the fact that a nonmagnetic colloidal particle, immersed in a suspension of NPs, behaves as a magnetic hole with an effective dipole pointing in a direction opposed to that of the local magnetization of the NPs. Hence, after the application of a magnetic field, a nonmagnetic colloid immersed in a dispersion of NPs behaves as an effective super-diamagnetic particle. This effect is not only found in nonmagnetic colloids but also it is possible in the case of composite colloidal particles made of superparamagnetic NPs embedded in a nonmagnetic matrix (e.g., polymer or silica). As demonstrated in [8, 28, 29]

theoretically and experimentally, a colloidal particle in a dispersion of superparamagnetic NPs under a magnetic field  $H$  behaves as having an effective magnetic dipole given by

$$m_{\text{eff}}(H) = m_c(H) - \frac{4}{3}\pi R_c^3 n_p m_p(H), \quad (11)$$

where  $m_c(H)$  is the intrinsic magnetic dipole of the colloid (the one observed when the colloid is not embedded in a dispersion of NPs),  $R_c$  is the radius of the colloid,  $n_p$  is the local concentration of NPs (in number of particles per unit volume), and  $m_p(H)$  is the magnetic dipole of the NPs induced by the external field  $H$ . Equation (11) can be interpreted as a magnetic buoyancy effect due to the different magnetic response of the colloid and its surroundings, as discussed in [8]. Note that a nonmagnetic colloid ( $m_c = 0$ ) will have always  $m_{\text{eff}} < 0$ , that is, a super-diamagnetic behavior with an effective dipole opposite to that of the superparamagnetic NPs. In the case of  $m_c > 0$ , the behavior of the colloids can be tuned to an effective superparamagnetic ( $m_{\text{eff}} > 0$ ) or super-diamagnetic ( $m_{\text{eff}} < 0$ ) behavior depending on the concentration of NPs.

Here, our interest will be the study of the behavior of a mixture of colloidal particles and NPs in a magnetic separator. Experimentally, this system has been studied in [30] in the case of a closed type separator. The magnetophoretic velocity of the superparamagnetic NPs will obey the same equations discussed in Section 2. In particular, the NPs will move in the direction of the magnetic gradient with a velocity given by (7). The magnetophoretic velocity of a colloidal particle  $v_c$  can be easily obtained using the same relations derived in Section 2 but taking into account that the magnetic dipole of the colloid is described by  $m_{\text{eff}}$  as given by (11). The result is given by

$$\vec{v}_c(\vec{r}) = \vec{v}_p(\vec{r}) \frac{R_p}{R_c} \left[ \frac{m_c}{m_p} - \frac{4}{3}\pi R_c^3 n_p(\vec{r}, t) \right], \quad (12)$$

where  $\vec{v}_p(\vec{r})$  is the magnetophoretic velocity of a NP located at  $\vec{r}$ , and  $n_p(\vec{r}, t)$  is the local concentration of NPs at  $\vec{r}$  and time  $t$ .

**3.2. Simulations: Methodology and Results.** The simulation methodology employed here is based on particle tracers simulations as developed in the previous section. Now, we will have two different types of tracer particles, one corresponding to NPs and another one corresponding to colloidal particles. For simplicity, we will consider the simulation of this mixture only in the case of closed type magnetic separators. The profile of the magnetic field is shown in Figure 1. As we have seen in the previous section, this case is more easy to understand due to the near uniformity of the magnetic gradient. In this case, the magnetic gradient is pointing in the radial direction, and it has a constant magnitude. Hence, (7) gives the following expression for the radial velocity of a NP at a radial distance  $r$  from the center of this cylindrical separator:

$$v_p(r) = \frac{2\mu_0 R_p^2 \rho_p M(H)}{9\eta} \frac{\partial H}{\partial r}, \quad (13)$$

where  $M(H)$  is given by (8) and (9). In the case of the colloidal particles, the radial velocity can be obtained from (12)

$$v_c(r) = v_p(r) \frac{R_p}{R_c} \left[ \frac{m_c}{m_p} - N_f(r, t) \right], \quad (14)$$

where  $N_f$  is the number of NPs “excluded” by the presence of a colloidal particle, and it is given by

$$N_f(\vec{r}, t) = \frac{4}{3} \pi R_c^3 n_p(\vec{r}, t). \quad (15)$$

Due to the symmetry of the problem, we consider only the radial motion of the particles so the simulations can be performed in 2 dimensions (the vertical coordinate  $z$  was ignored). As in the previous section, the equation of motion of the tracer NPs,  $dr/dt = v_p(r)$  was solved using the Verlet integration scheme. Also, we have to solve the motion of the tracer particles corresponding to the colloids. This is done as follows. At each time step (after updating the position of the NPs), we compute the concentration profile of NPs, and the function  $N_f(r, t)$  is updated in the following way. The value of  $N_f(r, t)$  is given by the initial value  $N_f^0$  multiplied by the ratio between the NPs density found in the region comprised between  $r$  and  $r + \delta r$  and the initial NPs density. Different combinations of integration time step and  $\delta r$  values were tested. The results reported here correspond to  $\delta r = L/100$  where  $L$  is the radius of the magnetic separator. Once this function is updated, the velocity of each colloidal tracer is calculated as follows. A first estimate of the velocity for each latex particle at a given time step  $v_1(t_n)$  is calculated according to the NPs concentration at time  $t_n$ . Then, each latex particle is moved to a new virtual position according to this initial estimate  $v_1(t_n)$ . Also, we update the position for each NP at time  $t_{n+1}$ , the new NPs concentration is computed, and a new estimation of the velocity of each latex particle (located at their virtual positions) is calculated  $v_2(t_{n+1})$ . Finally, the real velocity used to calculate the position at  $t_{n+1}$  for each latex particle is calculated as the average of these two estimates of the latex velocities that is,  $v(t_n) = (v_1(t_n) + v_2(t_{n+1}))/2$ . This two-steps, methodology is necessary in order to account for the effect of variations in NPs concentration during the motion of the latex particles.

In this case, we have performed a single simulation for a particular case of interest which is now being realized experimentally [30]. We have considered a mixture containing a dispersion of nanoparticles identical to that considered in the previous section (10 g/L dispersion of superparamagnetic  $\gamma$ -Fe<sub>2</sub>O<sub>3</sub> NPs of diameter 12 nm) and colloidal particles similar to commercial latex micro spheres (1 g/L dispersion of colloids with diameter 900 nm). In these conditions, the initial value of the quantity  $N_f$  defined in (15) is  $N_f^0 = 868$  in all the system. As we said before, the magnetic separator considered here is the same closed type separator with a gradient of approximately 30 T/m discussed in Section 2.2. Under these conditions, the behavior of the NPs is the same as discussed in Section 2.2. The behavior of the latex colloids depends strongly on the value considered for  $m_c$ . The most interesting case corresponds to the case with  $m_c/m_p < N_f$ . In this situation, (14) predicts that the initial motion of the colloidal particles will be in the opposite direction to that of NPs. In our

simulations, we have focused in the particular case  $m_c/m_p = 500$ , which we have found realizable experimentally [30].

We have performed different simulations with a total number of  $10^6$  tracer NPs together with  $10^4$  tracer latex particles. The initial system configuration was prepared by placing all the particles at random positions inside the separator of radius 1.5 cm. As in previous simulations, the solvent viscosity was set to 0.001 Pa · s which corresponds to the viscosity of water at 298 K. The integration time step was set to  $\Delta t = 5$  s, and the positions of the particles were recorded at intervals of 50 s. The simulation was performed until a simulated time of  $2.9 \times 10^5$  s, which required 131 min of CPU. At this point, we recall that all our calculations were performed by a C code developed in house, which is available under request to the authors.

Experimentally [30], it was observed that the latex particles behave in an interesting, nontrivial way. First, it was observed that latex colloids generate a sort of ring-shaped structure. Then, this ring of latex particles experiences a thinning process, and later it moves towards the walls of the system. This experimental behavior is also found in our simulations, as seen in the snapshots in Figure 6, and also it can be seen in the movies provided as supporting online information (see the movies provided in supplementary material available online at doi:10.1155/2012/678581).

The observed profiles of latex particles can be understood from the analysis of the trajectories of individual tracers. Typical trajectories for the radial distance  $r(t)$  of latex particles are shown in Figure 7. Latex particles move initially towards the center of the system due to the fact that initially  $m_{\text{eff}} < 0$  (see (11)). As time advances, the latex motion is slowed down and at certain point (different for each particle), the motion is reversed. For example, a particle starting near the center of the system ( $r = 0.1$  cm) reverses its motion after 1 h, reaching the wall after a total of 31 h. A particle starting at the wall (at  $r = 1.5$  cm) reverses its motion after 10 h, at a distance  $r = 0.7$  cm and reaches the wall ( $r = 1.5$  cm) also after 31 h. This reversal of latex motion is due to the radial motion of the NPs towards the walls, which changes the local concentration of NPs. The reversal of the trajectory of a latex particle occurs when it finds a decreased local concentration of NPs at which  $m_{\text{eff}} = 0$  ((12) gives a threshold NP concentration of 5.8 g/L for our case). This initial motion towards the center of the system generates the observed formation and thinning of the ring profile of latex particles shown in Figure 6. The subsequent motion of the ring profile of latex towards the wall corresponds to the time at which all latex particles have inverted their motion. All this process is also illustrated in the accompanying movies, showing the motion of latex particles superimposed to the evolution of the concentration profiles of NPs.

**3.3. Simplified Model.** Although our simulations described in the previous section are not particularly costly from the computational point of view, they require the use of relatively large amounts of disk space to store the tracer trajectories and later analysis to obtain relevant quantities such as concentration profiles and number of particles remaining inside the magnetic separator. For this reason, it could be convenient to

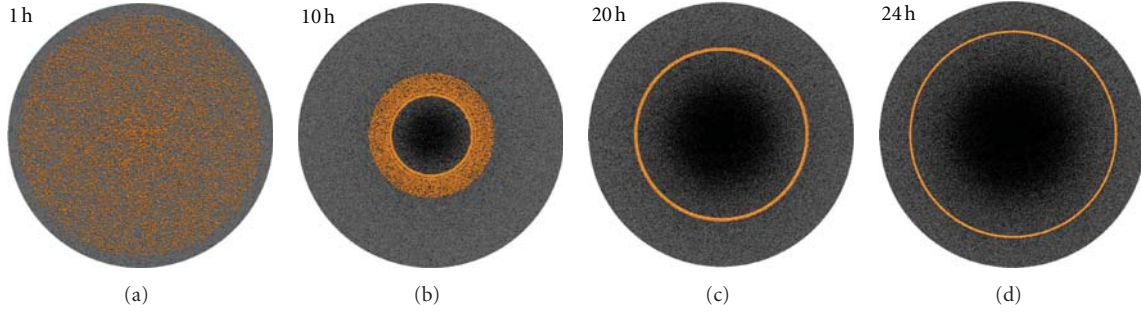


FIGURE 6: Snapshots from simulations of the magnetophoresis of an aqueous dispersion of  $\gamma$ -Fe<sub>2</sub>O<sub>3</sub> superparamagnetic nanoparticles (grey) and latex polystyrene particles (orange) under a magnetic gradient of 30 T/m at different times (1 h, 10 h, 20 h, and 24 h resp.).

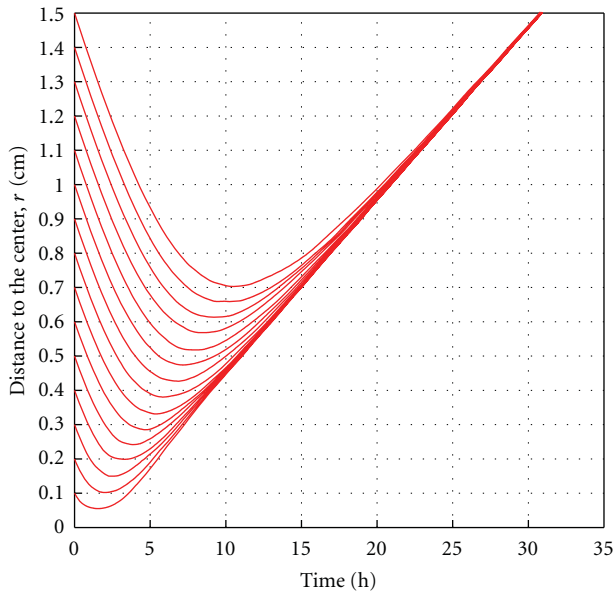


FIGURE 7: Examples of 15 trajectories obtained in simulations corresponding to tracer latex particles immersed in a dispersion of NPs starting from different distances to the center of the system (see details in the text.)

develop a simplified approach amenable of solution without the need of performing computer simulations.

The motion of the latex particles observed in the simulations can be described with reasonable accuracy with a simple equation. The basic idea is to disregard the radial dependence in the magnetophoretic velocity of the NPs in (13) and assume that the NPs move at constant velocity  $v_p^s$  which is the magnetophoretic velocity at magnetic saturation

$$v_p^s = \frac{2R_p^2}{9\eta} \mu_0 \left( \frac{\partial H}{\partial r} \right) M_s \rho_p. \quad (16)$$

This approximation is justified by the observation that the magnetic field observed in most parts of the magnetic separator (see Figure 1) is large enough to saturate the NPs. In the case of the 10 g/L suspension of  $\gamma$ -Fe<sub>2</sub>O<sub>3</sub> NPs under 30 T/m considered in our previous subsection, we have  $v_p^s =$

$7.9 \times 10^{-8}$  m/s. Within this approximation, the concentration profile of NPs is given approximately by

$$n_p(r, t) = n_0 \left( 1 - \frac{v_p^s t}{r} \right) \quad \text{for } r > v_p^s t, \quad (17)$$

$$n_p(r, t) = 0 \quad \text{for } r < v_p^s t. \quad (18)$$

Using (16)–(18) in (14), we obtain that the trajectory of a latex particle obeys the differential equation

$$\frac{dr}{dt} = v_c(r) = v_p^s \frac{R_p}{R_c} \left[ \frac{m_c}{m_p} - \frac{4}{3} \pi R_c^3 n_0 \left( 1 - \frac{v_p^s t}{r} \right) \right]. \quad (19)$$

Equation (19) is a first-order differential equation which can be solved numerically to obtain the trajectory  $r(t)$  for a latex particle initially at a position  $r(t=0) = r_0$ . In Figure 8 we compare the predictions of (19) with the results obtained from tracer simulations. In general, numerical solutions of (19) give a reasonable approximation to colloid trajectories with differences of the order of 10% with simulations. This result is remarkable in view of the apparently strong approximations involved in their derivation (see (16) and (18)). Therefore, in order to estimate systematically the effect of the different parameters of the system (e.g., the effect of the value of  $m_c$ ), it could be convenient in practice to solve numerically (19) instead of performing a full simulation. However, for more complex magnetic field geometries, to get analytical solutions becomes much more difficult, and numerical simulations as the ones presented here would be necessary.

## 4. Conclusions

In this work, we have presented a low-cost simulation strategy based on the concept of particle tracers aimed to tackle the magnetophoresis process in the noncooperative magnetophoretic regime. We have successfully validated this simulation approach by comparing the results obtained against existing experimental and also analytical results obtained for the separation process of a colloidal dispersion of  $\gamma$ -Fe<sub>2</sub>O<sub>3</sub> superparamagnetic nanoparticles in an aqueous solution. Thanks to this methodology, we have been able to evaluate different key factors involved in the magnetophoretic

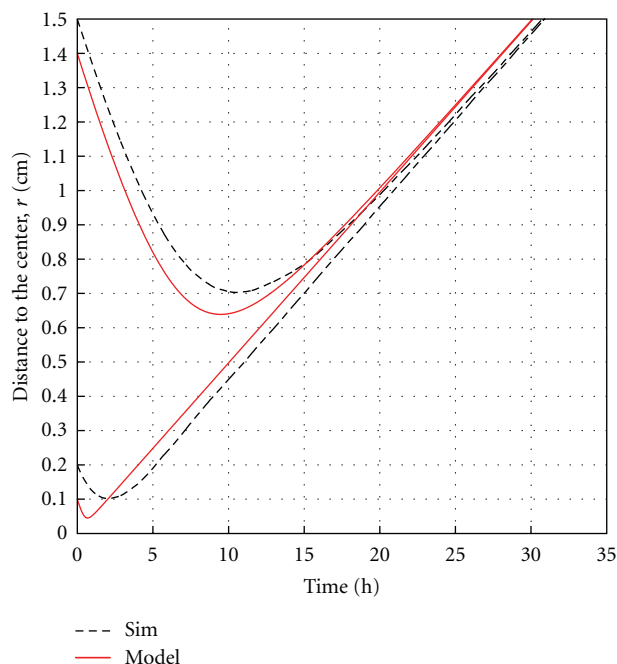


FIGURE 8: Comparison of trajectories of two tracer latex particles as obtained in the simulations and by numerical solution of (19).

separation process. Regarding the separator design, we have shown that the homogeneous magnetophoretic conditions created by a closed type separator (high magnetic field over almost the whole sample and constant magnetic gradient) enhance the separation process, providing more control over the process and reducing the expected separation time when compared to the open-type version of the separator. We have also extended that methodology to solutions of colloidal particles in aqueous solutions of superparamagnetic nanoparticles in the closed type geometry. The simulation performed in this case is able to account for the ring-like structure expected in some experimental situations and agrees with the simplified numerical model proposed.

## Acknowledgments

This work was supported by the Spanish Government Grants no. FIS2009-13370-C02-02, PET2008-02-81-01/02, and CONSOLIDER-NANOSELECT-CSD2007-00041. J. Faraudo and J. Camacho are also supported by the Catalan Government Grant no. 2009SGR164. The authors thank LL. M. Martínez from SEPMAG Technologies for help regarding the calculation of the profiles of the magnetic fields and for extensive discussions.

## References

- [1] C. T. Yavuz, A. Prakash, J. T. Mayo, and V. L. Colvin, "Magnetic separations: from steel plants to biotechnology," *Chemical Engineering Science*, vol. 64, no. 10, pp. 2510–2521, 2009.
- [2] C. De Latour, "Magnetic separation in water pollution control," *IEEE Transactions on Magnetics*, vol. 9, no. 3, pp. 314–316, 1973.
- [3] G. Mariani, M. Fabbri, F. Negrini, and P. L. Ribani, "High-Gradient Magnetic Separation of pollutant from wastewaters using permanent magnets," *Separation and Purification Technology*, vol. 72, no. 2, pp. 147–155, 2010.
- [4] C. T. Yavuz, J. T. Mayo, W. W. Yu et al., "Low-field magnetic separation of monodisperse  $\text{Fe}_3\text{O}_4$  nanocrystals," *Science*, vol. 314, no. 5801, pp. 964–967, 2006.
- [5] J. L. Corchero and A. Villaverde, "Biomedical applications of distally controlled magnetic nanoparticles," *Trends in Biotechnology*, vol. 27, no. 8, pp. 468–476, 2009.
- [6] K. M. Krishnan, "Biomedical nanomagnetism: a spin through possibilities in imaging, diagnostics, and therapy," *IEEE Transactions on Magnetics*, vol. 46, no. 7, Article ID 5439840, pp. 2523–2558, 2010.
- [7] I. Safarik and M. Safarikova, "Magnetic techniques for the isolation and purification of proteins and peptides," *BioMagnetic Research and Technology*, vol. 2, no. 1, article no. 7, 2004.
- [8] G. Friedman and B. Yellen, "Magnetic separation, manipulation and assembly of solid phase in fluids," *Current Opinion in Colloid and Interface Science*, vol. 10, no. 3-4, pp. 158–166, 2005.
- [9] G. D. Moeser, K. A. Roach, W. H. Green, T. A. Hatton, and P. E. Laibinis, "High-gradient magnetic separation of coated magnetic nanoparticles," *AIChE Journal*, vol. 50, no. 11, pp. 2835–2848, 2004.
- [10] C. P. Bean and J. D. Livingston, "Superparamagnetism," *Journal of Applied Physics*, vol. 30, no. 4, pp. S120–S129, 1959.
- [11] D. Leun and A. K. Sengupta, "Preparation and characterization of magnetically active polymeric particles (MAPPs) for complex environmental separations," *Environmental Science and Technology*, vol. 34, no. 15, pp. 3276–3282, 2000.
- [12] E. Taboada, R. Solanas, E. Rodríguez, R. Weissleder, and A. Roig, "Supercritical-fluid-assisted one-pot synthesis of biocompatible core( $\gamma\text{-Fe}_2\text{O}_3$ )/shell( $\text{SiO}_2$ ) nanoparticles as high relaxivity  $T_2$ -contrast agents for magnetic resonance imaging," *Advanced Functional Materials*, vol. 19, no. 14, pp. 2319–2324, 2009.
- [13] G. De Las Cuevas, J. Faraudo, and J. Camacho, "Low-gradient magnetophoresis through field-induced reversible aggregation," *Journal of Physical Chemistry C*, vol. 112, no. 4, pp. 945–950, 2008.
- [14] J. Faraudo and J. Camacho, "Cooperative magnetophoresis of superparamagnetic colloids: theoretical aspects," *Colloid and Polymer Science*, vol. 288, no. 2, pp. 207–215, 2010.
- [15] M. Benelmekki, C. Caparros, A. Montras, R. Gonçalves, S. Lanceros-Mendez, and L. M. Martínez, "Horizontal low gradient magnetophoresis behaviour of iron oxide nanoclusters at the different steps of the synthesis route," *Journal of Nanoparticle Research*, vol. 13, no. 8, pp. 3199–3206, 2011.
- [16] M. Benelmekki, A. Montras, A. J. Martins, P. J. G. Coutinho, and L. M. Martínez, "Magnetophoresis behaviour at low gradient magnetic field and size control of nickel single core nanobeads," *Journal of Magnetism and Magnetic Materials*, vol. 323, no. 15, pp. 1945–1949, 2011.
- [17] J. S. Andreu, J. Camacho, J. Faraudo, M. Benelmekki, C. Rebollo, and L. M. Martínez, "Simple analytical model for the magnetophoretic separation of superparamagnetic dispersions in a uniform magnetic gradient," *Physical Review E*, vol. 84, no. 2, Article ID 021402, 2011.
- [18] G. P. Hatch and R. E. Stelter, "Magnetic design considerations for devices and particles used for biological high-gradient

- magnetic separation (HGMS) systems,” *Journal of Magnetism and Magnetic Materials*, vol. 225, no. 1-2, pp. 262–276, 2001.
- [19] S. J. Hershberger, A. Parakka, B. Trudeau, C. Patel, and P. Schultz, “Scalable magnetic designs to achieve comparable capture rates and capture efficiency across multiple vessel diameters,” *AIP Conference Proceedings*, vol. 1311, pp. 351–362, 2010.
- [20] J. S. Andreu, J. Camacho, J. Faraudo, M. Benelmekki, C. Rebollo, and L. Martínez, “Magnetophoretic separation of superparamagnetic dispersions in a uniform magnetic gradient: experimental study and analytical solution,” in *Proceedings of the 4th Iberian Meeting on Colloids and Interfaces*, pp. 191–197, 2011.
- [21] R. Kaiser and G. Miskolczy, “Magnetic properties of stable dispersions of subdomain magnetite particles,” *Journal of Applied Physics*, vol. 41, no. 3, pp. 1064–1072, 1970.
- [22] R. Rosensweig, *Ferrohydrodynamics*, Cambridge University Press, New York, NY, USA, 1st edition, 1985.
- [23] D. X. Chen, A. Sanchez, E. Taboada, A. Roig, N. Sun, and H. C. Gu, “Size determination of superparamagnetic nanoparticles from magnetization curve,” *Journal of Applied Physics*, vol. 105, no. 8, Article ID 083924, 2009.
- [24] J. J. Monaghan, “Particle methods for hydrodynamics,” *Computer Physics Reports*, vol. 3, no. 2, pp. 71–124, 1985.
- [25] D. Frenkel and B. Smit, *Understanding Molecular Simulations*, Academic Press, 2nd edition, 2001.
- [26] B. B. Yellen, O. Hovorka, and G. Friedman, “Arranging matter by magnetic nanoparticle assemblers,” *Proceedings of the National Academy of Sciences of the United States of America*, vol. 102, no. 25, pp. 8860–8864, 2005.
- [27] R. M. Erb, H. S. Son, B. Samanta, V. M. Rotello, and B. B. Yellen, “Magnetic assembly of colloidal superstructures with multipole symmetry,” *Nature*, vol. 457, no. 7232, pp. 999–1002, 2009.
- [28] R. M. Erb and B. B. Yellen, “Concentration gradients in mixed magnetic and nonmagnetic colloidal suspensions,” *Journal of Applied Physics*, vol. 103, no. 7, Article ID 07A312, 2008.
- [29] R. M. Erb, D. S. Sebba, A. A. Lazarides, and B. B. Yellen, “Magnetic field induced concentration gradients in magnetic nanoparticle suspensions: theory and experiment,” *Journal of Applied Physics*, vol. 103, no. 6, Article ID 063916, 2008.
- [30] M. Benelmekki, L. M. Martínez, J. Andreu, J. Faraudo, and J. Camacho, “Magnetophoresis of colloidal particles in a dispersion of superparamagnetic nanoparticles: theory and experiments,” *Soft Matter*. In press.

## Research Article

# Angular Response of Magnetostrictive Thin Films

Jianjun Li<sup>1,2</sup>

<sup>1</sup>National Key Laboratory of Science and Technology on Advanced Composites in Special Environments, Harbin Institute of Technology, Harbin 150080, China

<sup>2</sup>Laboratoire de Magnétisme de Bretagne, Université de Bretagne Occidentale, 6 Avenue le Gorgeu C.S. 93837, 29238 Brest Cedex 3, France

Correspondence should be addressed to Jianjun Li, ljj8081@tom.com

Received 14 November 2011; Revised 12 January 2012; Accepted 13 January 2012

Academic Editor: Ovidiu Crisan

Copyright © 2012 Jianjun Li. This is an open access article distributed under the Creative Commons Attribution License, which permits unrestricted use, distribution, and reproduction in any medium, provided the original work is properly cited.

The magnetostrictions of the single TbFe layer and coupled Py/TbFe<sub>2</sub> bilayers were measured by using laser deflectometry. The dependences of the magnetostriction performance on the driving magnetic field direction have been investigated. The relationship studies between the saturation bending angle and torsion angle of the single layer with perpendicular anisotropy and coupled bilayers with in-plane uniaxial anisotropy have been conducted. Interesting “jump” reflecting the spin dynamics is observed in the magnetostriction loops of the coupled bilayers.

## 1. Introduction

Magnetostrictive films have already shown promising applications in micromechanical devices since the discovery of giant magnetostriction in the Laves phase of TbFe<sub>2</sub> by Clark and Belson in 1972 [1, 2]. In the past, extensive experimental studies were undertaken to investigate the relationships between the observed magnetostrictive properties and the film composition, preparation conditions, anisotropy, and so forth, [3–8]. In order to reduce the huge magnetic switching field for TbFe<sub>2</sub> alloy and make it suitable for practical applications, Quandt and coworkers combined the rare-earth-transition-metal (RE-TM) alloys with soft magnetic materials, which have high magnetization to form coupled multilayers [9, 10]. The interfacial exchange-coupling between the RE-TM alloys and the soft magnetic materials plays an important role in reducing the magnetic switching field. The magnetostriction of magnetic exchange-spring multilayers has been investigated [11–14], but the first and the last layer are not in the same conditions as the internal layers in a multilayer system. Thus, their properties represent an average of different parameters. Eventual technological differences in the properties of different layers and interfaces are also hidden in a multilayer system. It is necessary and very useful to study the magnetostriction of magnetically coupled bilayers so as to reach better understanding of the mic-

roscopic spin configuration in such magnetic thin films. In this paper, the weak magnetostrictive signals of S/Py/TbFe<sub>2</sub>-coupled bilayers were obtained successfully and the dependences of the saturation magnetostriction of S/TbFe<sub>2</sub>-single layer and S/Py/TbFe<sub>2</sub>-coupled bilayers on the driving magnetic field direction were studied.

## 2. Experimental

Rectangular Corning glass was chosen as substrate (22 × 5 × 0.16 mm<sup>3</sup>), and TbFe<sub>2</sub> and Py layers were deposited onto it from 4 inch targets mosaic by using a Z550 Leybold RF sputtering equipment with a rotary table technique. During the film deposition, a static magnetic field (around 0.03 T) was set along the long axis of the rectangular substrate to favour in-plane uniaxial magnetic anisotropy in the soft magnetic film. A 3 nm copper protective layer was grown onto the samples. The TbFe<sub>2</sub> layer is amorphous and sputtered under argon gas pressure of  $1.2 \times 10^{-2}$  mbar from an alloy target with a nominal composition of TbFe<sub>2</sub> (99.9% in purity), while Py is polycrystalline and sputtered under argon gas pressure of  $1.2 \times 10^{-2}$  mbar from an alloy target with a nominal composition of Ni<sub>80</sub>Fe<sub>20</sub> (99.99% in purity). The deposition rates are 6.2 Å/s for TbFe<sub>2</sub> layer and 4 Å/s for Py layer. The single layer and coupled bilayers studied in this

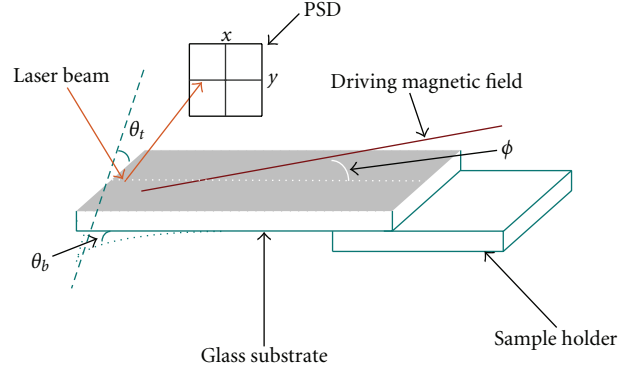


FIGURE 1: Outline of the measurement of magnetoelastic deformations (bending and torsion angles). The dashed line indicates the long axis of the sample.  $\phi$  is the angle between the long axis of the sample and the driving magnetic field.

paper had the following configurations: [S/TbFe<sub>2</sub> (1.24  $\mu$ m)] and [S/Py (10 nm)/TbFe<sub>2</sub> (10 nm)].

The magnetostrictions of S/TbFe<sub>2</sub>-single layer and S/Py/TbFe<sub>2</sub>-coupled bilayers were obtained by laser deflectionometry. Figure 1 outlines the magnetostrictive measurement of the magnetic films. He-Ne laser strikes on the sample surface and is reflected by the sample to reach PSD (Hamamatsu S1300 position sensitive detector) surface. When the magnetic field is applied and deformation of the substrate occurs, the deflections can be recorded simultaneously. The PSD gives a voltage proportional to the position of the laser spot on the detecting surface and provides continuous position data on both the X and Y axes, so the angular deformations of the sample (bending angle  $\theta_b$  and torsion angle  $\theta_t$ ) can be measured [13]. Angle  $\phi$  is the angle between the driving magnetic field and the long axis of the rectangular substrate. In our studies, angle  $\phi$  can be varied from 0 to 360° by rotating the electromagnet. The driving magnetic field is always kept in the film plane. The hysteresis loops were performed on a vibrating sample magnetometer (VSM).

### 3. Results and Discussion

**3.1. Single TbFe<sub>2</sub> Layer.** The magnetostriction loops of the TbFe<sub>2</sub>-single layer measured at different angles  $\phi$  ( $\phi = 15, 75, 90, 105, 165, 195^\circ$ ) are displayed in Figure 2. When the driving magnetic field is not applied, no magnetostriction occurs. The driving magnetic field up to 0.7 T is applied for the magnetostriction measurement of TbFe<sub>2</sub> single layer. If the magnetic field is not strong enough, the saturation magnetostriction of TbFe<sub>2</sub> layer cannot be observed for its the strong anisotropy. In Figure 2(a),  $\theta_b$  and  $\theta_t$  reach the maximum negative value at the saturation field, then the absolute values of  $\theta_b$  and  $\theta_t$  decrease to zero following the decrease of the driving magnetic field. After the driving magnetic field changes to the opposite direction and starts to increase again, the absolute values of  $\theta_b$  and  $\theta_t$  increase smoothly till they reach the same maximum negative values. When the angle  $\phi$  is changed by rotating the electromagnet, similar results are observed except the differences of the saturation magnetostriction and the sign of the deformation angle.

Figure 3 shows the saturation magnetostriction of TbFe<sub>2</sub>-single layer as a function of angle  $\phi$ . According to the results,  $\theta_{\text{bsat}}(\phi)$  and  $\theta_{\text{tsat}}(\phi)$  curves have  $\cos^2(\phi)$  and  $\sin^2 \phi$  characteristics, respectively. The functions  $A_1(\cos^2(\phi + \phi_1) + B_1)$  and  $A_2(\sin^2(\phi + \phi_2) + B_2)$  are used to fit, where  $\phi_1$  and  $\phi_2$  represent the correction angle of the sample misorientation calculated from bending and torsion angle, and A and B are constants: A means the oscillation amplitude and B indicates the easy axis deviation from the long axis of the sample. According to fitting, the simulated curves are shown in Figure 3 and the functions for TbFe<sub>2</sub> single layer are  $\theta_{\text{bsat}}(\phi) = -1.05(\cos^2(\phi - 2^\circ))$ ;  $\theta_{\text{tsat}}(\phi) = -0.41(\sin^2(\phi + 6^\circ) + 0.24)$ . According to the equation in [13]

$$\theta_{\text{sat}} = \frac{6(1 + \nu_s)Lt_f}{E_s t_s^2} b^{\gamma^2}, \quad (1)$$

one can calculate the magnetoelastic coupling coefficient  $b^{\gamma^2}$  of the magnetostrictive thin films. Here  $E_s$  and  $\nu_s$  are the Young modulus and Poisson ratio of the substrate, respectively.  $L$  is the sample length (20 mm), while  $t_s$  represents the glass substrate thickness and  $t_f$  is the film thickness (including Py and TbFe<sub>2</sub> for coupled bilayers). For the glass substrate,  $t_s$  is 0.16 mm and  $E_s = 60$  GPa and  $\nu_s = 0.27$ . Based on the results, magnetoelastic coupling coefficient of TbFe<sub>2</sub>-single layer in our experiments is  $b^{\gamma^2}_{\text{single layer}} = 8.53$  MPa, which is similar to what have been reported before [15].

It is known that the TbFe<sub>2</sub> film has a perpendicular easy axis. Several models including pair ordering [16], anelastic distortion of magnetic atom environment [17], and hexagonal planar units with a preferred axis perpendicular to the film plane [18, 19] have been proposed to account for the origin of the perpendicular anisotropy of TbFe<sub>2</sub> film. In ideal ferrimagnetic TbFe<sub>2</sub>-single layer, the model in Figure 4(a) can be used to explain the angular response of the saturation magnetostriction. Hysteresis loops (Figure 4(b)) of TbFe<sub>2</sub> single layer with field in plane ( $\phi = 0$  and  $90^\circ$ ) have no difference. Also the hysteresis loops (Figure 4(c)) of TbFe<sub>2</sub> single layer with field in plane and perpendicular to plane confirm the existence of the perpendicular anisotropy in the film. When the magnetic field is applied, the magnetic vectors rotate into the film plane and subsequently change the internal

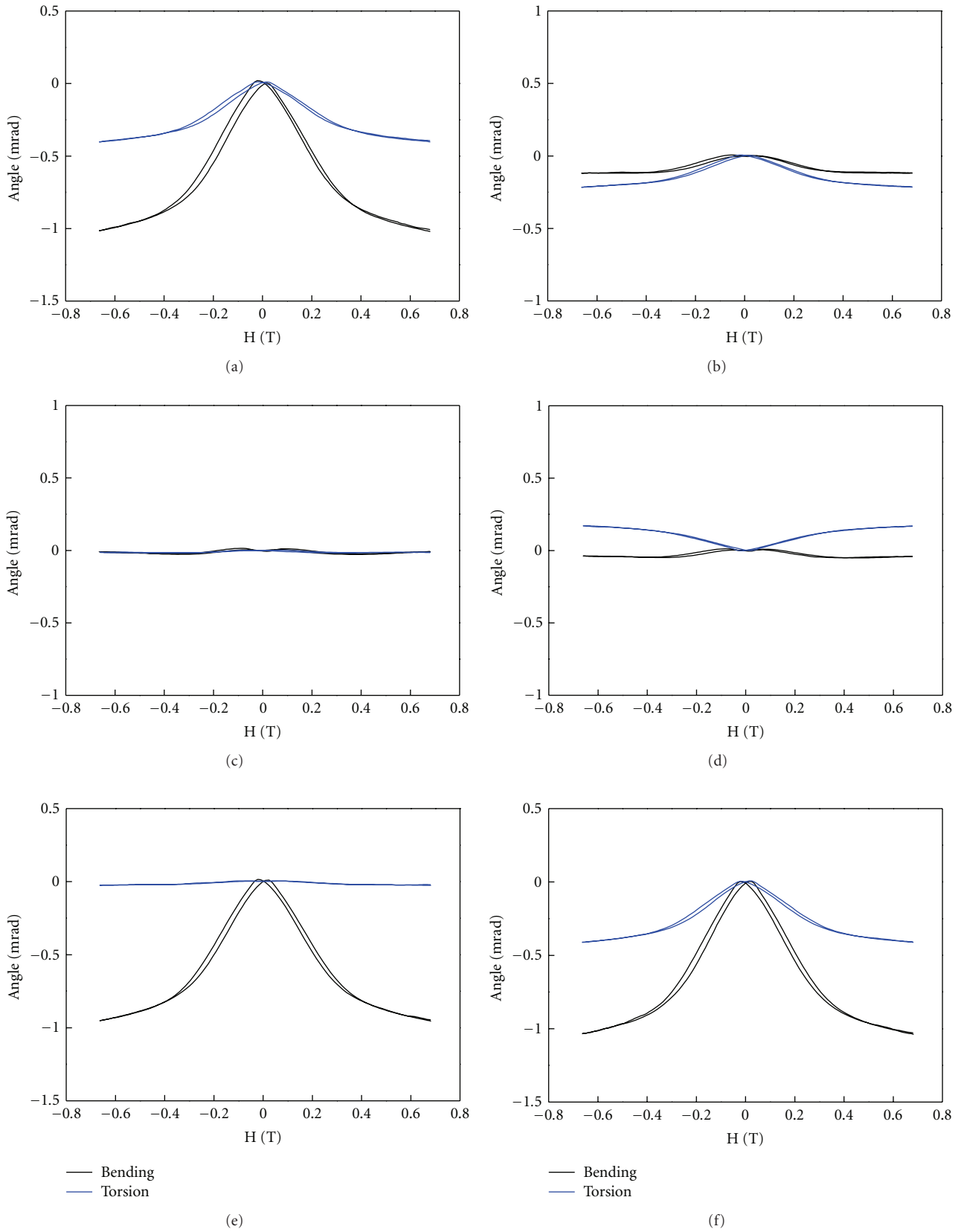


FIGURE 2: Experimental magnetostriction loops of TbFe<sub>2</sub> single layer at different driving field angles ( $\phi = 15, 75, 90, 105, 165, 195^\circ$  : (a)–(f)).

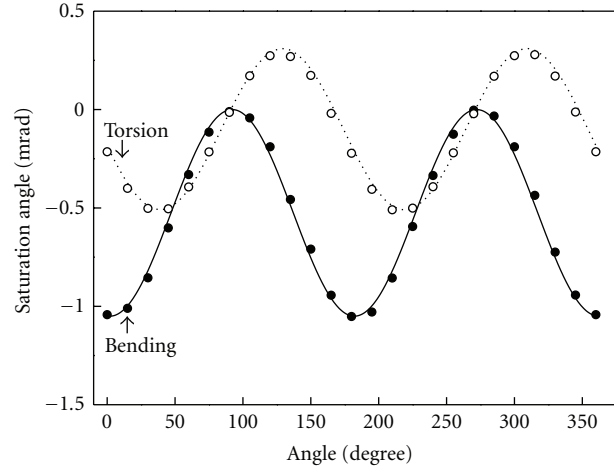


FIGURE 3: The saturation bending angle  $\theta_b$  and torsion angle  $\theta_t$  for  $\text{TbFe}_2$  single layer as a function of angle  $\phi$  ( $\phi$  varying every  $15^\circ$  from  $0$  to  $360^\circ$ ). The experimental data are represented by circles, and the fit is illustrated by line (bending: solid; torsion: dot).

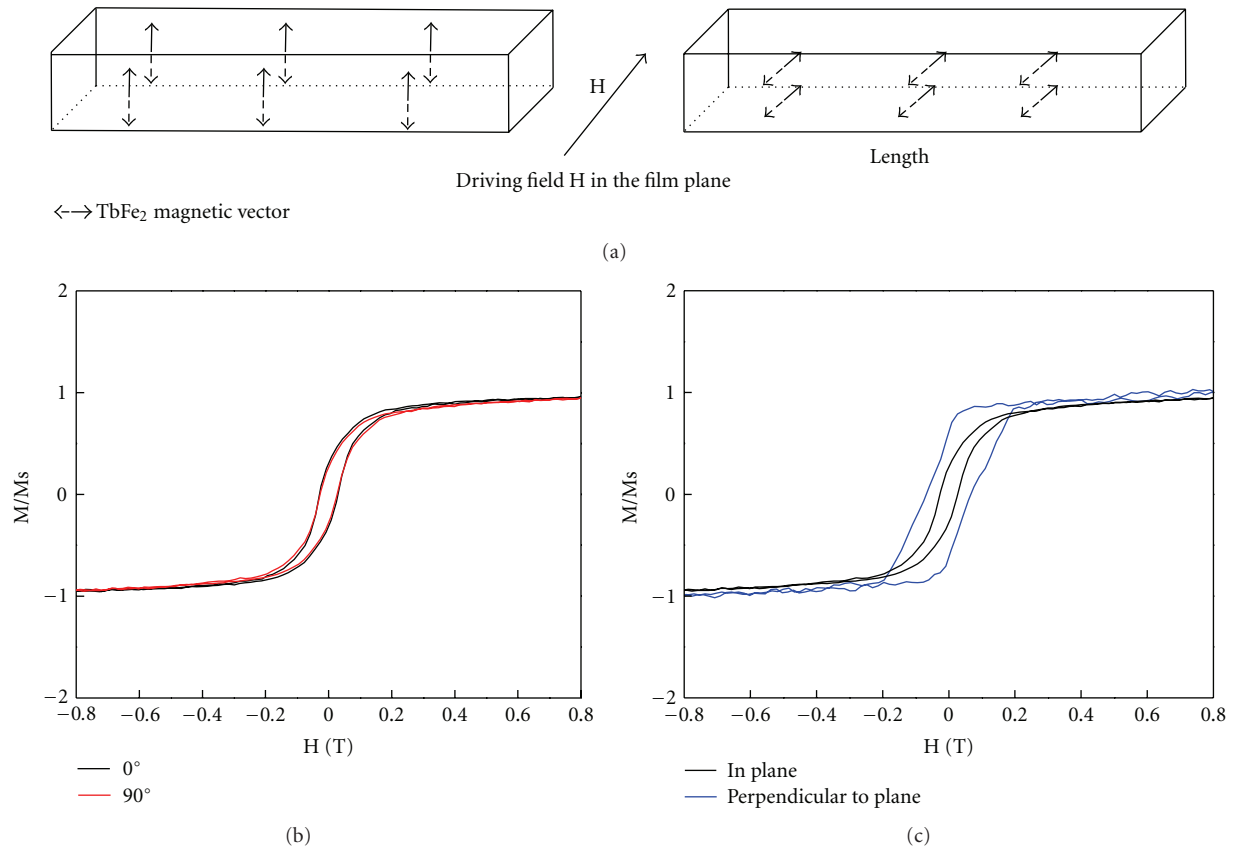


FIGURE 4: (a) Schematic drawing of the magnetic vector rotation model for  $\text{TbFe}_2$  single layer ( $H$ : the driving magnetic field); (b) hysteresis loops of single  $\text{TbFe}_2$  layer with field in plane ( $\phi = 0$  and  $90^\circ$ ); (c) hysteresis loops of single  $\text{TbFe}_2$  layer with field in plane and perpendicular to plane.

stress. The different saturation magnetostrictions are caused by the different  $\text{TbFe}_2$  spin configurations with varied field direction. The  $\text{TbFe}_2$  film has the maximum saturation magnetostriction when the  $\text{TbFe}_2$  vectors rotate into the film

plane along the long axis of the sample, but nearly zero magnetostriction is observed when the magnetic field is applied perpendicular to the long axis of the sample ( $\phi = 90^\circ$ ). Such phenomenon results from the rectangular shape of the

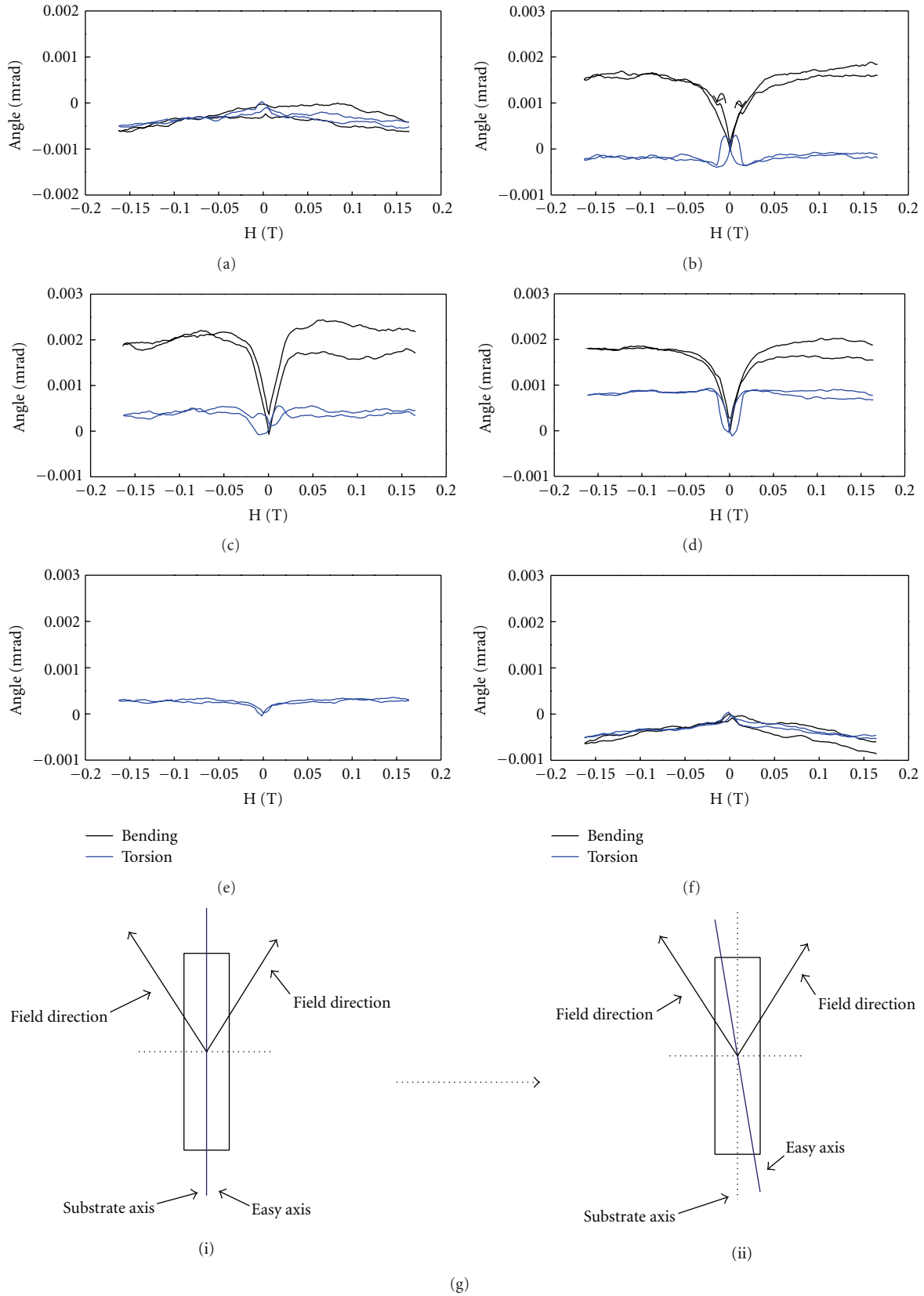


FIGURE 5: Representative magnetostriction loops (solid line: bending; dot line: torsion) of  $S/Py/TbFe_2$ -coupled bilayers at different driving field angle ( $\phi = 15, 75, 90, 105, 165, 195^\circ$ : (a)–(f)); graphical representations (i) and (ii) reveal the deviation of easy axis from the long axis of the sample.

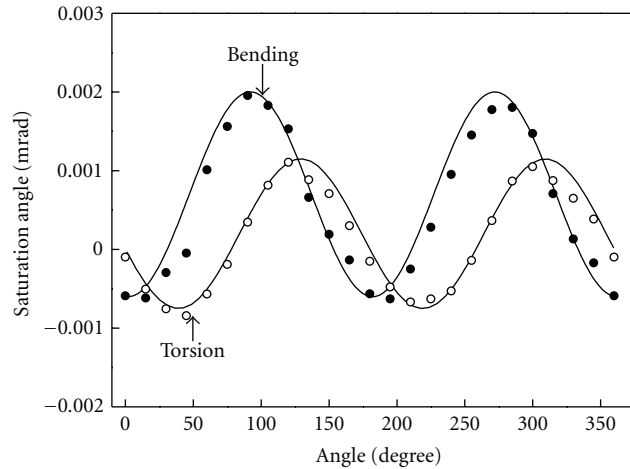


FIGURE 6: The saturation bending angle  $\theta_b$  and torsion angle  $\theta_t$  of S/Py/TbFe<sub>2</sub> bilayers as a function of angle  $\phi$  ( $\phi$  varying every 15° from 0 to 360°). The experimental data are represented by circles, and the fit is illustrated by line (bending: solid; torsion: dot).

substrate, and the cantilever structure makes the substrate hard to distort along the perpendicular direction (The cantilever is fixture).

**3.2. S/Py/TbFe<sub>2</sub>-Coupled Bilayers.** The angular responses of  $H_{EX}$  (exchange bias) and  $H_C$  (coercivity) in FM/AFM coupled bilayers have been reviewed by Ambrose et al. [20]. The angular response of the saturation magnetostriction of S/Py/TbFe<sub>2</sub>-coupled bilayers is investigated in this section. The angle  $\phi$  is changed every 15° from 0 to 360°, and representative magnetostriction loops of the coupled bilayers measured at different angle  $\phi$  ( $\phi = 15, 75, 90, 105, 165, 195^\circ$ ) are shown in Figure 5. In Figure 5(a), small negative bending and torsion occur. When  $\phi$  increases, the exchange-coupling effect starts to show more clearly, the saturation torsion angle  $\theta_{tsat}$  in Figure 5(b) is negative, but the saturation bending angle  $\theta_{bsat}$  becomes positive. The “jump” appears in the magnetostriction loop as indicated in Figure 5(b). In the magnetostriction loops of the coupled bilayers, the “jump” is only observed over a restricted range of angle  $\phi$ . In Figures 5(c) and 5(d), both the saturation bending and torsion angles turn positive. And the magnetostriction loops in Figure 5(f) are the same as that shown in Figure 5(a), implying that  $MS(\phi)$  magnetostriction loop is the same as  $MS(\phi + 180^\circ)$ .  $MS(\phi)$  and  $MS(-\phi)$  magnetostriction loops of the coupled bilayers are different in our results, which are caused by the deviation of easy axis from the long axis of the sample (graphical representations in Figure 5). A much smaller magnetic field can reach the saturation magnetostriction for the coupled bilayers and the exchange-coupling effect can reduce the switching magnetic field effectively.

The coupled bilayers have a uniaxial anisotropy in the film plane and the maximum saturation magnetostriction appears when  $\phi$  is about 90°, which differs greatly from the TbFe<sub>2</sub> single layer. The difference comes from the exchange-coupling effect between the Py and TbFe<sub>2</sub> layers, which results in the uniaxial magnetic anisotropy in the film plane. When the field is applied along the easy axis, the magnetization changes by the 180° domain wall displacement and

there is no magnetostrictive effect. To the contrary, if the field is applied along the hard axis, the magnetic vectors turn by 90° and the maximum saturation magnetostriction is observed. The fitting curves for the saturation magnetostriction of the coupled bilayers shown in Figure 6 also have  $\cos^2(\phi)$  and  $\sin^2\phi$  behaviours. The functions obtained from the fitting for S/Py/TbFe<sub>2</sub> coupled bilayers are  $\theta_{bsat}(\phi) = -0.0026(\cos^2(\phi - 2^\circ) - 0.77)$  and  $\theta_{tsat}(\phi) = -0.00095(\sin^2(\phi + 6^\circ) - 0.21)$ . Finally the magnetoelastic coupling coefficient of the coupled bilayers is calculated:  $b^{\gamma, 2}_{bilayers} = 0.83$  MPa.

Stoner-Wohlfarth model can be used to explain the magnetostriction results of the coupled bilayers. In the coupled bilayers, Py and TbFe<sub>2</sub> magnetic vectors rotate together when driving magnetic field is applied [13]. The rotation of the magnetic vectors will lead to the internal stress change (magnetostrictive stress) in the film, and then magnetostriction occurs (as shown in Figure 7). The “jump” in some magnetostriction loops is caused by the magnetic vectors aligning along the hard axis of the sample, and it reveals the spin dynamics in the process of magnetic vectors rotating from the easy axis to the magnetic field direction. The “jump” will be affected by the driving magnetic field direction and the deviation of easy axis from the long axis of the sample. Further work will be undertaken to explain these features with a model that is more appropriate than Stoner-Wohlfarth model.

## 4. Conclusion

In summary, the magnetostrictions of S/TbFe<sub>2</sub>-single layer and S/Py/TbFe<sub>2</sub>-coupled bilayers were measured by using laser deflectometry. The dependences of the magnetostriction on the driving magnetic field direction have been established. Interesting “jump” reflecting the spin dynamics is observed in the magnetostriction loops of the coupled bilayers. These results show that magnetostriction measurement is a very promising technique to reveal the spin configuration in the thin magnetic films.

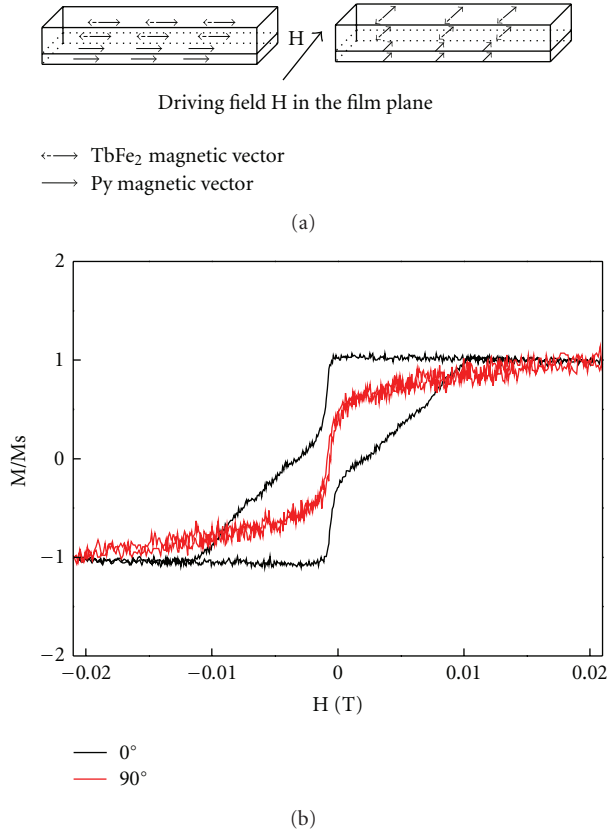


FIGURE 7: (a) Schematic drawing of the Stoner-Wohlfarth model for S/Py/TbFe<sub>2</sub>-coupled bilayers (H: the driving magnetic field); (b) hysteresis loops of S/Py/TbFe<sub>2</sub>-coupled bilayers with field in plane ( $\phi = 0$  and  $90^\circ$ ).

## Acknowledgments

The author gratefully acknowledges Professor Mikhail Indenbom, Mr. JAY Jean-Philippe, and Mr. BEN YOUSSEF Jamal for their guidance, supports, and useful discussions. This project is supported by K. C. Wong Education Foundation in Hong Kong and Opening Funding of National Key Laboratory of Science and Technology on Advanced Composites in Special Environments (no. HIT. KLOF.2009029) in Harbin Institute of Technology.

## References

- [1] A. E. Clark and H. S. Belson, "Giant room-temperature magnetostrictions in TbFe<sub>2</sub> and DyFe<sub>2</sub>," *Physical Review B*, vol. 5, no. 9, pp. 3642–3644, 1972.
- [2] Arthur E. Clark and Henry S. Belson, "Magnetostriction of terbium-iron and erbium-iron alloys," *IEEE Transactions on Magnetics*, vol. MAG-8, no. 3, pp. 477–479, 1972.
- [3] P. J. Grundy, D. G. Lord, and P. I. Williams, "Magnetostriction in TbDyFe thin films," *Journal of Applied Physics*, vol. 76, no. 10, pp. 7003–7005, 1994.
- [4] A. Speliotis, O. Kalogirou, and D. Niarchos, "Magnetostrictive properties of amorphous and partially crystalline TbDyFe thin films," *Journal of Applied Physics*, vol. 81, no. 8, pp. 5696–5698, 1997.
- [5] H. Takagi, S. Tsunashima, S. Uchiyama, and T. Fujii, "Stress induced anisotropy in amorphous Gd-Fe and Tb-Fe sputtered films," *Journal of Applied Physics*, vol. 50, no. 3, pp. 1642–1644, 1979.
- [6] E. Quandt, "Multitarget sputtering of high magnetostrictive Tb-Dy-Fe films," *Journal of Applied Physics*, vol. 75, no. 10, pp. 5653–5655, 1994.
- [7] D. W. Forester, C. Vittoria, J. Schelleng, and P. Lubitz, "Magnetostriction of amorphous Tb<sub>x</sub>Fe<sub>1-x</sub> thin films," *Journal of Applied Physics*, vol. 49, no. 3, pp. 1966–1968, 1978.
- [8] J. Huang, C. Prados, J. E. Evetts, and A. Hernando, "Giant magnetostriction of amorphous Tb<sub>x</sub>Fe<sub>1-x</sub> (0.10 < x < 0.45) thin films and its correlation with perpendicular anisotropy," *Physical Review B*, vol. 51, no. 1, pp. 297–304, 1995.
- [9] E. Quandt and A. Ludwig, "Giant magnetostrictive multilayers (invited)," *Journal of Applied Physics*, vol. 85, no. 8, pp. 6232–6237, 1999.
- [10] E. Quandt, A. Ludwig, J. Betz, K. Mackay, and D. Givord, "Giant magnetostrictive spring magnet type multilayers," *Journal of Applied Physics*, vol. 81, no. 8, pp. 5420–5422, 1997.
- [11] H. D. Chopra, M. R. Sullivan, A. Ludwig, and E. Quandt, "Magnetoelastic and magnetostatic interactions in exchange-spring multilayers," *Physical Review B*, vol. 72, Article ID 054415, 7 pages, 2005.
- [12] E. D. T. D. Lacheisserie, K. Mackay, J. Betz, and J. C. Peuzin, "From bulk to film magnetostrictive actuators," *Journal of Alloys and Compounds*, vol. 275–277, pp. 685–691, 1998.
- [13] J. P. Jay, F. Petit, J. Ben Youssef, M. V. Indenbom, A. Thiaville, and J. Miltat, "Magnetostrictive hysteresis of TbCo/CoFe multilayers and magnetic domains," *Journal of Applied Physics*, vol. 99, no. 9, Article ID 093910, 2006.
- [14] J. B. Youssef, N. Tiercelin, F. Petit, H. Le Gall, V. Preobrazhensky, and P. Pernod, "Statics and dynamics in giant magnetostrictive Tb<sub>x</sub>Fe<sub>1-x</sub>-Fe<sub>0.6</sub>Co<sub>0.4</sub> Multilayers for MEMS," *IEEE Transactions on Magnetics*, vol. 38, no. 5 I, pp. 2817–2819, 2002.
- [15] G. Engdahl, *Handbook of Giant Magnetostrictive Materials*, chapter 6, AP, 2000.
- [16] R. J. Gambino and J. J. Cuomo, "Selective resputtering-induced anisotropy in amorphous films," *Journal of Vacuum Science and Technology*, vol. 15, no. 2, pp. 296–301, 1978.
- [17] Y. Suzuki, J. Haimovich, and T. Egami, "Bond-orientational anisotropy in metallic glasses observed by x-ray diffraction," *Physical Review B*, vol. 35, no. 5, pp. 2162–2168, 1987.
- [18] D. Mergel, H. Heitmann, and P. Hansen, "Pseudocrystalline model of the magnetic anisotropy in amorphous rare-earth transition-metal thin films," *Physical Review B*, vol. 47, no. 2, pp. 882–891, 1993.
- [19] G. Suran, M. Ouahmane, and R. Zuberek, "Correlations between the in-plane uniaxial anisotropy and magnetostriction in amorphous (Co<sub>93</sub>Zr<sub>7</sub>)<sub>100-x</sub>(RE)<sub>x</sub> thin films," *IEEE Transactions on Magnetics*, vol. 30, no. 2 pt 2, pp. 723–725, 1994.
- [20] T. Ambrose, R. L. Sommer, and C. L. Chien, "Angular dependence of exchange coupling in ferromagnet/antiferromagnet bilayers," *Physical Review B*, vol. 56, no. 1, pp. 83–86, 1997.

## Research Article

# Fabrication and Characterization of Composite Containing HCl-Doped Polyaniline and Fe Nanoparticles

Rongcheng Liu,<sup>1</sup> Hong Qiu,<sup>1</sup> Hua Zong,<sup>1</sup> and Chunying Fang<sup>2</sup>

<sup>1</sup>Department of Physics, School of Mathematics and Physics, University of Science and Technology Beijing, 30 Xueyuan Road, Haidian District, Beijing 100083, China

<sup>2</sup>Department of Chemistry, School of Chemistry and Biological Engineering, University of Science and Technology Beijing, 30 Xueyuan Road, Haidian District, Beijing 100083, China

Correspondence should be addressed to Hong Qiu, qiu hong@sas.ustb.edu.cn

Received 24 October 2011; Accepted 12 December 2011

Academic Editor: Makis Angelakeris

Copyright © 2012 Rongcheng Liu et al. This is an open access article distributed under the Creative Commons Attribution License, which permits unrestricted use, distribution, and reproduction in any medium, provided the original work is properly cited.

HCl-doped polyaniline powder (HCl-PANI) was synthesized by using a polymerization procedure. Fe nanoparticles were then deposited on the HCl-PANI at room temperature by direct current magnetron sputtering. After this process the HCl-PANI-Fe composite was obtained. Fe nanoparticle size in the composite is about 100 nm. HCl-PANI structure is not influenced by the Fe nanoparticles. The composite pellet has room temperature ferromagnetism and a conductivity of 0.25 S/cm. Temperature dependence of the conductivity reveals that a carrier transport mechanism in the composite is three-dimensional variable range hopping. Thermogravimetric analysis reveals that a weight loss of the HCl-PANI-Fe composite is smaller than that of the HCl-PANI for the same heating temperature when the temperature exceeds 230°C.

## 1. Introduction

Polyaniline (PANI) having both electrical and magnetic features has attracted considerable attention for its potential applications in electrical, magnetic, and electronic devices as well as stealth technology and electromagnetic interference shielding. The conductive and magnetic PANI composites containing iron oxides such as Fe<sub>3</sub>O<sub>4</sub> and Fe<sub>2</sub>O<sub>3</sub> were mostly studied, for example, see references [1–10]. As it is well known, pure Fe is easily oxidized in moist or oxidizing atmosphere. Thus it is a challenging work to prepare the conductive PANI composites containing Fe (PANI-Fe). Izumi et al. [11] chemically polymerized PANI doped with Fe and found the formation of semiquinone segments upon coordination of emeraldine base PANI to Fe<sup>3+</sup> ions. Li et al. [12] prepared the PANI-Fe polymer at room temperature by chemical synthesis in the absence and presence of an applied magnetic field. The PANI-Fe polymer was a complex rather than a composite in which Fe nanoparticles were covered by PANI. The PANI-Fe complex polymer had both conductive and ferromagnetic behaviors. Fe<sup>3+</sup> ions coordinated mainly with the nitrogen atoms on the quinone

rings. Xue et al. [13] mechanically mixed PANI doped with 4-dodecylbenzenesulfonic acid (DBSA) and Fe nanoparticles obtaining DBSA-PANI-Fe composites. As the Fe nanoparticle content increased from 0 to 70 wt%, a conductivity of the composite pellet decreased linearly from 0.25 to 0.07 S/cm and the saturation magnetization increased monotonically to 78 emu/g. However, the Fe nanoparticles were partly oxidized forming iron oxides which were detected by X-ray diffraction [13]. Thus, in the strict sense, Xue et al. prepared the DBSA-PANI-Fe-Fe<sub>3</sub>O<sub>4</sub> composites.

Sputter deposition is one of the most important techniques for preparing the thin film because the purity of the film can be easily controlled and the adhesion of the film to the substrate can be enhanced. The magnetron sputtering technique can trap electrons in the region near the target and can effectively ionize working gas, leading to fast deposition of the film at room temperature. It was reported that sputter deposition could prepare dense and pure Fe thin films and islands [14, 15]. On the basis of the above-mentioned advantage of sputter deposition, it is desirable to prepare PANI-Fe composites by sputter-depositing Fe islands or particles on the PANI. Recently, HCl-PANI-Ni composites

have been successfully prepared using the well-established polymerization procedure followed by sputter-deposition of Ni, that is, using the chemically and physically combinative method [16]. The HCl-PANI-Ni composites had the conductive and ferromagnetic features. In the present work, HCl-doped polyaniline powder (HCl-PANI) is synthesized by using a polymerization procedure. Fe nanoparticles are deposited on the HCl-PANI at room temperature by direct current (DC) magnetron sputtering. After this process, the HCl-PANI-Fe composite is obtained. Structural, magnetic, and electrical properties of the composite are studied. This work, besides fabrication and study of the HCl-PANI-Fe composite, will further confirm the feasibility of the chemically and physically combinative method to prepare the PANI composites containing metal nanoparticles.

## 2. Experimental Procedure

**2.1. Preparation of HCl-PANI-Fe Composite.** All the reagents were purchased from Beijing Chemical Works and were analytical grade. Only aniline was doubly distilled under reduced pressure and stored in refrigerator (at about 4°C) prior to using. The other reagents were used without further purification. HCl-PANI was chemically synthesized using the well-established polymerization procedure [17]. Aniline (0.1 mol) was dissolved in 100 mL aqueous hydrochloric acid (HCl, 1 mol/L) taken in a three-neck flask. The mixture solution was cooled and stirred at -3°C by a magnetic stirrer. Then 51.5 mL ammonium persulfate solution (2.4 mol/L) in a constant pressure funnel was slowly added into the mixture solution for 1 hour in order to avoid heating the reaction mixture. The reaction proceeded at -3°C for 8 hours. The final solution was filtered. The precipitate was washed with aqueous HCl (1 mol/L) for protonating. The protonated precipitate was washed with deionized water and acetone until the washing water and acetone became colorless. Then the powder was dried at 50°C in vacuum for two days. The HCl-PANI powder was obtained.

The HCl-PANI powder was compacted to pellets with 0.2 mm in thickness and 50 mm in diameter. Fe particles or thin films were deposited on the two surfaces of the HCl-PANI pellet at room temperature by using a DC magnetron sputtering system (KYKY Technology Development). The Fe target (99.99% in purity) with 50 mm in diameter was inclined at an angle of 45° to the pellet. The distance between the target and the pellet was about 100 mm. The pellet holder was rotated using a stepping motor during deposition in order to obtain the uniform distribution of Fe particles or the uniform thickness of Fe thin film. Prior to deposition, the working chamber was evacuated to a pressure lower than  $2 \times 10^{-4}$  Pa using a turbo molecular pump. An Ar gas (99.9995% in purity) pressure was 1.0 Pa and a sputtering power applied to the target was fixed at 100 W. The deposition rate was about 12 nm/min and the deposition time was 10 minutes.

In order to obtain the HCl-PANI-Fe composite, the HCl-PANI pellet sputter-deposited Fe particles or thin film was mechanically milled at an almost same speed in an agate mortar for 30 minutes in ambient air. According to the Fe deposition amount and the pellet mass, the nominal Fe

content in the HCl-PANI-Fe composite was estimated to be about 1.66 wt%. The composite powder was compacted to pellets with 0.5 mm in thickness and 13 mm in diameter at a same pressure.

**2.2. Analysis of HCl-PANI-Fe Composite.** X-ray diffraction (XRD) (Rigaku, D/Max-RB) was used to analyze the structure of the HCl-PANI-Fe composite. The XRD measurements were performed in a standard  $\theta$ - $2\theta$  scan using a Cu K $\alpha$  radiation filtered by a crystal monochromator (wavelength  $\lambda = 0.15406$  nm). Transmission electron microscopy (TEM) (Philips, F20) was used to observe the structure of the Fe particles in the composite. The molecular structure of the composite was characterized by Fourier transform infrared spectroscope (FT-IR) (Nexus, 670). A magnetization curve of the composite pellet was measured at room temperature using a vibrating sample magnetometer (VSM) (Quantum Design, Versalab). The magnetic field was applied along the pellet plane during the VSM measurement. A temperature dependence of the magnetization for the HCl-PANI-Fe composite pellet was measured from 55 K to 300 K. First, the composite pellet was cooled down to 55 K at zero field. Then the magnetization data were taken with warming up under a magnetic field of 1000 Oe applied along the pellet plane. The warming rate was approximate to 4 K/min. The magnetization data of the HCl-PANI-Fe composite was estimated by subtracting the signal of the sample holder. Resistance  $R$  of the HCl-PANI-Fe composite pellet was measured at room temperature using a four-point probe technique. The spacing between the two adjacent probe tips was 3 mm. The conductivity  $\sigma$  of the composite pellet can be given by [18]

$$\sigma = \frac{1}{3.31 \times R \times d}, \quad (1)$$

where  $3.31 \times R$  is the sheet resistance and  $d$  is the pellet thickness, which was measured by a micrometer. A temperature dependence of the conductivity for the HCl-PANI-Fe composite pellet was measured in the temperature range of 55–290 K using the Cryogen-Magnet system with the four-point probe (Cryogenic, CFM-5T-H3-CFVTI-1.6 K-24.5). Thermogravimetric analysis (TGA) (Setaram, Labsy-Evo) was used to study a weight loss of the composite in air at heating temperature up to 400°C. The heating rate was 10°C/min.

## 3. Results and Discussion

Figure 1 shows XRD patterns of the HCl-PANI pellet and the HCl-PANI-Fe composite pellet. As can be seen from Figure 1, the HCl-PANI pellet and the HCl-PANI-Fe composite pellet have a crystalline structure of emeraldine salt (ES-I) [19]. For the composite, the Fe nanoparticles could not influence the crystalline structure of the HCl-PANI. Furthermore, a weak Fe(110) diffraction peak can be detected at a diffraction angle of about 44.76°. According to the diffraction angle of Fe(110) peak, the lattice constant of the Fe nanoparticles is calculated to be  $0.2861 \pm 0.0006$  nm, which is almost equal to that of

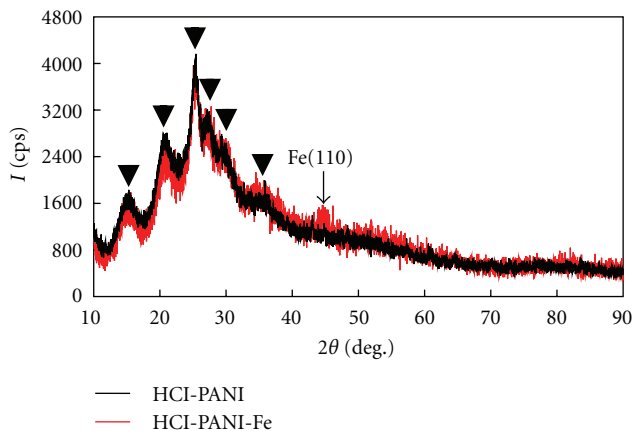
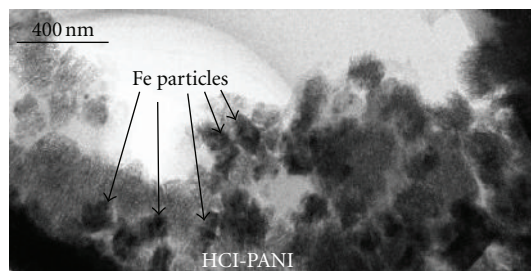


FIGURE 1: XRD patterns of the HCl-PANI pellet and the HCl-PANI-Fe composite pellet. ▼ represents the diffraction peaks of HCl-PANI.

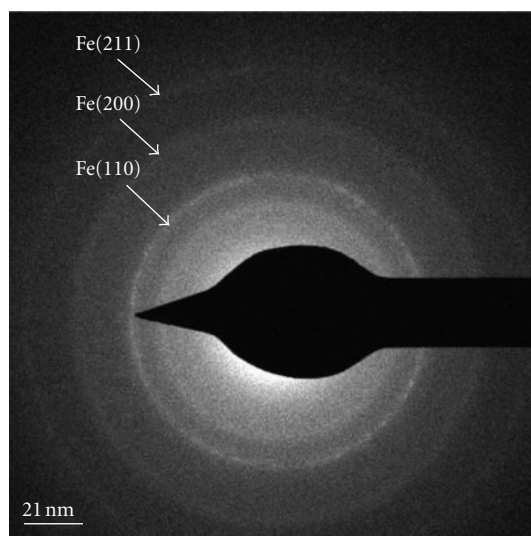
the Fe bulk (0.28664 nm). No diffraction peaks from the iron oxides are detected.

Figure 2 shows a TEM microphotograph and an electron diffraction (ED) pattern of the HCl-PANI-Fe composite. As can be seen from Figure 2, Fe nanoparticles exist in the composite and some Fe nanoparticles aggregate. The Fe particle size is about 100 nm. These Fe nanoparticles were grown on the HCl-PANI by sputter-depositing. As shown in the ED pattern of Figure 2, Fe(110), Fe(200), and Fe(211) diffraction rings are observed. According to these diffraction rings, the lattice constant of the Fe nanoparticles is calculated to be  $0.287 \pm 0.003$  nm, which is almost equal to that of the Fe bulk (0.28664 nm). The result is consistent with the XRD result. It should be noted that a halo ring shows on the inner side of the Fe(110) diffraction ring. According to the radius of the halo ring, the plane spacing of the atomic short-range order region is estimated to be  $0.251 \pm 0.002$  nm, which is approximate to the plane spacing of Fe<sub>3</sub>O<sub>4</sub>(311) (0.25312 nm). Therefore, it is considered that the halo ring is attributed to amorphous Fe<sub>3</sub>O<sub>4</sub> formed on the Fe nanoparticle surface [20]. Figure 3 shows a high-resolution TEM (HRTEM) image of the HCl-PANI-Fe composite. Using the HRTEM image, the (110) plane spacing of Fe nanoparticle is calculated to be  $0.202 \pm 0.003$  nm. The (110) plane spacing of the Fe nanoparticle is almost equal to that of the Fe bulk (0.20268 nm). This result is consistent with both the XRD and ED results. The HRTEM image definitely shows the Fe nanoparticle formed in the composite.

Figure 4 shows FT-IR spectra of the HCl-PANI and the HCl-PANI-Fe composite. The FT-IR spectroscopy is a powerful tool for analyzing the molecular structure and the oxidation state of PANI [21, 22]. As can be seen from Figure 4, for both the samples, the absorption peak positions of FT-IR spectra are the same. The peak at  $1587 \text{ cm}^{-1}$  is related to the quinone structure and that at  $1471 \text{ cm}^{-1}$  is characterized by benzene ring stretching. Therefore, it demonstrates that the aromatic structure of PANI is retained in the HCl-PANI-Fe composite. An intensity ratio of the peak at  $1587 \text{ cm}^{-1}$  to that at  $1471 \text{ cm}^{-1}$  is a quantitative measurement of the oxidation



(a)



(b)

FIGURE 2: TEM microphotograph and ED pattern of the HCl-PANI-Fe composite.

state of PANI [21]. The intensity ratios of the HCl-PANI and HCl-PANI-Fe composite are almost the same, meaning that it does not appear any indication for severe change in the oxidation state for the HCl-PANI-Fe composite. It has been reported that for the PANI-Fe the Fe<sup>3+</sup> ions coordinate mainly with the nitrogen atoms on the quinone rings leading to the peak of the quinone units shifting to a higher wave numbers compared with the PANI [12]. In this work, however, the peak position at  $1587 \text{ cm}^{-1}$  related to the quinone units is not influenced by the Fe nanoparticles. It indicates that an interaction between the Fe nanoparticle and the PANI is predominated by a physical mechanism because the Fe nanoparticles are sputter-deposited on the HCl-PANI or adhere physically to the HCl-PANI. Namely, the Fe nanoparticles are physically adsorbed on the HCl-PANI or adhere physically to the HCl-PANI. The peak at  $1295 \text{ cm}^{-1}$  is also attributed to C–N stretching in the quinoid benzoid rings. The peaks at  $1243$  and  $1115 \text{ cm}^{-1}$  result from vibrations in the polar structure of the conducting protonated form [23]. The very weak peak at near  $470 \text{ cm}^{-1}$  for the HCl-PANI-Fe composite is attributed to the Fe–O interaction [24–26]. However, the characteristic peak at  $530$ – $595 \text{ cm}^{-1}$  due to the Fe–O stretching band of iron oxide [24–27] cannot be detected. Therefore, it is considered that the Fe nanoparticles are mainly formed in the composite. It is

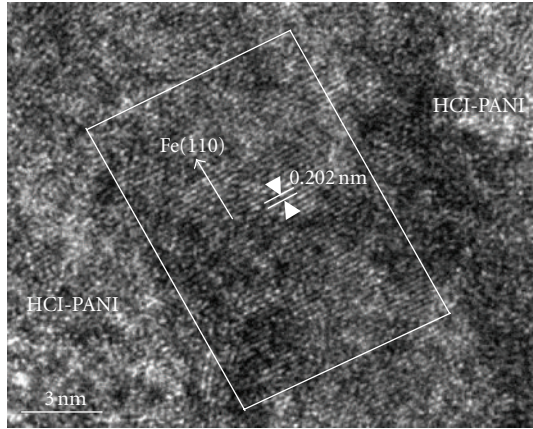
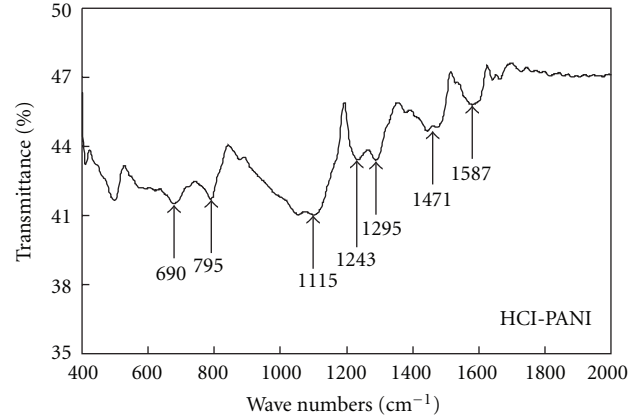


FIGURE 3: HRTEM image of the HCl-PANI-Fe composite. The (110) plane spacing of Fe nanoparticle is calculated by using the lattice pattern in the rectangular area represented in the figure.

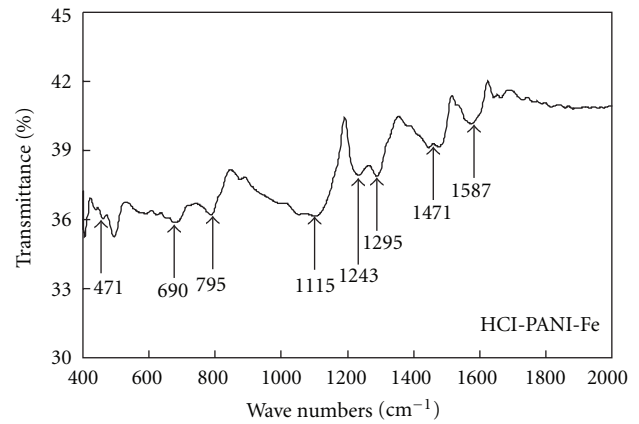
consistent with the results of XRD, ED, and HRTEM. The very weak peak at near  $470\text{ cm}^{-1}$  for the composite might be due to the Fe–O interaction on the Fe nanoparticle surface.

Figure 5 shows a magnetization curve and a temperature dependence of the magnetization for the HCl-PANI-Fe composite pellet. As can be seen from Figure 5, the HCl-PANI-Fe composite pellet exhibits hysteresis, meaning that the composite has room temperature ferromagnetism. As a comparison, a magnetization curve of the HCl-PANI was also measured by VSM. The HCl-PANI does not show the magnetic hysteresis loop [16]. The temperature dependence of the magnetization further proves that the HCl-PANI-Fe composite has the ferromagnetism even over room temperature. A study on organic magnets such as PANI is significant for fundamental and practical viewpoints [28, 29]. It was found that the HCl-PANI exhibited a paramagnetic behavior at 10 K and its paramagnetic behavior gradually changed into diamagnetic with increasing the temperature up to 330 K [30]. It was reported that a new type of polymer produced from polyaniline and tetracyanoquinodimethane was ferrimagnetic or ferromagnetic with a Curie temperature of over 350 K and the magnetically ordered state developed with aging time [31]. The research and development of the organic magnets with a high Curie temperature, which has a magnetic order with strong magnetic interactions, is a challenging work [32]. In the present work, the HCl-PANI-Fe composite, which only contains about 1.66 wt% Fe, has better room temperature ferromagnetism. The saturation field and the coercivity are estimated to be about 4000 Oe and 300 Oe, respectively. The residual magnetization ratio, that is, the ratio of the residual magnetization to the saturation magnetization, is 0.18.

Conductivities of the HCl-PANI pellet and the HCl-PANI-Fe composite pellet are 0.42 S/cm and 0.25 S/cm, respectively. Figure 6 shows a variation of conductivity with temperature for the HCl-PANI-Fe composite pellet, plotted as  $\ln\sigma$  versus  $T^{-1/4}$ . In the variable range hopping (VRH)



(a)



(b)

FIGURE 4: FT-IR spectra of the HCl-PANI and the HCl-PANI-Fe composite.

model [33–35], a temperature  $T$  dependence of conductivity  $\sigma$  follows the relation

$$\sigma = \sigma_0 \exp \left[ - \left( \frac{T_0}{T} \right)^{1/r} \right], \quad (2)$$

where  $T_0$  is the Mott characteristic temperature and  $\sigma_0$  is the conductivity at  $T = \infty$ .  $T_0$  and  $\sigma_0$  are determined by the localization length, the density of state, and the hopping distance in the material. The  $r$  is determined by a dimension of the researching system. For the one-dimensional (1D), two-dimensional (2D), and three-dimensional (3D) systems,  $r$  is equal to 2, 3, and 4, respectively. In the 3D-VRH model, (2) can be express as

$$\sigma = \sigma_0 \exp \left[ - \left( \frac{T_0}{T} \right)^{1/4} \right]. \quad (3)$$

As can be seen from Figure 6, the plots exhibit a good linear dependence having a correlation coefficient better than 0.9991. It indicates that the 3D-VRH model is suitable for explaining the carrier transport mechanism of the HCl-PANI-Fe composite. It has been reported that for the HCl-PANI the carrier transport mechanism is 3D-VRH [16, 36].

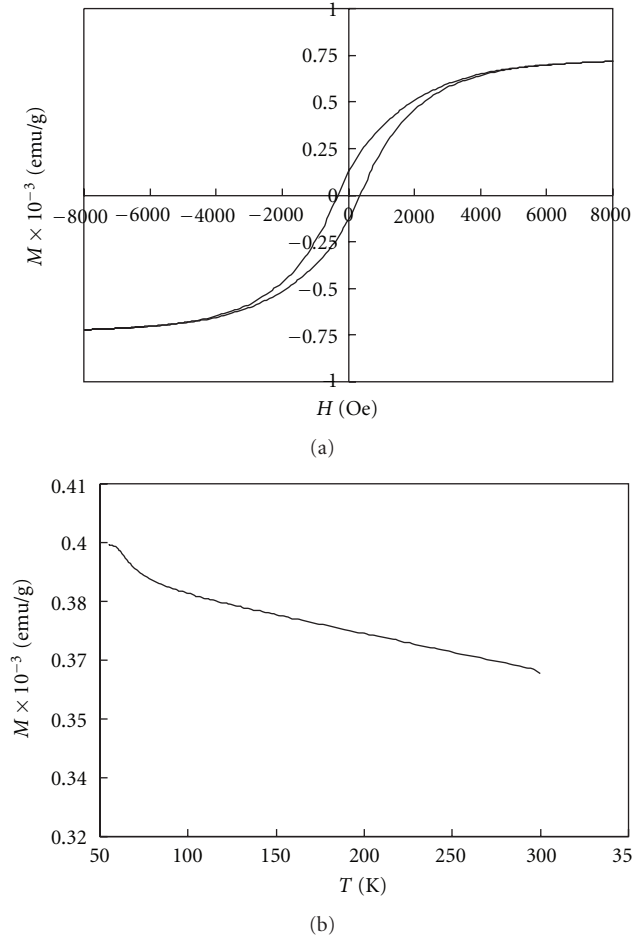


FIGURE 5: Magnetization curve and temperature dependence of the magnetization for the HCl-PANI-Fe composite pellet.

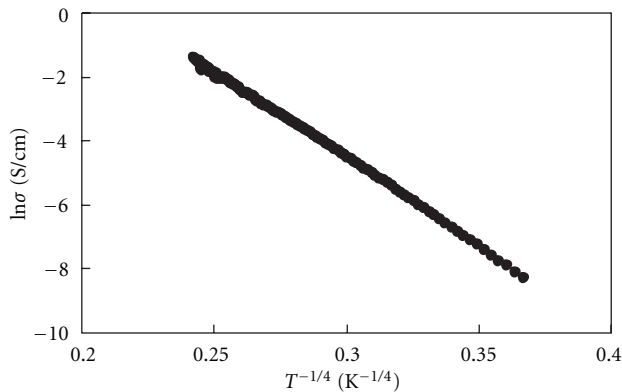


FIGURE 6: Variation of conductivity with temperature for the HCl-PANI-Fe composite pellet, plotted as  $\ln\sigma$  versus  $T^{-1/4}$ .

Therefore, the Fe nanoparticles do not change the carrier transport mechanism of the HCl-PANI in the HCl-PANI-Fe composite. Values of the  $T_0$  and  $\sigma_0$  obtained from the fitted straight line of Figure 6 are equal to 8417719 K and 112420 S/cm.  $\text{Cl}^-$  ions have small size in the HCl-PANI. Then the interchain separation may be small, resulting in

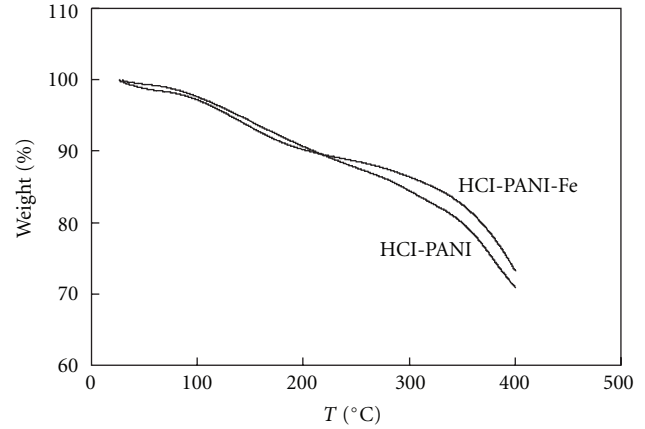


FIGURE 7: Thermogravimetric curves for the HCl-PANI and the HCl-PANI-Fe composite.

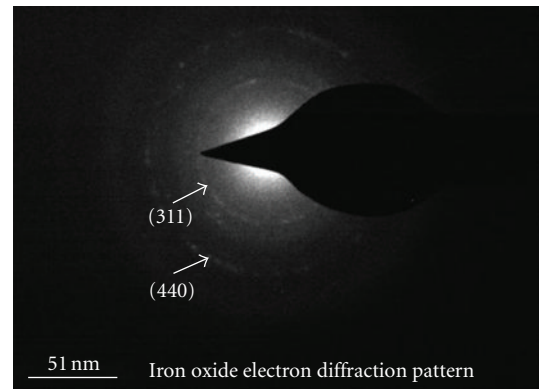


FIGURE 8: ED pattern of the heat-treated HCl-PANI-Fe composite.

an existence of strong coherence/coupling between chains [34]. Therefore, charge carriers could hop from one chain to the other in terms of the 3D-VRH. The Fe nanoparticles are nanosized and the nanoparticle amount is less. Thus, the Fe nanoparticles do not weaken strong coherence/couple between the PANI chains. As a result, for the HCl-PANI-Fe composite, the carrier transport mechanism is also 3D-VRH.

The TGA measurements for the HCl-PANI and the HCl-PANI-Fe composite were carried out in air to study their thermal stability in atmosphere. Figure 7 shows thermogravimetric curves for the HCl-PANI and the HCl-PANI-Fe composite. As can be seen from Figure 7, a three-step weight loss process can be observed for both the samples. The first step at temperatures up to 110 °C may be due to the loss of water, the second step in the temperature range of 110–300 °C can be attributed to the loss of impurities such as HCl dopant and the third step at the temperatures over 300 °C may be due to the degradation of the polymer [37]. Furthermore, it should be noted that for the same heating temperature the weight loss of the HCl-PANI-Fe composite is smaller than that of the HCl-PANI after heating over 230 °C. This result is similar to that of the HCl-PANI-Fe composites mixed mechanically [38] but differs from that of the HCl-PANI-Ni composite [16]. The Fe nanoparticles in the composite

might be oxidized during the TGA measurement. In order to confirm the oxidation of the Fe nanoparticles in the HCl-PANI-Fe composite, the composite was heat treated in air at 295°C for 30 minutes. Figure 8 shows an ED pattern of the heat-treated HCl-PANI-Fe composite. As shown in Figure 8, the diffraction rings from the iron oxide are only observed, meaning that the Fe nanoparticles in the composite were oxidized by heat treating. It is consistent with the result reported previously for the HCl-PANI-Fe composites mixed mechanically [38]. Therefore, it is considered that the Fe nanoparticles in the composite are oxidized during TGA measuring. It was reported that heating led to an increase in the weight of the Fe nanoparticles due to the Fe oxidation when the heating temperature exceeded 100°C [20]. Furthermore, it has also been proposed that the PANI-Fe<sub>3</sub>O<sub>4</sub> and PANI-Fe<sub>2</sub>O<sub>3</sub> composites have a better thermal stability compared with the PANI [6, 9, 39]. However, in the present work, the reason that the weight loss of the HCl-PANI-Fe composite is smaller than that of the HCl-PANI over 230°C is not clear. Detailed work should be further done.

#### 4. Summary

The HCl-PANI-Fe composite was successfully prepared by using the well-established polymerization procedure followed by the sputter-deposition of Fe. The Fe nanoparticle size is about 100 nm. HCl-PANI structure is not influenced by the Fe nanoparticles. The composite pellet has room temperature ferromagnetism and a conductivity of 0.25 S/cm. The carrier transport mechanism in the composite is three-dimensional variable range hopping. The weight loss of the HCl-PANI-Fe composite is smaller than that of the HCl-PANI for the same heating temperature when the temperature exceeds 230°C. Furthermore, this work also confirms the feasibility of the chemically and physically combinative method to prepare the PANI composites containing metal nanoparticles.

#### Acknowledgments

The authors would like to thank Dr. Xin Gao at the Analysis Center of School of Materials Science and Engineering for supporting TEM and HRTEM observations. The authors would also like to thank Dr. Jinxia Deng at Department of Chemistry for the TGA measurements.

#### References

- [1] M. X. Wan and J. C. Li, "Electrical and ferromagnetic behavior of polyaniline composites," *Synthetic Metals*, vol. 101, no. 1, pp. 844–845, 1999.
- [2] J. Deng, X. Ding, W. Zhang et al., "Magnetic and conducting Fe<sub>3</sub>O<sub>4</sub>-cross-linked polyaniline nanoparticles with core-shell structure," *Polymer*, vol. 43, no. 8, pp. 2179–2184, 2002.
- [3] Z. Zhang and M. Wan, "Nanostructures of polyaniline composites containing nano-magnet," *Synthetic Metals*, vol. 132, no. 2, pp. 205–212, 2003.
- [4] J. C. Aphesteguy and S. E. Jacobo, "Composite of polyaniline containing iron oxides," *Physica B*, vol. 354, no. 1-4, pp. 224–227, 2004.
- [5] Q. Xiao, X. Tan, L. Ji, and J. Xue, "Preparation and characterization of polyaniline/nano-Fe<sub>3</sub>O<sub>4</sub> composites via a novel Pickering emulsion route," *Synthetic Metals*, vol. 157, no. 18–20, pp. 784–791, 2007.
- [6] Y. J. Zhang, Y. W. Lin, C. C. Chang, and T. M. Wu, "Magnetic properties of hydrophilic iron oxide/polyaniline nanocomposites synthesized by in situ chemical oxidative polymerization," *Synthetic Metals*, vol. 160, no. 9-10, pp. 1086–1091, 2010.
- [7] A. C. V. de Araújo, R. J. de Oliveira, S. Alves Júnior et al., "Synthesis, characterization and magnetic properties of polyaniline-magnetite nanocomposites," *Synthetic Metals*, vol. 160, no. 7-8, pp. 685–690, 2010.
- [8] M. Petrychuk, V. Kovalenko, A. Pud, N. Ogurtsov, and A. Gubin, "Ternary magnetic nanocomposites based on core-shell Fe<sub>3</sub>O<sub>4</sub>/polyaniline nanoparticles distributed in PVDF matrix," *Physica Status Solidi A*, vol. 207, no. 2, pp. 442–447, 2010.
- [9] K. Singh, A. Ohlan, R. K. Kotnala, A. K. Bakhshi, and S. K. Dhawan, "Dielectric and magnetic properties of conducting ferromagnetic composite of polyaniline with  $\gamma$ -Fe<sub>2</sub>O<sub>3</sub> nanoparticles," *Materials Chemistry and Physics*, vol. 112, no. 2, pp. 651–658, 2008.
- [10] Z. Wang, H. Bi, J. Liu, T. Sun, and X. Wu, "Magnetic and microwave absorbing properties of polyaniline/ $\gamma$ -Fe<sub>2</sub>O<sub>3</sub> nanocomposite," *Journal of Magnetism and Magnetic Materials*, vol. 320, no. 16, pp. 2132–2139, 2008.
- [11] C. M. S. Izumi, V. R. L. Constantino, A. M. C. Ferreira, and M. L. A. Temperini, "Spectroscopic characterization of polyaniline doped with transition metal salts," *Synthetic Metals*, vol. 156, no. 9-10, pp. 654–663, 2006.
- [12] S. Li, C. Zhu, L. Tang, and J. Kan, "Unique properties of polyaniline in the presence of applied magnetic field and ferric chloride," *Materials Chemistry and Physics*, vol. 124, no. 1, pp. 168–172, 2010.
- [13] W. Xue, H. Qiu, K. Fang, J. Li, J. Zhao, and M. Li, "Electrical and magnetic properties of the composite pellets containing DBSA-doped polyaniline and Fe nanoparticles," *Synthetic Metals*, vol. 156, no. 11–13, pp. 833–837, 2006.
- [14] S. Kreuzer, K. Prügl, G. Bayreuther, and D. Weiss, "Epitaxial growth and patterning of sputtered Fe films on GaAs(001)," *Thin Solid Films*, vol. 318, no. 1-2, pp. 219–222, 1998.
- [15] C. Quintana, J. L. Menéndez, Y. Huttel, M. Lancin, E. Navarro, and A. Cebollada, "Structural characterization of Fe(1 1 0) islands grown on  $\alpha$ -Al<sub>2</sub>O<sub>3</sub>(0 0 0 1)," *Thin Solid Films*, vol. 434, no. 1-2, pp. 228–238, 2003.
- [16] R. Liu, H. Qiu, H. Li, H. Zong, and C. Fang, "Fabrication and characteristics of composite containing HCl-doped polyaniline and Ni nanoparticles," *Synthetic Metals*, vol. 160, no. 23-24, pp. 2404–2408, 2010.
- [17] P. N. Adams, P. J. Laughlin, A. P. Monkman, and A. M. Kenwright, "Low temperature synthesis of high molecular weight polyaniline," *Polymer*, vol. 37, no. 15, pp. 3411–3417, 1996.
- [18] "Standard test method for sheet resistance of thin metallic films with a collinear four-probe array," ASTM International, West Conshohocken, F390-98, 2003.
- [19] M. E. Jozefowicz, R. Laversanne, H. H. S. Javadi et al., "Multiple lattice phases and polaron-lattice spinless-defect competition in polyaniline," *Physical Review B*, vol. 39, no. 17, pp. 12958–12961, 1989.

- [20] C. J. Choi, O. Tolochko, and B. K. Kim, "Preparation of iron nanoparticles by chemical vapor condensation," *Materials Letters*, vol. 56, no. 3, pp. 289–294, 2002.
- [21] G. E. Asturias, A. G. MacDiarmid, R. P. McCall, and A. J. Epstein, "The oxidation state of "emeraldine" base," *Synthetic Metals*, vol. 29, no. 1, pp. 157–162, 1989.
- [22] J. Tang, X. Jing, B. Wang, and F. Wang, "Infrared spectra of soluble polyaniline," *Synthetic Metals*, vol. 24, no. 3, pp. 231–238, 1988.
- [23] J. Prokeš, M. Trchová, D. Hlavatá, and J. Stejskal, "Conductivity ageing in temperature-cycled polyaniline," *Polymer Degradation and Stability*, vol. 78, no. 2, pp. 393–401, 2002.
- [24] A. Šarić, S. Musić, K. Nomura, and S. Popović, "FT-IR and  $^{57}\text{Fe}$  Mossbauer spectroscopic investigation of oxide precipitated from  $\text{Fe}(\text{NO}_3)_3$  solutions," *Journal of Molecular Structure*, vol. 480–481, pp. 633–636, 1999.
- [25] M. Ristić, E. De Grave, S. Musić, S. Popović, and Z. Orehovec, "Transformation of low crystalline ferrihydrite to  $\alpha\text{-Fe}_2\text{O}_3$  in the solid state," *Journal of Molecular Structure*, vol. 834–836, pp. 454–460, 2007.
- [26] M. Žic, M. Ristić, and S. Musić, "Precipitation of  $\alpha\text{-Fe}_2\text{O}_3$  from dense  $\beta\text{-FeOOH}$  suspensions with added ammonium amidosulfonate," *Journal of Molecular Structure*, vol. 924–926, pp. 235–242, 2009.
- [27] K. R. Reddy, K. P. Lee, and A. I. Gopalan, "Self-assembly approach for the synthesis of electro-magnetic functionalized  $\text{Fe}_3\text{O}_4$ /polyaniline nanocomposites: effect of dopant on the properties," *Colloids and Surfaces A*, vol. 320, no. 1–3, pp. 49–56, 2008.
- [28] A. J. Epstein and J. S. Miller, "Molecule- and polymer-based magnets, a new frontier," *Synthetic Metals*, vol. 80, no. 2, pp. 231–237, 1996.
- [29] J. A. Crayston, J. N. Devine, and J. C. Walton, "Conceptual and synthetic strategies for the preparation of organic magnets," *Tetrahedron*, vol. 56, no. 40, pp. 7829–7857, 2000.
- [30] P. Dallas, D. Stamopoulos, N. Boukos, V. Tzitzios, D. Niarchos, and D. Petridis, "Characterization, magnetic and transport properties of polyaniline synthesized through interfacial polymerization," *Polymer*, vol. 48, no. 11, pp. 3162–3169, 2007.
- [31] N. A. Zaidi, S. R. Giblin, I. Terry, and A. P. Monkman, "Room temperature magnetic order in an organic magnet derived from polyaniline," *Polymer*, vol. 45, no. 16, pp. 5683–5689, 2004.
- [32] D. Luneau, "Molecular magnets," *Current Opinion in Solid State and Materials Science*, vol. 5, no. 2–3, pp. 123–129, 2001.
- [33] M. Gosh, A. Barman, A. K. Meikap, S. K. De, and S. Chatterjee, "Hopping transport in HCl doped conducting polyaniline," *Physics Letters A*, vol. 260, no. 1–2, pp. 138–148, 1999.
- [34] Z. H. Wang, H. H. S. Javadi, A. Ray, A. G. MacDiarmid, and A. J. Epstein, "Electron localization in polyaniline derivatives," *Physical Review B*, vol. 42, no. 8, pp. 5411–5414, 1990.
- [35] W. Li and M. Wan, "Porous polyaniline films with high conductivity," *Synthetic Metals*, vol. 92, no. 2, pp. 121–126, 1998.
- [36] J. Li, K. Fang, H. Qiu, S. Li, and W. Mao, "Micromorphology and electrical property of the HCl-doped and DBSA-doped polyanilines," *Synthetic Metals*, vol. 142, no. 1–3, pp. 107–111, 2004.
- [37] G. M. Do Nascimento, C. H. B. Silva, and M. L. A. Temperini, "Spectroscopic characterization of the structural changes of polyaniline nanofibers after heating," *Polymer Degradation and Stability*, vol. 93, no. 1, pp. 291–297, 2008.
- [38] G. Ren, H. Qiu, Q. Wu, H. Li, H. Fan, and C. Fang, "Thermal stability of composites containing HCl-doped polyaniline and Fe nanoparticles," *Materials Chemistry and Physics*, vol. 120, no. 1, pp. 127–133, 2010.
- [39] S. S. Umare, B. H. Shambharkar, and R. S. Ningthoujam, "Synthesis and characterization of polyaniline- $\text{Fe}_3\text{O}_4$  nanocomposite: electrical conductivity, magnetic, electrochemical studies," *Synthetic Metals*, vol. 160, no. 17–18, pp. 1815–1821, 2010.